Astronomy & Astrophysics manuscript no. output
August 22, 2018

SEDIGISM: The kinematics of ATLASGAL filaments

M. Mattern[1], J. Kauffmann[1,2], T. Csengeri[1], J. S. Urquhart[3], S. Leurini[4], F. Wyrowski[1], A. Giannetti[5], P. J. Barnes[6,7], H. Beuther[8], L. Bronfman[9], A. Duarte-Cabral[10], T. Henning[8], J. Kainulainen[8,11], K. M. Menten[1], E. Schisano[12], and F. Schuller[13]

[1] Max-Planck-Institut für Radioastronomie, Auf dem Hügel 69, D-53121 Bonn e-mail: mmattern@mpifr-bonn.mpg.de
[2] Haystack Observatory, Massachusetts Institute of Technology, 99 Millstone Road, Westford, MA 01886, USA
[3] School of Physical Sciences, University of Kent, Ingram Building, Canterbury, Kent CT2 7NH, UK
[4] INAF - Osservatorio Astronomico di Cagliari, via della Scienza 5, 09047 Selargius (CA), Italy
[5] INAF - Istituto di Radioastronomia, and Italian ALMA Regional Centre, via P. Gobetti 101, 40129 Bologna, Italy
[6] Astronomy Department, University of Florida, PO Box 112055, Gainesville, FL 32611, USA
[7] School of Science and Technology, University of New England, NSW 2351 Armidale, Australia
[8] Max-Planck-Institut für Astronomie, Königstuhl 17, 69117 Heidelberg, Germany
[9] Departamento de Astronomía, Universidad de Chile, Casilla 36-D, Santiago, Chile
[10] School of Physics and Astronomy, Cardiff University, Queens Buildings, The Parade, Cardiff CF24 3AA, UK
[11] Dept. of Space, Earth and Environment, Chalmers University of Technology, Onsala Space Observatory, 439 92 Onsala, Sweden
[12] Istituto di Astrofisica e Planetologia Spaziali, INAF, via Fosso del Cavaliere 100, I-00133 Roma, Italy
[13] AIM, CEA, CNRS, Université Paris-Saclay, Université Paris Diderot, Sorbonne Paris Cité, F-91191 Gif-sur-Yvette, France

Received ...; accepted ...

ABSTRACT

Analysing the kinematics of filamentary molecular clouds is a crucial step towards understanding their role in the star formation process. Therefore, we study the kinematics of 283 filament candidates in the inner Galaxy, that were previously identified in the ATLASGAL dust continuum data. The ^{13}CO(2 – 1) and C^{18}O(2 – 1) data of the SEDIGISM survey (Structure, Excitation, and Dynamics of the Inner Galactic Inter Stellar Medium) allows us to analyse the kinematics of these targets and to determine their physical properties at a resolution of 30″ and 0.25 km s^{-1}. To do so, we developed an automated algorithm to identify all velocity components along the line-of-sight correlated with the ATLASGAL dust emission, and derive size, mass, and kinematic properties for all velocity components. We find two-third of the filament candidates are coherent structures in position-position-velocity space. The remaining candidates appear to be the result of a superposition of two or three filamentary structures along the line-of-sight. At the resolution of the data, on average the filaments are in agreement with Plummer-like radial density profiles with a power-law exponent of $p \approx 1.5 \pm 0.5$, indicating that they are typically embedded in a molecular cloud and do not have a well-defined outer radius. Also, we find a correlation between the observed mass per unit length and the velocity dispersion of the filament of $m \propto \sigma_v^2$. We show that this relation can be explained by a virial balance between self-gravity and pressure. Another possible explanation could be radial collapse of the filament, where we can exclude infall motions close to the free-fall velocity.

Key words. molecular data – methods: data analysis Stars: formation – ISM: clouds – ISM: kinematics and dynamics – submillimeter: ISM

1. Introduction

Filamentary structures play an important role in the process of star formation. Observations at different wavelengths based on various tracers have revealed that filaments are ubiquitous in the interstellar medium (e.g., Schneider & Elmegreen 1979; Molinari et al. 2010; André et al. 2010; Schisano et al. 2014; Ragan et al. 2014; Li et al. 2016). Filaments are seen in quiescent and star-forming clouds, in which a significant fraction of pre-stellar cores are located (André et al. 2010). Filamentary structures have wide ranges of masses ($\sim 1 - 10^5\,M_\odot$) and lengths ($\sim 0.1 - 100$ pc) (e.g., Bally et al. 1987; Jackson et al. 2010; Arzoumanian et al. 2011; Hernandez et al. 2012; Hacar et al. 2013; Kirk et al. 2013; Palmeirim et al. 2013; Li et al. 2016; Kainulainen et al. 2013; Beuther et al. 2015; Kainulainen et al. 2017; Abreu-Vicente et al. 2016; Zucker et al. 2017).

The processes of filament formation and filament fragmentation to star-forming cores are not well understood. Because of the wide range of filament size scales and masses these processes might also differ among filaments. High-resolution magnetohydrodynamical simulations of molecular cloud evolution and filament formation show subsonic motions in the inner dense regions of filaments, but the surrounding low density gas is supersonic (Padoan et al. 2001; Federrath 2016). Additionally, accretion flows along and radially onto the filament have been seen in observations and simulations (Schneider et al. 2010; Peretto et al. 2013, 2014; Henshaw et al. 2014; Smith et al. 2015). Therefore, the formation and evolution of filaments is a highly

dynamical process and to constrain it is essential to study their kinematics.

Studies of filaments have targeted mainly sources in nearby star-forming regions, e.g. Orion, Musca and Taurus (Bally et al. 1987; Takahashi et al. 2013; Hacar et al. 2016; Kainulainen et al. 2015, 2017), where high resolution data ($\sim$ 0.01 pc, 0.1 km s^{-1}) reveals sub-structures like fibers (Hacar et al. 2013; Hacar et al. 2018), or prominent mid-infrared extinction structures, e.g. "Nessie" and infrared dark clouds like G11.11−0.12 (Johnstone et al. 2003; Pillai et al. 2006b; Schneider et al. 2010; Jackson et al. 2010; Kainulainen et al. 2013; Henshaw et al. 2014; Mattern et al. 2018). Detailed studies of these filaments led us to recognize their important role in star formation, and their internal structure, but studies of small samples do not allow to draw general conclusions. In particular the filaments towards the more distant, typically high-mass star forming regions have not yet been systematically studied. Therefore, it is necessary to study a large unbiased sample of filaments. Such studies have recently become feasible because of modern multi-wavelength surveys, which cover the Galactic plane at high resolution and sensitivity.

Several catalogues of filamentary structures have been conducted in the last years, which can be divided in two groups. The filaments in the catalogues of Schisano et al. (2014); Koch & Rosolowsky (2015); Li et al. (2016) were identified from continuum data and therefore, miss the kinematic information, and might be affected by line-of-sight projection effects. The catalogues of Ragan et al. (2014); Zucker et al. (2015); Abreu-Vicente et al. (2016); Wang et al. (2015, 2016) concentrate on the longest filamentary structures in the Galaxy. While the identification methods and criteria vary in these studies, all filaments are tested for a velocity coherent behaviour.

In this study, we target the largest catalogue of filamentary structures published so far (Li et al. 2016), which is based on the ATLASGAL survey at 870μm (Schuller et al. 2009). As these structures were identified in continuum dust emission data, the scope of this work is to use the SEDIGISM data (Schuller et al. 2017) to assess their velocity structure. Because of the large number of targets, it is necessary to perform the analysis in a fully-automated way, which will be also presented in this work.

In this paper, we will refer to the structures identified by Li et al. (2016) as filament candidates. After the analysis of their velocity structure we will refer to the velocity coherent structures in the filament candidates as filaments, where one filament candidate can consist of multiple filaments. Some of these filaments may not meet the definitions of a filament, as they seem to be composed of a chain of dense clumps, or a dense clump with an elongated low column density environment. However, since filaments fragment, these structures could represent a late phase of evolution and should not be ignored.

The structure of the paper is as follows: Section 2 introduces the survey data used in this study and the targeted catalogue of filament candidates. The methods used to separate the velocity components of a given filament candidate and to derive its filament parameters are described in Section 3. In Section 4 we present the resulting statistics of the velocity separation and the interpretation of the kinematics. We then discuss in Section 5 the dependency of the filament mass with increasing radius, and the origin of the correlation found between the line-mass (mass per unit length) and velocity dispersion of the filaments. Finally, we summarize our results in Section 6.

2. Data and filament sample

2.1. Survey data

Within this paper, we will make use of three surveys: ATLASGAL (APEX Telescope Large Area Survey of the Galaxy, Schuller et al. 2009), ATLASGAL+PLANCK (ATLASGAL combined with PLANCK, Csengeri et al. 2016) and SEDIGISM (Structure, Excitation and Dynamics of the Inner Galactic InterStellar Medium, Schuller et al. 2017).

The ATLASGAL survey was conducted with the Large APEX Bolometer Camera (LABOCA) at 870 μm between 2007 and 2010 at the Atacama Pathfinder Experiment (APEX) telescope (Güsten et al. 2006) located on the Chajnantor plateau in Chile. The resolution of the survey is 19.2″ (6.0″ per pixel) with a 1σ RMS noise in the range of 40–70 mJy/beam. It covers the inner Galactic plane between $-80° \leq \ell \leq 60°$ and $|b| \leq 1.5°$. It is sensitive to the cold dust, and it traces mainly the high molecular hydrogen column density regions ($N_{\rm H_2} \geq 1.0 \times 10^{22}$ cm^{-2}) of the ISM.

As the ATLASGAL data is missing the large scale low column density emission due to sky noise subtraction, Csengeri et al. (2016) combined the survey with the data observed by the HFI instrument at 353 GHz (850 μm) with a resolution of 4.8′ on board the PLANCK satellite (Lamarre et al. 2010; Planck Collaboration et al. 2014). The combined ATLASGAL+PLANCK survey is sensitive to a wide range of spatial scales at a resolution of 21″ covering the same region as the original ATLASGAL data on the same pixel grid.

The SEDIGISM survey (Schuller et al. 2017) covers the inner Galactic plane between $-60° \leq \ell \leq 18°$ and $|b| \leq 0.5°$, which was observed from 2013 to 2016 with the SHeFI heterodyne receiver (Vassilev et al. 2008) at the APEX telescope. The prime targets of the survey are the ^{13}CO(2 – 1) and C^{18}O(2 – 1) molecular lines. The average root-mean-square (RMS) noise of the survey is 0.9 K ($T_{\rm MB}$) at a velocity resolution of 0.25 km s^{-1}, an FWHM beam size of 30″, and a pixel-size of 9.5″. For this analysis we use the first data release (DR1, Schuller et al. in prep.).

2.2. The ATLASGAL sample of filaments

Based on ATLASGAL, Li et al. (2016) produced a catalogue of filament candidates, which is the base for this study. The filaments were identified in the ATLASGAL only maps, after they were smoothed to a spatial resolution of 42″. The source extraction was performed with the DisPerSE (Discrete Persistent Structures Extractor, Sousbie 2011) algorithm, which is optimized for the identification of large spatially coherent structures, and has been successfully used to trace filaments in previous studies (e.g., Hill et al. 2011; Arzoumanian et al. 2011). Because of the limited sensitivity and resolution (minimal mean column density $N_{\rm H_2} = 1.6 \times 10^{21}$ cm^{-2}), the resulting catalogue is unlikely to be complete, however, as it covers a large fraction of the Galactic plane it is likely to include the full range of sizes and masses of filamentary type structures.

Not all of the identified structures are filamentary, but they cover a range of morphologies and complexity

from roundish clumps to large web-like structures. Therefore, the identified structures were categorized by Li et al. (2016) through visual inspection into six groups: unresolved clumps, marginally resolved elongated structures, filaments, networks of filaments, complexes, and unclassified structures. Here a filament was defined as single elongated linear structure with relatively few branches, an intensity clearly above the surrounding medium and an aspect ratio of at least 3, that is clearly resolved across its length and width. The high column densities found in the Galactic centre region lead to a higher probability of identifying more complex structures. Therefore, the number of filament candidates in the catalogue is lower towards the Galactic centre. This classification resulted in a catalogue of 517 filament candidates, providing the starting point of this study. For more details about the filament identification see Li et al. (2016). In the following, we will refer to the structures of the catalogue as filament candidates, as they have been identified only in position-position space, which leaves the possibility of line-of-sight projection effects. One of the objectives of this study is to investigate their velocity coherence.

3. The automated filament analysis

The SEDIGISM survey covers the Galactic plane between $-60° \leq \ell \leq 18°$ and $|b| \leq 0.5°$, which is only a part of the ATLASGAL survey. Therefore, we analyse the 283 filament candidates in the area covered by all three surveys described in section 2.1. This corresponds to $\sim 55\%$ of the total number of filaments, and can therefore be considered representative of such structures in the inner Galactic plane.

Because of the large number of filament candidates, it is necessary to use an automated approach to analyse them. However, as the sample is distributed over a large range of Galactic longitudes, it is unlikely to find homogeneous conditions in their surrounding material. Therefore, we choose a robust and efficient method to analyse the data in a systematic way, which leads to the following decisions for the analysis. We use the calculation of moments instead of multi-Gaussian fitting to identify the kinematics of the filaments. Also, we do not truncate or alter the skeletons of the filament candidates to fit the identified filaments more accurately, but rather neglect parts where we do not detect molecular gas. Therefore, there are two sets of pixels for a filament candidate used in the analysis: One that describes only the skeleton for the calculation of the kinematics and one that includes also the surrounding area within a dilation box with diameter of three beams used for the structure correlation. This approach results in larger uncertainties in the derived properties, but the homogeneous method enables the finding of correlations in the large scale properties of the filaments, which is the aim of this work.

From Li et al. (2016) we have a set of positions defining the skeleton of each filament, which trace the highest ATLASGAL intensities, that form the backbone of the structure. For each candidate we extract the data around the skeleton from the surveys using a rectangular box that is 5′ larger on each side than the extrema of the skeleton points. This showed to be sufficient for the analysis of the most nearby < 2 kpc filaments, where the angular extend of the structure is the largest. We now describe the analysis performed on every filament candidate.

3.1. The filament skeleton

For the analysis of each filament candidate we first have to transfer the skeleton coordinates (Fig. 1) onto the SEDIGISM grid. To do so, we check whether all positions of the skeleton are covered by the SEDIGISM observations, and remove the positions if they are not covered. This allows us to continue with structures that are partially truncated by the data limits. Then we overlay the skeleton coordinates on the pixel grid of the molecular line data. We mark the pixels within a dilation box around each pixel that covers a position of the DisPerSE skeleton as part of the new pixel skeleton. The size of the dilation box is set to be larger than the maximum distance between two neighbouring skeleton points. Here a width of 1 pixel (9.5″) is sufficient. As the resulting skeleton mask might have a width larger than one pixel, we use the thinning algorithm of Gonzalez & Woods (1992) to truncate the pixel skeleton. The result is a "chain" of pixels which might have several branches (see Fig. 2).

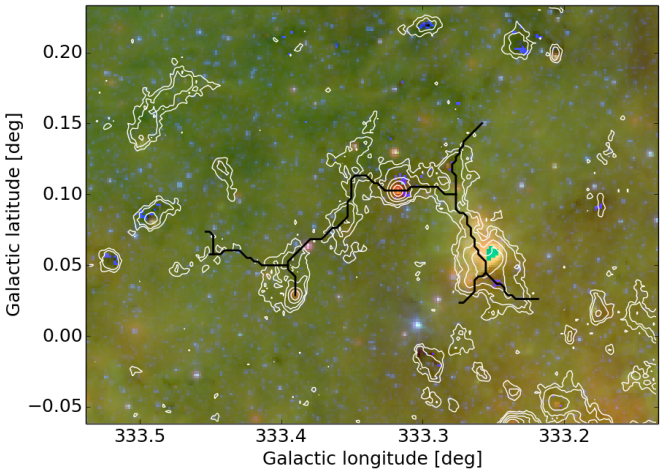

Fig. 1. ATLASGAL contours (0.05, 0.1, 0.2, 0.5, 1.0, 2.0 Jy/beam) and skeleton derived by DisPerSE for the filament candidate G333.297+00.073, overlaid on an infrared three color image of the field (red: MIPSGAL 24 μm; green: GLIMPSE 8.0 μm; blue GLIMPSE 3.6 μm.

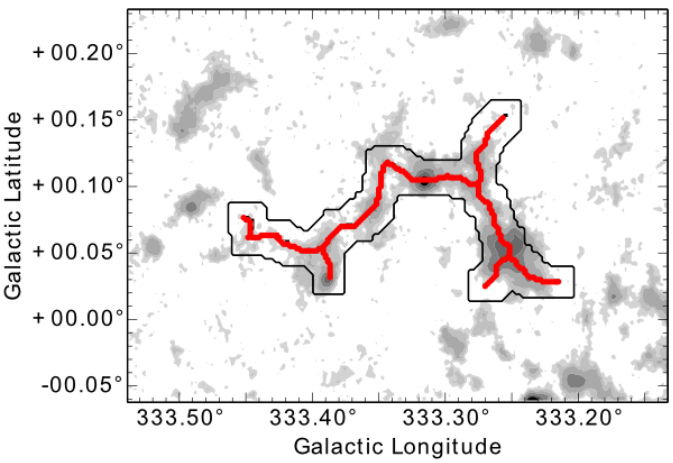

Fig. 2. The skeleton of the filament candidate G333.297+00.073 derived by DisPerSE on top of the ATLASGAL grayscale contour map. The black contour indicates the dilation box used for the correlation in Section 3.3.

3.2. Identification of velocity components

In order to investigate whether the filament candidates form a single structure in velocity, spectroscopic observations are indispensable. From a study of filaments in the SEDIGISM first science field (7 filament candidates in 1.5 deg^2, Schuller et al. 2017), we know that one can observe line emission at very different velocities towards one continuum structure due to projection effects through the Galactic plane. Therefore, we average all spectra located on the skeleton and identify the velocity ranges that show emission peaks in this spectrum. To identify the velocities we smooth the average spectrum with a Gaussian kernel with a dispersion of 4 channels ($= 1\,\mathrm{km\,s^{-1}}$) to reduce the noise. In case the signal-to-noise ratio (SNR) is low, peak intensity $\leq 5\sigma$, we double the kernel width. We then define the velocity range of each spectral component in the averaged spectrum as that between which the emission attains more than the 1σ noise level. This leaves us with a minimum separation limit of $\delta v_{\mathrm{min}} = 2.5\ \mathrm{km\,s^{-1}}$, which is described in detail later on. Furthermore, we only consider components with an SNR ≥ 5 in their integrated intensity of the original data (for example, see Fig. 3).

We then define the ends of the velocity components where the emission peaks of the average spectrum exceeds the 1σ noise level, so the emission peak is not likely to be truncated, and accept only components with an integrated intensity SNR ≥ 5 (for example Fig. 3). The above procedure is only applied to the ^{13}CO data because of their higher SNR. The C^{18}O emission lines are narrower than the ^{13}CO data lines and so we use the same velocity ranges to calculate the moments in the C^{18}O data. Thereafter, we calculate the zeroth, first, and second 'order' moment of each velocity component, that indicate the integrated intensity, peak velocity, and velocity dispersion, respectively, for both molecules. This gives us a first impression of the kinematics of the filament.

Separating the velocity components of a filament along the line-of-sight is a crucial part of this work. Therefore, the technique of identifying the velocity range of emission needs to be tested in a systematic way. We created a simulated data cube with an RMS noise per position of 1 K, typical for SEDIGISM, and include two filaments at the same 2D location, with the same velocity dispersion and intensity, but with different peak velocities. For the emission of the filaments, we assume a Gaussian line profile. We then vary the peak-to-peak velocity, the linewidth, and the intensity and analyse these cubes in exactly the same way as the observed data. From this modelling, we find for filaments with a signal-to-noise SNR > 4, which is typical for our ^{13}CO data (channel width 0.25 $\mathrm{km\,s^{-1}}$), that the minimal separated peak-to-peak velocity $(\delta v)_{\mathrm{min}}$ depends linearly on the velocity dispersion σ_{v} like,

$$(\delta v)_{\mathrm{min}} = 2\sigma_{\mathrm{v}} + 1\ \mathrm{km\,s^{-1}}\ , \qquad (1)$$

shown in Fig. 4. Emission lines with a velocity dispersion of $\sigma_{\mathrm{v}} < 0.75\ \mathrm{km\,s^{-1}}$ (3 channels) are not identified as an emission line. For filaments with low intensities (SNR ≤ 4) and for different intensities these limits must be degraded by $\Delta\sigma_{\mathrm{v}} = 0.25\ \mathrm{km\,s^{-1}}$. Note, as the identification is done on the average spectrum over the filament skeleton, the velocity dispersion of an emission line can be larger than the intrinsic value because of velocity gradients along the skeleton. As a result, we are not resolving the kinematic substructure, like fibres (δv $\approx 1.0\ \mathrm{km\,s^{-1}}$, Hacar et al. 2013), but can determine the large scale kinematics of the filament.

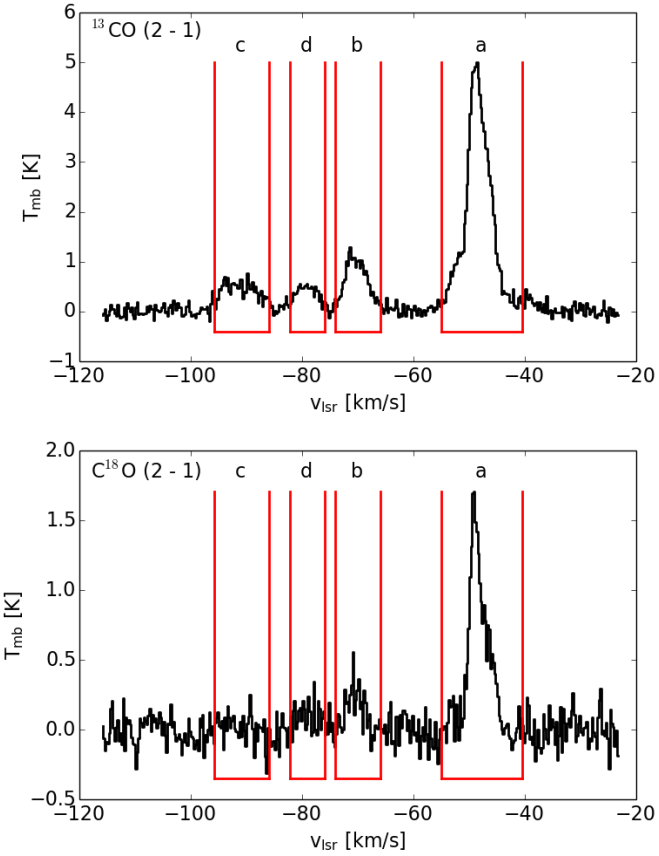

Fig. 3. Average ^{13}CO (top) and C^{18}O (bottom) spectrum over the skeleton of filament candidate G333.297+00.073 (see Figs. 1 and 2). The red lines mark the identified emission intervals named by letters.

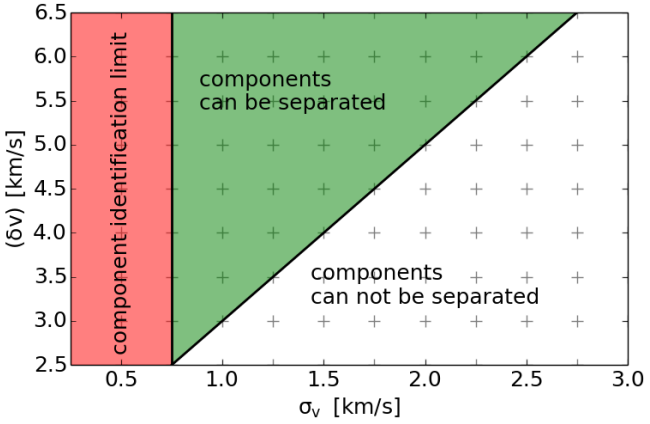

Fig. 4. Component separation limits dependent on the velocity dispersion of the two velocity components. The crosses indicate the modelled data points

From previous studies (Schuller et al. 2017) we know that ^{13}CO is likely to be optically thick towards the densest regions, which might lead to effects like self-absorption, and could affect the separation method. As the abundance of C^{18}O is lower by ^{13}CO /C^{18}O $= 8.3$ (Miettinen 2012), it

is likely to be optically thin over the whole filament. During visual comparison of the ^{13}CO and C^{18}O spectra of all 604 ATLASGAL clumps within the filaments (position and velocity) optically thick ^{13}CO emission is seen in 76 clumps, corresponding to 13%. However, these clumps do not show a significant effect on the average spectrum over the whole skeleton. Hence, our method is unlikely to separate velocity components because of self-absorption features. Additionally, we conclude that the contribution of the dense core emission is small when compared to the emission integrated up over the whole filament.

In the next step we use the same method as for the average spectrum on every spectrum/pixel along the skeleton within the identified velocity ranges. In this way we identify which part of the skeleton is detected in the different velocity components. Velocity components in which less than ten positions of the skeleton are detected in ^{13}CO are discarded, as these barely deviate from the noise, and we ensure a minimal elongated shape for all correlated structures (aspect ratio of 3 assuming a width of one beam). Additionally, we are able to detect multiple velocity components within the previously identified velocity range towards individual pixels. In the case where several velocity components are found, we only keep the calculated moments for the one with highest intensity. This is done for the ^{13}CO and C^{18}O data. The separation of these subcomponents is limited by the smoothed velocity resolution. Also, we calculate the zeroth, first, and second 'order' moments of skeleton pixels in each detected velocity component. With the first order measurements we potentially trace velocity gradients along the spine, but this is beyond the scope of this paper. However, the second order measurements, hence the velocity dispersion, of one pixel includes only the velocity gradient within one beam, which can be considered to be small. Therefore, the average over the skeleton pixels is a better estimate of the velocity dispersion of a filament than the value derived from the average spectrum and used in the further analysis. To check the results of these calculations we plot the derived moments on top of the position-velocity diagram of the filament candidate skeleton (Fig. 5). Additionally, we integrate over the velocity ranges of each velocity component; see Fig. 6.

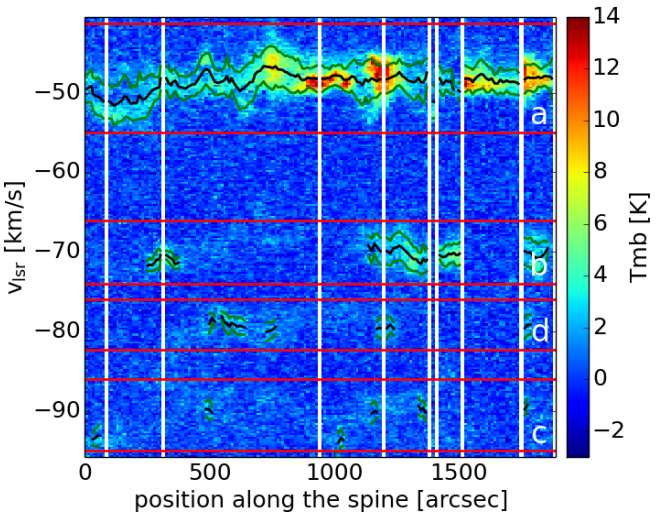

Fig. 5. Position-velocity plot of the intensity along the skeleton of the filament candidate G333.297+00.073. The white stripes indicate the beginning/end of a skeleton branch. The first five branches show the longest connection through the skeleton from higher to lower galactic longitude and the last four are the branches to the side in the same direction. The horizontal red lines mark the identified emission intervals shown in Fig. 3 with intervals a, b, d, c from top to bottom. The jagged black and green lines mark the per pixel measured peak velocity and the 1σ interval of the detected emission peak.

3.3. Gas-dust correlation

We further estimate how much each velocity component contributes to the overall dust emission from a given filament candidate. We smooth and re-grid the ATLASGAL maps, which were used for the candidate identification, to the resolution ($30.1''$) and pixel-grid ($9.5''$) of the SEDIGISM cubes. For comparison with the ^{13}CO integrated emission we restrict the maps (ATLASGAL and integrated ^{13}CO intensities per velocity component) to an area within a dilation box around the skeleton with a width of 3 beams (9 pixels), which covers the emission seen in ATLASGAL. We scale the ATLASGAL intensities with the minimum and maximum value to an interval of [0–1], using

$$I_s^{\rm dust} = \frac{I^{\rm dust} - \min(I^{\rm dust})}{\max(I^{\rm dust}) - \min(I^{\rm dust})} \ , \qquad (2)$$

where $I_s^{\rm dust}$ are the scaled ATLASGAL intensities, and $I^{\rm dust}$ the original ones, and min() and max() describe the minimal and maximal value of the pixel intensities within the dilation box. As the ATLASGAL emission traces only the small scale high density gas, the minimun value is typically around 0 Jy/beam. For the ^{13}CO data we define the intensity integrated over the velocity range of component i as $I^{\rm gas}(v_i) = \int_{v_i} T_{\rm mb}(v)\, dv$, where $T_{\rm mb}(v)$ is the main beam temperature, and v_i is the velocity interval of one component as defined before. Also, for the correlation we do not apply any threshold. We use for the scaling the maximum and minimum value within the dilation box of the sum over the integrated intensity maps of all velocity components,

$$I_s^{\rm gas}(v_i) = \frac{I^{\rm gas}(v_i) - \min(\sum_i I^{\rm gas}(v_i))}{\max(\sum_i I^{\rm gas}(v_i)) - \min(\sum_i I^{\rm gas}(v_i))} \ , \qquad (3)$$

where $I_s^{\rm gas}(v_i)$ are the scaled ^{13}CO intensities of the velocity component i, and $I^{\rm gas}(v_i)$ are the original ones. Assuming a constant gas-to-dust ratio, the ATLASGAL maps should correlate with the molecular line emission integrated over all velocity components. We perform pixel-to-pixel correlation between the scaled ATLASGAL maps and the scaled integrated ^{13}CO maps of one velocity component using the same dilation box mask. Therefore, in cases of multiple components per candidate we will not find a one-to-one correlation, but we identify which velocity component shows the filamentary behaviour seen in dust emission. Additionally, noise in the observations and effects like CO depletion will affect the correlation plot. See Fig. 7 and appendix A for examples.

We analyse these correlation diagrams as follows. We calculate the standard deviation of the total (scaled) integrated intensities, $\sigma_{\rm gas} = \sigma(\sum_i I_s^{\rm gas}(v_i))$, presenting an upper limit of the noise in the gas emission, and the standard deviation of the correlation, $\sigma_{\rm cor} = \sigma(I_s^{\rm dust} - \sum_i I_s^{\rm gas}(v_i))$. To estimate the intensity contribution of one velocity com-

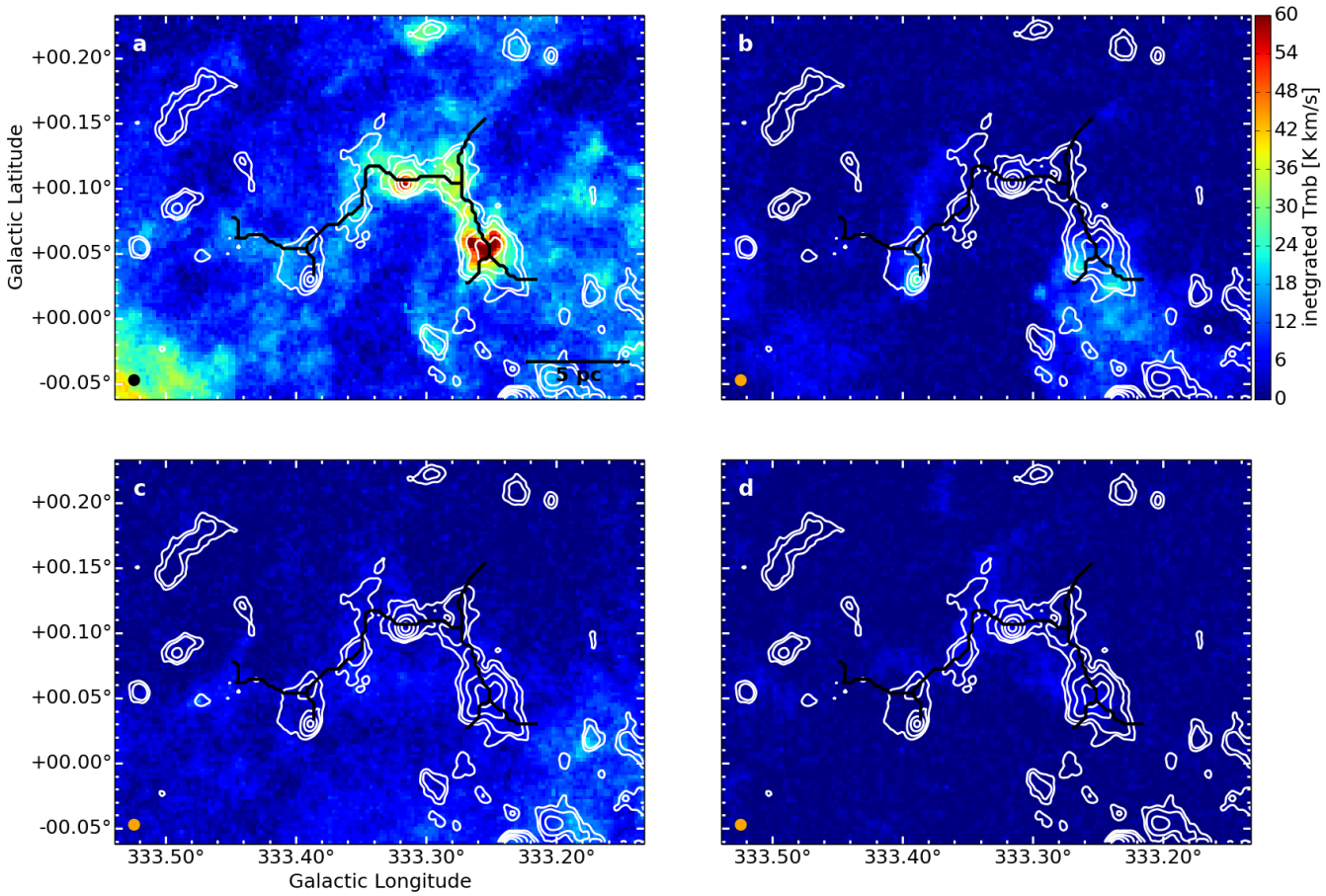

Fig. 6. Integrated ^{13}CO(2 − 1) emission of the four velocity components of the filament candidate G333.297+00.073. The intensity was integrated over the velocity ranges −55.0 to −40.5 km s^{-1} (top left), −74.0 to −66.0 km s^{-1} (top right), −96.0 to −86.0 km s^{-1} (bottom left) and −82.5 to −76 km s^{-1} (bottom right). The beamsize is indicated by the circle in the lower left and the contours show the ATLASGAL [0.1, 0.2, 0.5, 1.0, 2.0] Jy/beam levels. The letters in the upper right refer to the marked intervals in Fig. 3.

ponent, we perform a linear fit with a slope of 1 on the data points with $I_s^{\rm gas}(v_i) \geq \sigma_{\rm gas}$. We then derive the percentage of data points, which are above the $\sigma_{\rm gas}$ noise , $p_{\rm gas}$, which are within $\pm\sigma_{\rm cor}$ from the linear fit (red in Fig. 7), $p_{\rm cor}$, and which meet both conditions, $p_{\rm cor,\ gas}$. We then use these three parameters to characterize the different velocity components with the limiting values shown in Table 1.

Table 1. Limiting characterization parameters $p_{\rm gas}$, $p_{\rm cor}$, and $p_{\rm cor,\ gas}$ as described in Section 3.3. These parameters describe the population of three different areas in the correlation plots, see Fig. 7 and appendix A.

Status	$p_{\rm gas}$	$p_{\rm cor}$	$p_{\rm cor,\ gas}$
fully correlated	≥ 0.4		≥ 0.4
partially correlated	≥ 0.05		≥ 0.4
diffuse correlated	< 0.05	≥ 0.4	
uncorrelated (1)	≥ 0.05		< 0.4
uncorrelated (2)	< 0.05	< 0.4	

The limiting values for the characterization were obtained from the manual analysis of a test sample of filament candidates. This introduces a slight bias to the general analysis. The uncertainty of the characterization is difficult to determine, as the filament definition given by Li et al. (2016) can not be applied in a systematic way. Therefore, to get an objective, reproducible result, we decided to use this quantitative characterization over a visual approach as used by Li et al. (2016). A later visual inspection and different characterization will be possible, as all velocity components of all filament candidates, which are not uncorrelated, are handled in the same way in the subsequent analysis. Therefore, the characterization bias alters only the statistics of the characterization itself. However, the reliability of a filamentary shape decreases from fully correlated over partially correlated to diffuse structures, where partially correlated structures might not be continuous in position-position space, and diffuse structures might not show clearly enhanced emission from the surrounding. For simplicity we will still refer to all correlated structures as filaments. In total, we identified 422 filaments within the 283 filament candidates. More statistics of the characterization will be presented in Section 4.1 and 4.6.

3.4. Thermal and non-thermal motions

The unresolved kinematic motions in a molecular cloud can be estimated by the observed linewidth. The total velocity dispersion can be separated into a thermal and a non-thermal component. The thermal motions depend on the

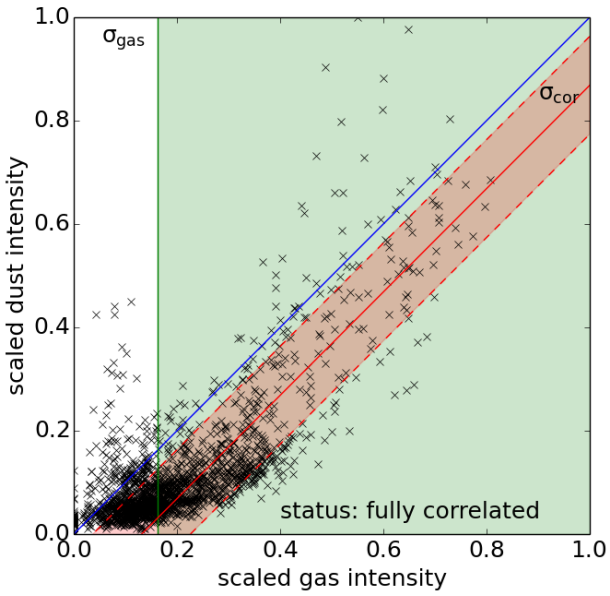

Fig. 7. Gas-dust correlation plot of the brightest velocity component ("a" in the spectrum shown in Fig. 3) of the filament candidate G333.297+00.073. The blue line gives the one-to-one correlation. The green area indicates values above the $\sigma_{\rm gas}$ limit ($p_{\rm gas} = 0.51$). The red line shows the fitting result, and the area within the dashed red lines marks the $\pm\sigma_{\rm cor}$ surrounding ($p_{\rm cor} = 0.80$). $p_{\rm cor,\,gas} = 0.70$ is estimated from the overlap of these areas.

observed molecule and gas temperature. For the molecular gas temperature we assume a typical value of $T = 15$ K (Pillai et al. 2006a; Wang et al. 2012, 2014), which is also in agreement with measured temperatures of ATLASGAL clumps (Urquhart et al. 2018). The non-thermal motions describe statistical motions of the gas, which are independent of the kinetic temperature of the the gas. The non-thermal velocity dispersion, $\sigma_{\rm nt}$, is given by

$$\sigma_{\rm nt}^2 = \sigma_{\rm x}^2 - \frac{k_B T}{m_{\rm p} m_{\rm x}} \,, \tag{4}$$

where $\sigma_{\rm x}$ is the measured second moment of ^{13}CO or C^{18}O, k_B the Boltzmann constant, $m_{\rm p}$ is the proton mass, and $m_{\rm x}$ is the molecular weight of the observed gas, here $m_{^{13}{\rm CO}} = 29$ and $m_{{\rm C}^{18}{\rm O}} = 30$. To derive the non-thermal velocity dispersion of the filament, $\sigma_{\rm nt}$, we average the measurements of each pixel along the skeleton, where we choose C^{18}O if it is detected and ^{13}CO otherwise. Therefore, this value is independent of velocity gradients along the skeleton, neglecting gradient effects within the beam, and it is less likely to be influenced by optical depth effects.

The thermal motion of the interstellar medium is given by the sound speed,

$$c_s = \frac{k_B T}{m_{\rm p} \mu} \,, \tag{5}$$

where $\mu = 2.8$ is the mean molecular weight of the mean free particle (Kauffmann et al. 2008), and other parameters as previously defined. The total velocity dispersion of a filament is given by $\sigma_{\rm v} = \sqrt{c_s^2 + \sigma_{\rm nt}^2}$.

3.5. Mass and length of filaments

To calculate physical parameters of the 422 filaments it is crucial to estimate the distance towards them. However, estimating distances towards extended and diffuse structures, like these filaments, is difficult. Especially, solving the ambiguity of kinematic distances. Therefore, we use a method similar to that discussed by Li et al. (2016), but including additional measurements.

As a first step we identify all ATLASGAL clumps (Contreras et al. 2013b; Urquhart et al. 2014) associated with the filaments. The distances towards these clumps have been estimated in Urquhart et al. (2018). As these estimates are based on kinematic distances, we must exclude the Galactic centre region ($|\ell| < 5°$), because of the large uncertainties. For filaments with an associated clump within the defined limits of the filament in position-position-velocity space) we simply assume the same distance. This provides distances for 222 filaments. In a second step we use friends-to-friends analysis to find adjacent clumps and adopt their distances for the filaments. This adds distances for another 114 filaments, but note the larger uncertainty for the distance estimate. For the friends-of-friends analysis we allow sources with a spatial offset of at most 10′ (with 90% closer than 5′) and a kinematic offset of at most 10 km s^{-1} (with 90% closer than 4 km s^{-1}). In total, we are able to assign a distance to 336 out of 422 filaments, including diffuse, partially correlated, and fully correlated ones. Additionally, we tested these estimates to be in agreement with (one of) the kinematic distances.

After we obtained the distances towards the filaments we can calculate their physical length. Here we take all pixels along the skeleton into account, towards which ^{13}CO was detected for the single filament. This allows us to get accurate measurements of the angular length for complex structures or partially correlated structures, including the detected branches, by adding up the length over each relevant pixel. However, because of a possible inclination of the structures, the derived physical measurements represent lower limits to their true length.

For calculating the area and the mass of the filaments we again use a dilation box. With the distances in hand we are able to use a physical box-diameter. Here we take the box-diameter as a free parameter and in Section 5.1 we discuss the dependency between the filament mass and box-diameter. For calculating the filament mass we assume its diameter to be of the order of the star-forming size scale. For a first order approximation of the star-forming size scale we use the previously measured velocity dispersion within a filament, $\sigma_{\rm v}$, and assume a star formation time of $T_{\rm sf} = 2$ Myr (Evans II et al. 2009). The size scale is then given by $s_{\rm sf} = \sigma_{\rm v} \cdot T_{\rm sf}$. As box-diameters are limited to discrete multiples of pixels, we interpolate linearly the values from measurements of the next bigger and smaller box size.

We estimate the area covered by the filament, by summing over all pixels within the dilation box of the integrated intensity maps, within which we detect ^{13}CO emission (SNR > 5). The same positions are used to estimate the filament mass. Here we follow two different approaches: First we use the integrated ^{13}CO emission, $W(^{13}{\rm CO})$, in combination with the ^{13}CO X-factor, $X_{^{13}{\rm CO}(2-1)} = 1^{+1}_{-0.5} \times 10^{21} {\rm cm}^{-2} ({\rm K\,km\,s}^{-1})^{-1}$ derived by Schuller et al. (2017). This has the advantage of tracing only the emission within the specific velocity component. The molecular hydrogen

column density, $N_i(H_2)$, in pixel i was then calculated by $N_i(H_2) = W_i(^{13}CO)X_{^{13}CO(2-1)}$. We then computed the mass using the equation

$$M(H_2) = \sum_i N_i(H_2) A_i \mu m_p \ , \quad (6)$$

where $N_i(H_2)$ is the H_2 column density computed for pixel i, A_i its area, $\mu = 2.8$ the mean molecular weight per H_2 molecule, and m_p the proton mass.

Second, we estimate the mass from dust emission maps of different surveys (ATLASGAL, ATLASGAL+PLANCK) using basic assumptions like a gas-dust ratio of $R = 100$, and a dust temperature of $T_D = 15\,K$ (Urquhart et al. 2018). The mass of the filament candidate is then computed through the equation

$$M_\nu(H_2) = \frac{S_\nu \, d^2 R}{B_\nu(T_D)\kappa_\nu} \ , \quad (7)$$

where S_ν is the integrated flux density at the frequency ν of the used survey, d is the distance towards the structure, $B_\nu(T_D)$ is the Planck function at the given dust temperature, and κ_ν is the dust absorption coefficient, which is $\kappa_{870\mu m} = 1.85\,cm^2\,g^{-1}$ for the ATLASGAL emission (Schuller et al. 2009; Ossenkopf & Henning 1994).

However, because of the contribution of the PLANCK data, the ATLASGAL+PLANCK survey traces not only the filament and the low column density gas around the filament, but also the diffuse Galactic dust emission, which ideally should be removed. To do so, we exclude the filament area of the maps using the inverse of the filament dilation box used previously. The remaining pixels should be dominated by non-filament emission. However, as the box has a width of three beams, we find a few cases in the most nearby (< 2kpc) filaments where the emission extends clearly beyond the mask. Therefore, we use the 20th percentile value of the non filament pixels as estimate of the diffuse Galactic dust emission. We then correct the ATLASGAL+PLANCK maps for the diffuse emission and estimate the masses as shown previously. In Section 4.7 we discuss the differences of the these three mass estimates based on dust continuum emission and compare them to the ^{13}CO emission estimate.

4. Results

4.1. Final Catalogue

Using the methods described in the previous section we derived a large set of filament parameters. With these parameters we created a catalogue of velocity coherent structures. The derived parameters of the catalogue are shown in Table 2, and the complete catalogue is shown in Tables 5 and 6. However, as several parameters are distance dependent, they cannot be calculated for the whole filament catalogue. The following description of the derived parameters includes only the structures with a distance estimate. The catalogue contains all 422 filaments of the 283 observed filament candidates, which show some correlation with the dust emission. In Table 3 we show the statistics of the characterization and the subsample for which we have distance estimates. The names of the structures are based on the initial filament candidate name from Li et al. (2016) and are extended by an integer starting from 0, indicating the velocity component.

4.2. Detection of filaments in ^{13}CO and $C^{18}O$

Out of the 283 ATLASGAL filament candidates within the SEDIGISM survey we detect correlated ^{13}CO emission for 260 filament candidates, which then show 422 velocity coherent (continuous kinematic structure, which cannot be resolved into separate components) filaments. We do not find a correlated ^{13}CO velocity component for 23 filament candidates, which is partially because of the sensitivity of the SEDIGISM survey, and partially because the candidates result from line-of-sight alignments of diffuse gas clouds. About 20% of the detected filaments show ^{13}CO emission at every position of the skeleton and for about 60% we detected ^{13}CO emission over at least half of the length of the skeleton. About 32% of the ^{13}CO detected filaments show no detection of $C^{18}O$ on the skeleton, about 13% have $C^{18}O$ detected over at least half of the skeleton, and for no filament $C^{18}O$ is detected over its entire length; see Fig. 8.

This difference in the detection rate is very likely due to the different abundances of the molecules ($^{13}CO/C^{18}O$ = 8.3; Miettinen 2012). The $C^{18}O$ line is expected to be weaker, resulting in a lower signal-to-noise ratio and the observed lower detection rate.

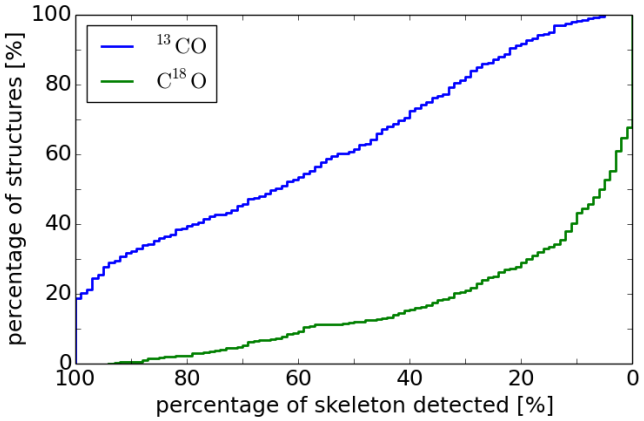

Fig. 8. Cumulative histogram of the percentage of filament candidate skeletons detected in ^{13}CO (blue) and $C^{18}O$ (green).

4.3. Galactic distribution

Using the distance estimates we can derive the Galactocentric coordinates and plot the positions onto a face-on artist's impression of the Milky Way (Fig. 9). We find that a large fraction of the filaments are likely to be associated with the near Scutum-Centaurus arm. We also find some filaments located in the near Sagittarius arm, the near and far 3-kpc arm, and the near Norma arm, but also in some inter-arm regions. Note, we do not have distance estimates for the Galactic Centre region ($|\ell| \leq 5°$).

Histograms representing positions of the detected filaments with Galactic longitude and latitude are shown in Figs: 10 and 11, respectively. The distribution with Galactic longitude shows a peak around $l = -21°$ with a strong decrease towards the outer Galaxy (only 14 structures for $l < -45°$), and a decrease towards the Galactic centre. As the filament candidates were identified in the ATLASGAL maps that trace only high column density dust emission, it is more unlikely to find filaments towards the outer Galaxy, which contains fewer dense molecular cloud regions. How-

Table 2. Descriptions of the derived parameters. The complete catalogue is shown in Tables 5 (top) and 6 (bottom).

Parameter	Unit	Description
		Table of measured parameters
Filament ID		
ℓ	$^\circ$	Galactic longitude of the centre of the filament
b	$^\circ$	Galactic latitude of the centre of the filament
Status		correlation with the ATLASGAL emission
N_c		number of detected velocity components in the original filament candidate
$v_{lsr}(^{13}CO)$	km s^{-1}	peak velocity derived from the ^{13}CO average spectrum
$v_{lsr}(C^{18}O)$	km s^{-1}	peak velocity from the C^{18}O average spectrum
$\sigma(v_{^{13}CO})$	km s^{-1}	dispersion of the ^{13}CO peak velocities along the skeleton
$\sigma(v_{C^{18}O})$	km s^{-1}	dispersion of the C^{18}O peak velocities along the skeleton
σ_v	km s^{-1}	average total velocity dispersion along the skeleton (derived from ^{13}CO and C^{18}O)
$\sigma_v(^{13}CO)$	km s^{-1}	average ^{13}CO velocity dispersion along the skeleton
$\sigma_v(C^{18}O)$	km s^{-1}	average C^{18}O velocity dispersion along the skeleton
$\sigma_{v,t}(^{13}CO)$	km s^{-1}	^{13}CO velocity dispersion derived from the average spectrum
$\sigma_{v,t}(C^{18}O)$	km s^{-1}	C^{18}O velocity dispersion derived from the average spectrum
		Table of derived parameters
Filament ID		
d	kpc	distance from the Sun
l	$^\circ$	angular length of the detected skeleton
$l(d)$	pc	physical length of the detected skeleton
M(ATG)	M$_\odot$	filament mass derived from ATLASGAL emission
M(ATG+P)	M$_\odot$	filament mass derived from ATLASGAL+PLANCK emission
M(dust)	M$_\odot$	filament mass derived from corrected ATLASGAL+PLANCK emission
$M(^{13}CO)$	M$_\odot$	filament mass derived from integrated ^{13}CO emission
$m_{crit,nt}$	M$_\odot$ pc^{-1}	critical, non-thermal line-mass
m_{obs}	M$_\odot$ pc^{-1}	observed line-mass
det. ^{13}CO		fraction of the skeleton detected in ^{13}CO
det. C^{18}O		fraction of the skeleton detected in C^{18}O
edge flag		skeleton truncated because of the edge of SEDIGISM
d flag		indicating the method for the distance estimate: 0 no distance; 1 inside ATLASGAL source; 2 nearby ATLASGAL source

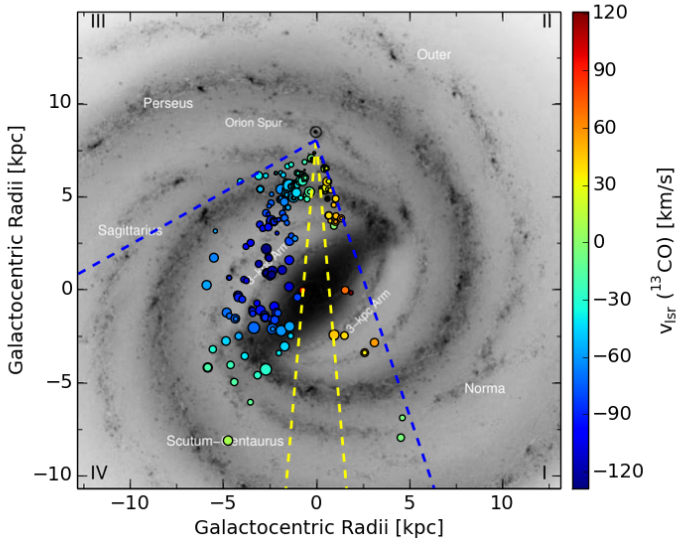

Fig. 9. The filaments with distance estimated are plotted onto an artist's impression of the Milky Way (Robert Hurt), the size is indicating the length of the filament, and the colour indicates the ^{13}CO velocity. The yellow lines mark the range $|\ell| \leq 5^\circ$, where distances are uncertain and the blue lines mark the SEDIGISM survey limits.

Table 3. Number of sources (with distance estimate) separated in different groups.

Groups	total	with dist.
filament candidates (Li et al. 2016)	517	
in SEDIGISM area	283	
≥ 1 correlated velocity component	260	
total velocity components	812	336
uncorrelated components	390	
filaments	422	336
fully correlated filaments	180	151
partially correlated filaments	191	148
diffuse component filaments	51	37

ever, the number of filaments is also suppressed in the direction of the Galactic centre, where identification is difficult because many structures along the line-of-sight are confused, and were categorized as networks, complexes or unclassified, such as the Galactic centre region (Li et al. 2016). Nevertheless, comparing the distribution of filaments to the distribution of ATLASGAL clumps presented by (Beuther et al. 2012, Fig. 3) and (Csengeri et al. 2014, Fig. 16) shows similarities for the location of peaks, indicating a possible correlation with active star-forming regions.

The distribution of the detected filaments with Galactic latitude (Fig. 11) shows a broad, almost flat behaviour similar to the findings of Li et al. (2016). However, we find the

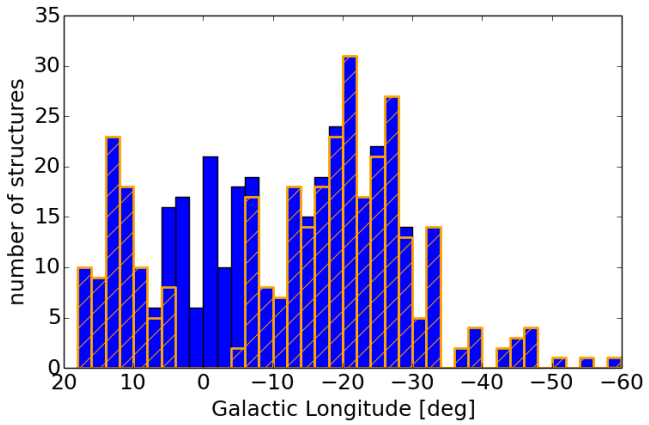

Fig. 10. Distribution of the filament positions in Galactic Longitude. The orange hatch marks the filaments with distance estimate.

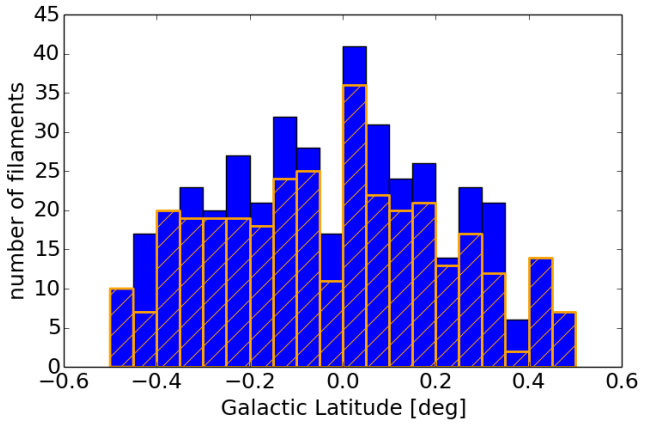

Fig. 11. Distribution of the filament positions in Galactic Latitude. The orange hatch marks the filaments with distance estimate.

peak and mean ($\langle b \rangle = +0.02°$) of the distribution aligned with the Galactic mid-plane, which is in contrast to the general finding of more sources for $b < 0.0°$ than for $b > 0.0°$ (Beuther et al. 2012; Li et al. 2016). Note, our sample is not identical with that of Li et al. (2016), as we use only a sub-sample of their filament candidates and split some of these candidates in different velocity components, hence filaments.

4.4. Distributions of velocity dispersion, mass, length and distance

In the following, we give a short overview on the most interesting measured properties of the filaments, which are the non-thermal velocity dispersion along the skeleton, the mass derived from the ^{13}CO emission, and the length of the filament, which we define as the sum over the detected parts of the skeleton.

For the calculation of the total velocity dispersion we assumed an isothermal medium of 15 K, see Section 3.4. The distribution of the resulting values is shown in Fig. 12. We find values reaching from about 0.5 km s^{-1} to 2.5 km s^{-1} with a relatively flat center between 0.8 km s^{-1} and 1.4 km s^{-1}, and a mean of about 1.17 km s^{-1}. Concentrating on the 180 fully correlated, hence, the most reliable filaments, we find a similar distribution with the mean at about 1.20 km s^{-1}. In general, these values are higher than what Arzoumanian et al. (2013) find in nearby filaments ($\sigma_v \approx 0.3$ km s^{-1}), but in agreement with studies of similar (more distant and more massive) objects like the DR21 filament (Schneider et al. 2010).

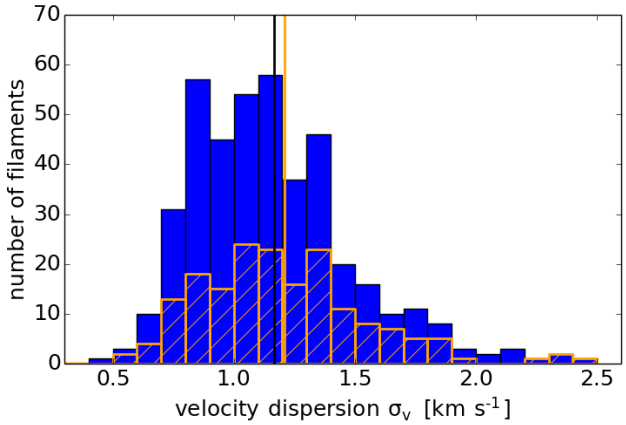

Fig. 12. Distribution of the measured total velocity dispersion of all filaments (blue). The fully correlated filaments are marked by the orange-coloured hatched area. The vertical lines indicate the mean value for the complete (black) and the sub-sample (orange).

For the logarithmic distribution of the calculated masses, Fig. 13, we find a flat part between 1800 $M_\odot$ and 18000 $M_\odot$ with a mean mass of 8600 $M_\odot$. Again the distribution of the fully correlated filaments (151 with distance estimate) is similar to the complete distribution with a mean of 11000 $M_\odot$. For comparison we also show the mass ranges covered by other filament catalogues (Ragan et al. 2014; Wang et al. 2015; Zucker et al. 2015; Abreu-Vicente et al. 2016; Wang et al. 2016) and the study of Contreras et al. (2013a). These studies report filaments with similar or higher masses. However, several of these studies have tried to identify the largest structures in the Galaxy and therefore, are biased to larger structures. As a result, some filaments mentioned in this study are only parts of structures in the other catalogues. Also, we find filaments that are almost identical in several catalogues, like G11.046-00.069_2 (Snake) or G332.370-00.080_1.

We also find overlap between the catalogues for the lengths of the filaments (Fig. 14), where the shortest filaments of the other studies are as long as the mean of our sample (10.3 pc all, 11.1 pc fully correlated). In general, we cover the range from 2 pc to 100 pc with a peak around 8 pc.

Most filaments are found within 5 kpc from the Sun (Fig. 15), which is also the area where the other surveys found the long filaments. This area includes parts of the nearby Sagitarius and Scutum-Centaurus spiral arms. Another peak in the distance distribution is found at around 10 kpc, which is about the distance of the connection point of the Galactic bar with the Perseus spiral arm (see also Fig. 9).

Plotting the filament lengths against the estimated distances separated by the categories (Fig. 16), we find that especially the fully correlated filaments follow the distance distribution, while the others are more equally distributed.

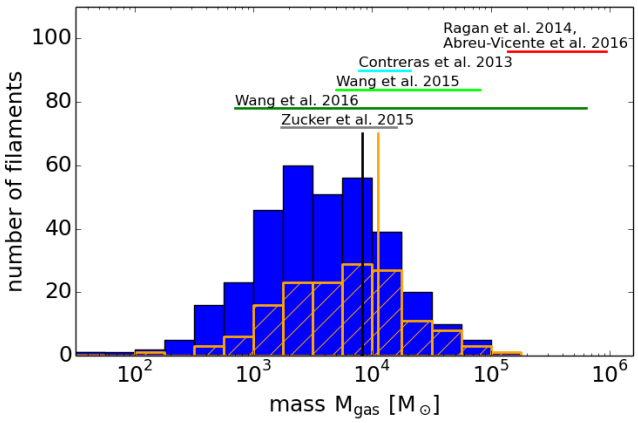

Fig. 13. Distribution of the measured mass based on ^{13}CO of all filaments (blue). The fully correlated filaments are marked by the orange hatch. The vertical lines indicate the mean value for the complete (black) and the sub-sample (orange). The horizontal lines mark the mass ranges measured by the studies mentioned above the lines.

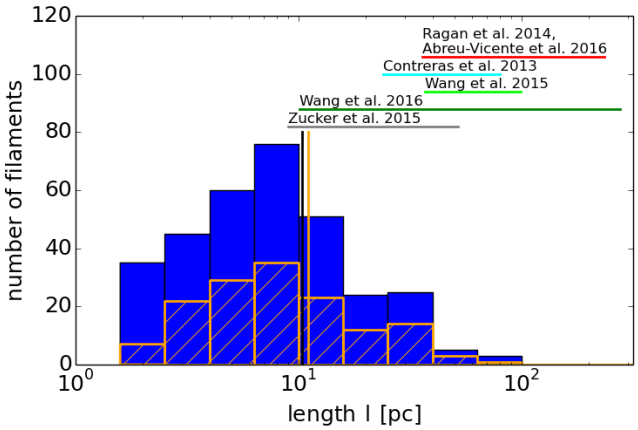

Fig. 14. Distribution of the measured length over the detected skeleton of all filaments (blue). The fully correlated filaments are marked by the orange hatch. The vertical lines indicate the mean value for the complete (black) and the sub-sample (orange). The horizontal lines mark the length ranges measured by the studies mentioned above the lines.

Also, we find no correlation between the longest filaments and the distance. This results in a larger scatter of lengths for a given distance. The shortest filaments reproduce our minimal length criteria of at least 10 pixels.

4.5. ^{13}CO – C^{18}O *velocity comparison*

As mentioned before, C^{18}O is less abundant than ^{13}CO and traces mainly the bright, dense parts of the filaments, where ^{13}CO is likely to be optically thick. However, to combine the kinematics of the two lines we need to be sure that both trace the same gas. Therefore, Fig. 17 shows the distribution of the absolute difference between the ^{13}CO and C^{18}O peak velocities of each filament derived from the average spectrum along the full skeleton, which is supposed to be zero if both istotopologues trace the same gas. The logarithmic distribution shows a plateau between 0.17 km s^{-1} and 1.0 km s^{-1} and decreases steeply to both sides. Additionally, we find the largest difference in filaments with a

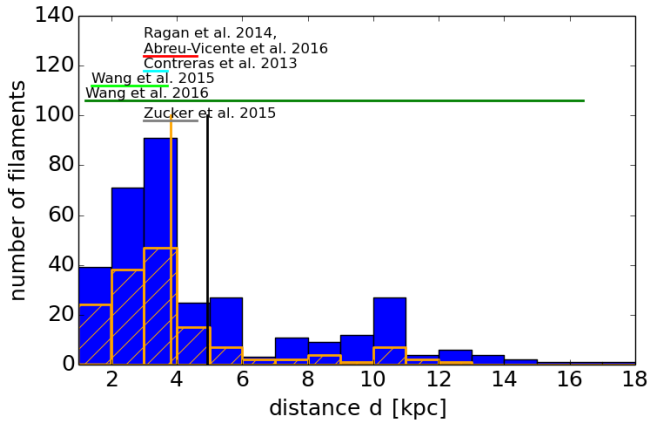

Fig. 15. Distribution of the estimated distances of all filaments (blue). The fully correlated filaments are marked by the orange hatch. The vertical lines indicate the mean value for the complete (black) and the sub-sample (orange).

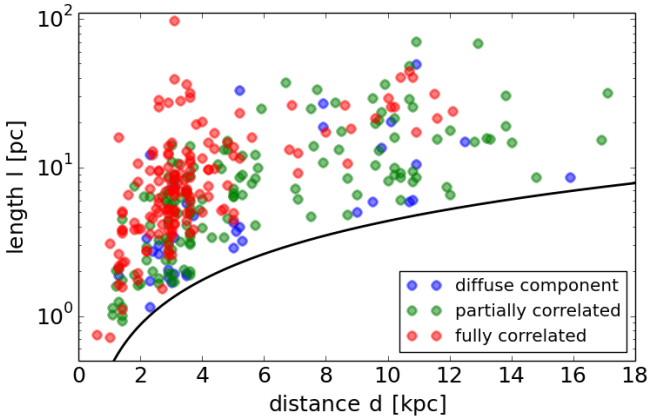

Fig. 16. Filament length plotted against the estimated distance. The three filament categories are indicated by blue, green, and red for diffuse component, partially correlated, and fully correlated, respectively. The black line shows the criteria of a minimum length of 10 pixels.

signal-to-noise of the C^{18}O average spectra of SNR < 5. In general, low SNR filaments peak at higher velocity differences (red).

We compare the observed distribution to a model distribution given by the mean velocity dispersion along the filament $\overline{\sigma}_{\rm v} = 1.17$ km s^{-1} (see Section 4.4 and Fig. 12). Given the wide distribution of velocity dispersions this model gives only a first order impression of the expected distribution. We model the absolute difference between two velocities drawn from two Gaussian distributions. The dispersion of the differences is then given by $\sigma_{\delta v} = \sqrt{\overline{\sigma}_{\rm v}^2 + \overline{\sigma}_{\rm v}^2} = \sqrt{2}\,\overline{\sigma}_{\rm v}$. We generate an artificial difference distributions, using 10,000 draws to avoid statistical noise, bin the absolute values of the sample like the observed differences, and scale the height by 0.0373 to get a comparable total number of filaments as our sample. The resulting distribution (orange hatched in Fig. 17) does not agree with the observed one, as it is shifted to larger differences.

To further investigate this trend, we reduced the dispersion of the underlying velocity distribution until we found a distribution that matched the differences (black hatched) area. Its velocity dispersion is $\sigma_{\rm v}$(model) $= 0.35$ km s^{-1},

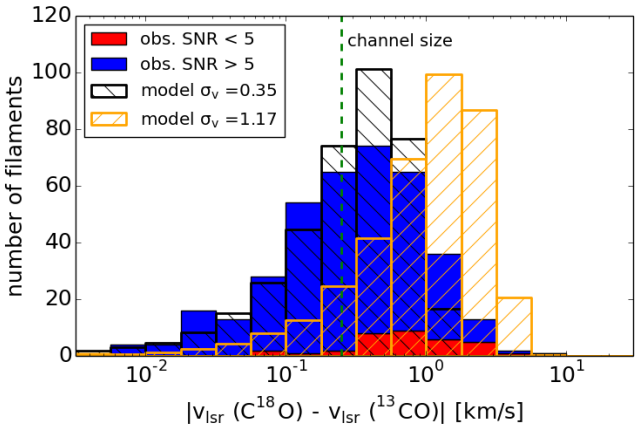

Fig. 17. Histogram of the absolute velocity difference. Sources with SNR < 5 are shown in red. On top the model difference distributions given by a underlying Gaussian velocity distribution with a dispersion of 1.17 km s^{-1} (orange) and 0.35 km s^{-1} (black) are shown. The green dashed line indicates the velocity channel size of the data.

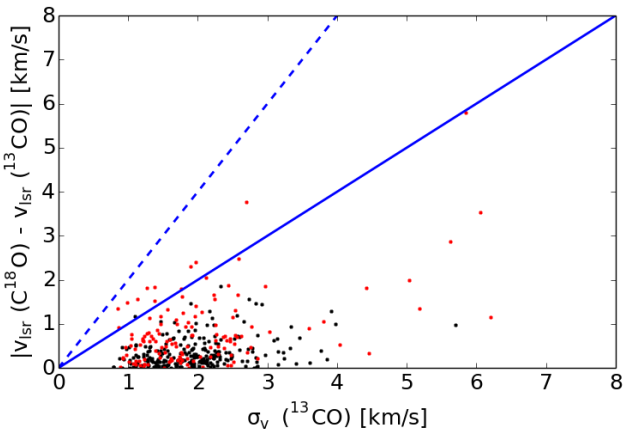

Fig. 18. Plot of the absolute velocity difference against the velocity dispersion of the filament, where filaments with a $C^{18}O$ detection rate below 10% are indicated in red. The blue lines show the one-to-one (1σ, solid) and two-to-one (2σ, dashed) relations.

which is about $\sqrt{2}$ times the channel width (0.25 km s^{-1}). We speculate therefore, that this distribution is likely to arise from the sampling of the spectra.

However, we also see some filaments that show a larger difference between the ^{13}CO and $C^{18}O$ peak velocities than can be expected by the channel-width introduced sampling issues. For these filaments we speculate that they show a gradient along the skeleton and are only partially detected in $C^{18}O$. To investigate this, we plot the velocity difference against the ^{13}CO velocity dispersion of the average spectrum (Fig. 18), as gradients along the skeleton result in a higher velocity dispersion. Additionally, filaments for which less than 10 % of the skeletons are detected in $C^{18}O$ are marked in red. We find that almost all filaments fall below the one-to-one line and that all velocity differences are smaller than $2\sigma_v(^{13}CO)$. We also see that 31 out of 43 filaments with a velocity difference larger than 1 km s^{-1} show low $C^{18}O$ detection rates.

In summary we rule out systematic differences between the kinematic of the isotopologues. The observed differences are based on observational limitations, like the velocity resolution and sensitivity.

4.6. Multiplicity in velocity space

Filamentary structures are often identified in continuum emission maps. But it is unknown whether these structures are actual continuous filaments or only an effect of line-of-sight projection of multiple velocity components. We address this question with our data.

The 260 detected filament candidates split up in 422 velocity coherent filaments in total. Kinematic subcomponents are identified in single spectra for 14 of the filaments, but will not be discussed any further as more detailed studies will be needed. Analysis of the velocity components shows that about 58% of the filament candidates exhibit one velocity component. Another significant fraction of the filaments, 27% and 12%, have 2 or 3 components, respectively. 6 filaments have 4 or more velocity components with a maximum of 7 components, seen in only one filament (Fig. 19).

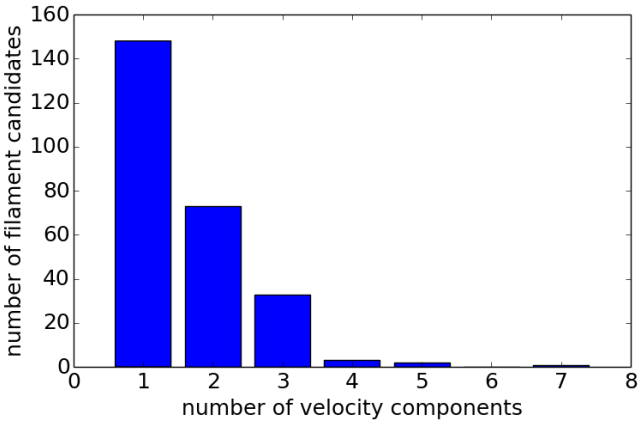

Fig. 19. Histogram of the number of velocity components per filament.

The categorization of the velocity components shows that a filament candidate can have several velocity components even in the case of one component being fully correlated. This is shown in Fig. 20. However, a filament candidate with a single component does not necessarily have a fully correlated structure. In general, we find that filament candidates with fewer velocity components are more likely to have a fully correlated component, and candidates with an increasing number of velocity components are more likely to have partially correlated and diffuse components.

Many structures are identified on continuum data that does not provide information about the velocity coherence. Therefore, we test whether there a correlation exists between the intensities of 2D-data and the number of velocity components. With the known multiplicity of the filament candidates, we are able to show that filament candidates with several velocity components tend to be brighter (see Fig. 21). We do so as follows: we derive the mean and maximum intensity of the ATLASGAL dust emission and the ^{13}CO emission integrated over all velocity components. Because the statistical scatter of the intensity values shows a non-Gaussian distribution, we take the median and the 90th percentile value of the intensity distributions of each filament category (i.e. separated according to the number of

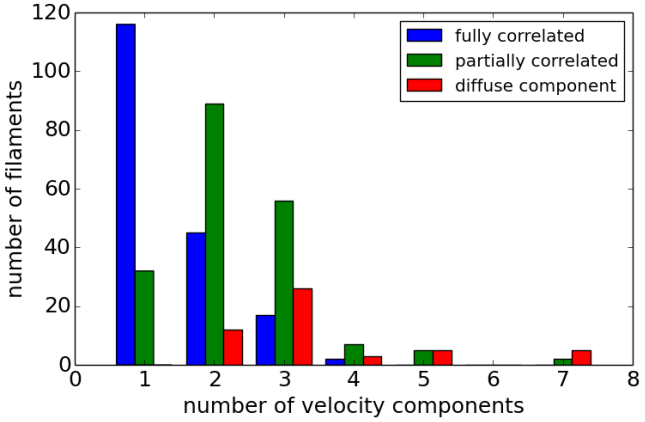

Fig. 20. Histogram of the number of velocity components for fully correlated (blue), partially correlated (green), and diffuse (red) structures.

components) as a qualitative measure. We also estimate the uncertainty of the median using a bootstrapping method. However, only the sample sizes of the filament categories with 1, 2, and 3 components are sufficient to use the bootstrapping method. In this method we draw new, random samples of intensities from among the observed values. We then calculate the median of these new, simulated samples. The resulting distribution of the median values then estimates the sampling function of the observed median and is used to estimate the uncertainty using the standard deviation. We find, that the medians of the ^{13}CO peak intensities increase outside their uncertainties as the number of velocity components increases. The same increase is also seen for the 90th percentile values (Fig. 21). Our data suggests a similar increase for the ATLASGAL peak intensities, but a flat behaviour is also consistent with the data. We could not find such a behaviour for the mean intensities of the filaments (not shown in figures).

For filament candidates with multiple components we investigate whether two physically separate filaments can be located within the same spiral arm. Therefore, we show in Fig. 22 a histogram of the absolute peak-to-peak velocity difference (blue). The bins up to $\delta v = 10$ km s^{-1} are likely to be incomplete because of the component separation limit, as shown before (Fig. 4, Eq. 1). We compare the distribution of the observed velocity differences with model distributions (hatched) of expected velocity difference from a spiral arm. We assume velocity dispersions of $\sigma_{\mathrm{v}_1}(\mathrm{arm}) = 5$ km s^{-1} and $\sigma_{\mathrm{v}_2}(\mathrm{arm}) = 10$ km s^{-1} following Reid et al. (2016) and Caldu-Primo et al. (2013). As we measure the absolute difference between two velocities drawn from a Gaussian distribution, the dispersion of the differences is given by $\sigma_{\delta v} = \sqrt{\sigma_{\mathrm{v}}(\mathrm{arm})^2 + \sigma_{\mathrm{v}}(\mathrm{arm})^2} = \sqrt{2}\sigma_{\mathrm{v}}(\mathrm{arm})$. We sample the difference distributions with 10,000 draws to avoid statistical noise, bin the absolute values of the sample like the observed differences, and scale by 0.016 to get a comparable total number of filaments. We find, that the observed and the model distribution of $\sigma_{\mathrm{v}_2}(\mathrm{arm})$ are similar for $\delta v \leq 30$ km s^{-1}, but we see more observed filaments for larger velocity separations. The model distribution for $\sigma_{\mathrm{v}_1}(\mathrm{arm})$ does not describe the observed one. Therefore, we can conclude that a large fraction of separated filaments might be located in the same spiral arm with a velocity dispersion of $\sigma_{\mathrm{v}_2}(\mathrm{arm})$, but we also see filaments from different Galactic structures along the line-of-sight. However, because of the kinematic distance ambiguity filaments located in different spiral arms can have similar line-of-sight velocities at specific Galactic Longitudes.

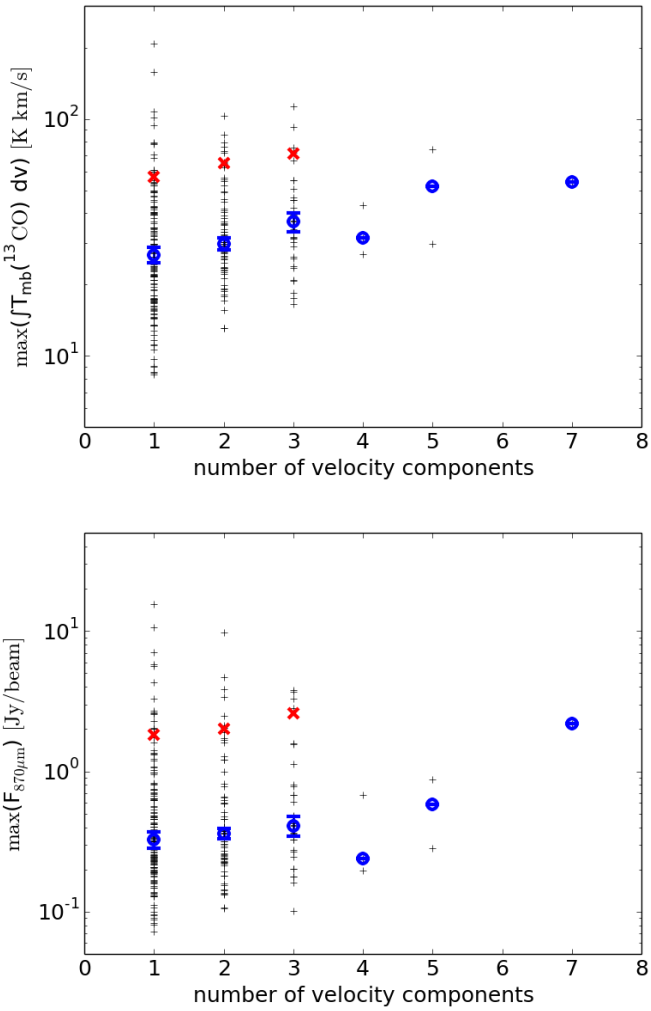

Fig. 21. The peak integrated ^{13}CO intensity (*top*) and the peak ATLASGAL dust intensity (*bottom*) of a filament are plotted against the number of velocity components. The blue circles mark the median, and the red crosses mark the 90th percentile for each number of components. The error-bars show the uncertainty of the median derived by bootstrapping.

4.7. Comparison of masses derived from gas and dust

Calculating the masses of the filaments is an important part of the analysis. However, it comes with some difficulties. Commonly, dust emission or dust extinction is used to calculate the mass of objects. However, because of the line-of-sight projection several filaments that may appear at the same position, and cannot be separated in the continuum data, this is not applicable here. Therefore, we need to use the CO emission to disentangle the projected emission from different structures in velocity space. For the mass estimate we then use the emission integrated over the velocity range of the filament. Specifically, we use the ^{13}CO emission as it has a higher signal-to-noise and traces the lower column

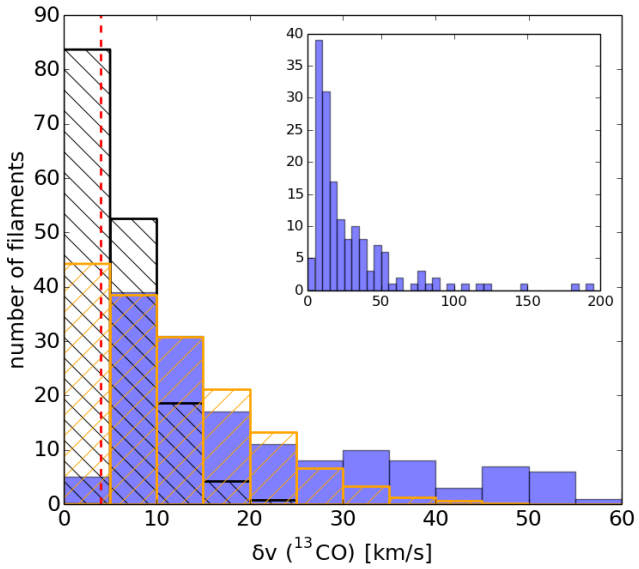

Fig. 22. Histogram of the absolute difference in velocity between the neighbouring velocity components of a filament. The upper right panel shows the complete distribution, while the main panel shows only the lower velocity separations. The black and orange hatched distributions indicate the models for spiral arm velocity dispersions of 5 km s^{-1} and 10 km s^{-1}. The dashed red line indicates the average velocity separation limit of 3.5 km s^{-1} (see Eq. 1 and mean velocity dispersion of 1.17 km s^{-1})

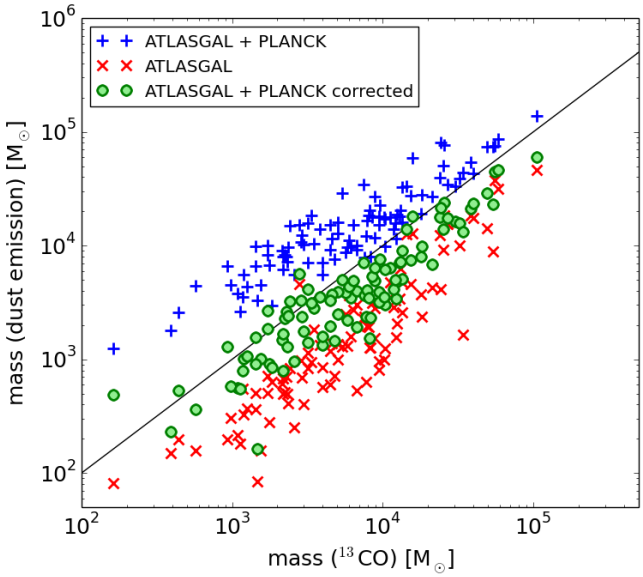

Fig. 23. Mass per fully correlated filament derived from dust versus the mass derived from integrated ^{13}CO using an $X_{^{13}\mathrm{CO}(2-1)}$ factor from Schuller et al. (2017). The black line indicates the one-to-one ratio.

density gas around the skeleton, and calculate the mass like described in Section 3.5.

We first have to test whether this X-factor is a good approximation for the whole survey area. To do so we take a sample of filaments, which show only one velocity component and are fully correlated with the ATLASGAL dust emission. We calculate the masses for this sample using the integrated ^{13}CO emission with Equation 6 and using the ATLASGAL and ATLASGAL+PLANCK dust emission with Equation 7. For all three data-sets we use the same mask around the skeleton. The comparison of the resulting masses is shown in Fig. 23.

We find that masses derived from ^{13}CO are systematically larger than the masses derived from ATLASGAL, but systematically smaller than the masses derived from ATLASGAL+PLANCK. This behaviour is expected as the ATLASGAL maps are sensitive to the small scale (2.5′), high column density dust structures and extended emission from the diffuse surrounding gas is filtered out because of the observing technique (see Schuller et al. (2009)). Therefore, Csengeri et al. (2016) combined the ATLASGAL data with the PLANCK data, which traces the diffuse, large scale structures, but does not resolve the small scales because of the low resolution (4.8′). However, the combined data also traces the dust emission along the line-of-sight, i.e foreground and background. Thus, masses derived from ATLASGAL are likely to be underestimated while masses derived from ATLASGAL+PLANCK are likely to be overestimated.

As shown in Section 3.5, we corrected the ATLASGAL+PLANCK data for the line-of-sight emission towards every filament and used this data to derive another mass estimate. On average we find a mean Galactic emission of 0.52 Jy/beam (beam size of 21″). These corrected dust masses are in agreement with the ^{13}CO derived masses within a factor of 2. Therefore we conclude that the ^{13}CO X-factor derived from the SEDIGISM science demonstration field (Schuller et al. 2017) is a good approximation for the whole survey area.

5. Discussion

5.1. Radial filament profiles

Nearby (< 500 pc), low line-mass (< 100 M$_\odot$ pc^{-1}) filaments have been found to have an FWHM size of the order of 0.1 pc (Arzoumanian et al. 2011). The corrected ATLASGAL+PLANCK and ^{13}CO data trace the wide range of column densities that is needed to study the filament profile. To ensure that we are looking only at true filaments we restrict our sample to the 151 fully correlated filaments with a distance estimate, but for completeness we show the results of the other filaments in Appendix B. However, measuring the filament profile is challenging as most filaments are not homogeneous, linear structures, but show branches and varying central densities.

Therefore, we do not extract the radial column density distribution directly from the data, but estimate the mass of the filaments within filament masks with increasing diameter, s_{box}, using the same equations and assumptions as in Section 3.5. The mass, $M(R)$, is then given by

$$M(R) = 2l \int_0^R \Sigma(r)\, dr \ , \tag{8}$$

where l is the length of the filament, $\Sigma(r)$ is the column density of the gas at distance r from the skeleton (to both sides, with the skeleton at $r = 0$ pc), and $R = 0.5\, s_{\mathrm{box}}$ the maximum radius. We normalize the values with the mass from a box-diameter of $s_{\mathrm{max}} = 4$ pc, where the

typically found radial profile is almost flat (Arzoumanian et al. 2011). The smallest box-diameter is given by the pixel size. The resulting mass curves of the ^{13}CO emission are shown in Fig. 24, and of the continuum emission and less correlated filaments in Appendix B. As the physical resolution is changing with the distance towards the source, we group the filaments in four distance intervals d_i ($d_1 < 2$ kpc $< d_2 < 4$ kpc $< d_3 < 8$ kpc $< d_4$) and average the mass curves within these intervals (see Fig. 26).

The profiles of filamentary structures are found to be well described by a Plummer-like density distribution (Nutter et al. 2008; Arzoumanian et al. 2011; Contreras et al. 2013a), which is given by

$$\rho(r) = \rho_c \left(1 + \left(\frac{r}{R_{\rm flat}}\right)^2\right)^{-p/2} , \quad (9)$$

where ρ_c is the central density of the filament, and $R_{\rm flat}$ the characteristic radius of the flat inner part. The column density profile of the filament (Arzoumanian et al. 2011; Panopoulou et al. 2014) then is described by

$$\Sigma_p(r) = A_p \frac{\rho_c R_{\rm flat}}{[1 + (r/R_{\rm flat})^2]^{\frac{p-1}{2}}} , \quad (10)$$

where $\Sigma = N(\mathrm{H_2})\mu m_p$, μ and m_p as previously defined, and $A_p = (\cos i)^{-1} \int_{-\infty}^{\infty} (1+u^2)^{-p/2} du$, a finite constant for $p > 1$. Other studies (e.g. Arzoumanian et al. 2011) have shown that the inner part of the radial profile of a filament can also be well described by a Gaussian column density distribution. These two models are shown in Fig. 25, where they are normalized to an integrated intensity of 1.

The mass within a box around the theoretical filament is then given by Eq. 8. We plot the measured mass curves as well as the theoretical ones as $M(R)/M(2\ \mathrm{pc})$ and test different values for the exponent, p, and the inner radius, $R_{\rm flat}$, of the Plummer-like distribution and for the dispersion, w, of the Gaussian (see Fig. 26).

A detailed analysis of the density structure of filaments is beyond the scope of this paper. Still, we perform a rough visual comparison between the observed radial column density profiles and modeled ones. We find that the Plummer-like distribution is in agreement with the average profile of the ^{13}CO and dust observations for $p \approx 1.5 \pm 0.5$ and $R_{\rm flat} \approx 0.1$ pc. Also the Gaussian column density distribution with a dispersion of $w = 1$ pc describes the observation within the uncertainties. However, the two fitting models lead to different $FWHMs$ for the filaments. While for a Plummer-like function the $FWHM_P = (2^{2/(p-1)} - 1)^{1/2} R_{\rm flat}$ ($FWHM_{2.0} \approx 0.17$ pc, $FWHM_{1.5} \approx 0.39$ pc (Heitsch 2013b), for the Gaussian $FWHM_G = \sqrt{8 \ln 2}\, w \approx 2.36$ pc.

One possible interpretation is that the Gaussian traces only the low column density surrounding of the filament, but not the dense inner part, hence the actual filament. From previous studies (see Arzoumanian et al. 2011; Panopoulou et al. 2014) and the Plummer-like function we see measurements of the FWHM between 0.1 pc and 0.6 pc. The physical beam size of the SEDIGISM data at a distance of 2 kpc is about 0.3 pc and therefore, we are at the resolution limit for the dense filament spine, but note that the mass curves (integral over the radial profile) have a dependency on $R_{\rm flat}$ in the Plummer-like case. However, we find that small changes of $R_{\rm flat}$ do not significantly change the agreement with the observation. Therefore, we conclude that the mass of the filament is dominated by the low column density gas surrounding the spine, and that the resolution of the SEDIGISM data is not sufficient to meaningfully fit the inner spine with a Gaussian radial profile.

The exponent of the average density profile is $p \approx 1.5$, which is in agreement with the lower limit found by Arzoumanian et al. (2011). The single profiles scatter between $p \approx 1.0$ and $p \approx 2.0$, with the scatter decreasing with more distant filaments most likely because of the smaller sample. Also, we tested the effect of the beam size to the theoretical radial profiles by convolving the profile with a Gaussian beam. The resulting theoretical mass curves are shallower with increasing distance, but not significantly, given the scatter of the single observed mass curves. The study of Arzoumanian et al. (2011) analyses prominent filaments in nearby molecular clouds using dust continuum emission. This selection of prominent filaments might give a bias towards higher exponents. Theoretically, an isolated, isothermal, cylindrical filament in hydrostatic equilibrium would be expected to have an exponent of $p = 4$ (Ostriker 1964). However, this exponent is typically not found in observations and models (Juvela et al. 2012; Kainulainen et al. 2015). Low resolution and signal-to-noise data explain only partially the observed exponents. Therefore, observations suggest that filaments are embedded in a surrounding molecular cloud (Fischera & Martin 2012), not isothermal (Recchi et al. 2013) and/or not in hydrostatic equilibrium (Heitsch 2013a,b).

It is important to mention that for an exponent of $p < 2$ mathematically the mass diverges with an increasing radius. This can be seen in Fig. 25. As a result the mass, M, and therefore, also the line-mass (mass per unit length), $m = M/l$, are not well-defined. However, filaments are not isolated structures, but surrounded by low density gas, which sets boundary conditions that are not considered in this model. As mentioned before, we decided to use a radius dependent on the velocity dispersion of the filament to estimate the mass of the filaments in this study.

5.2. Stability against Collapse

Thermally supercritical filaments are commonly seen as star formation sites. Therefore, they need to build the connection between the diffuse gas of the molecular cloud and the dense gas in the star-forming cores. Inutsuka & Miyama (1992) showed that isothermal, infinitely long, self-gravitating cylinders will collapse radially if their line-mass (mass per unit length) exceed a critical value, and fragment along the axis in the sub-critical and equilibrium case. The critical line-mass is given by

$$m_{\rm crit,th} = \frac{2c_s^2}{G} \quad (11)$$

(Ostriker 1964), where G is the gravitational constant and c_s is the sound speed of the medium, which is dependent on the gas temperature T (Eq. 5). Assuming a typical gas temperature of $T = 15$ K the critical line-mass is $m_{\rm crit} = 20\ \mathrm{M_\odot\,pc^{-1}}$.

Based on our observations and analysis we can estimate the line-mass for all the filaments with a distance estimate by $m_{\rm obs} = M/l$, where M is the mass estimated from the

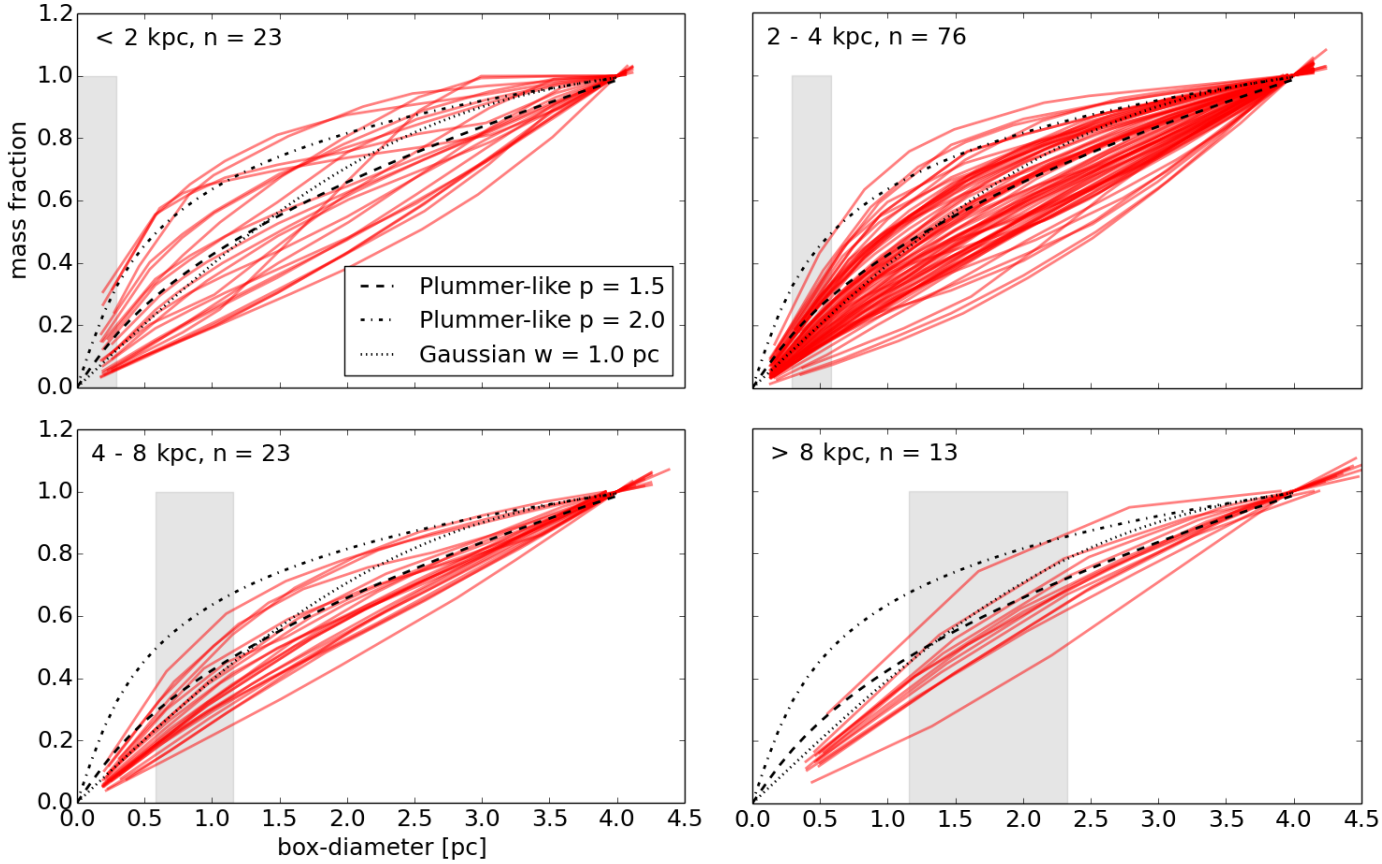

Fig. 24. Fraction of the filament mass derived from ^{13}CO emission dependent on the box-diameter of the mask separated by distances. *Top left:* $d < 2$ kpc, *Top right:* 2 kpc $< d < 4$ kpc, *Bottom left:* 4 kpc $< d < 8$ kpc, *Bottom right:* $d > 8$ kpc. One curve describes one fully correlated filament at its distance estimate. The grey lines indicate the physical beamsize at distances of 2 kpc, 3 kpc, 6 kpc, and 8 kpc. The black lines show the integrated theoretical radial profiles, which describe a Plummer-like distribution $p = 1.5$ (dashed) or $p = 2.0$ (dash-dotted), and a Gaussian distribution with a dispersion of $w = 1.0$ (dotted).

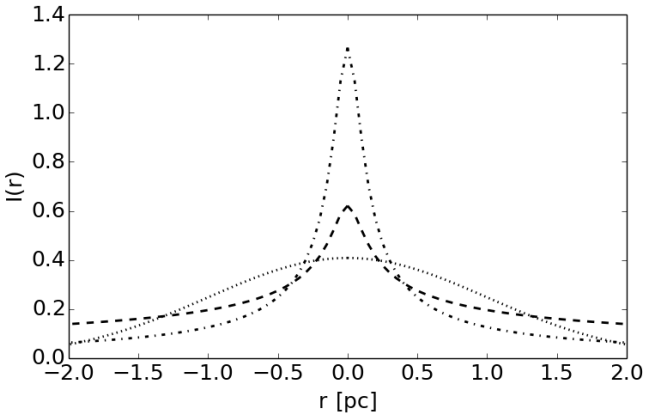

Fig. 25. Theoretical filament profiles normalized to an integrated intensity of 1, which describe a Plummer-like function with $R_{\rm flat} = 0.1$ pc and $p = 1.5$ (dashed) or $p = 2.0$ (dash-dotted), and a Gaussian with a dispersion of $w = 1.0$ pc (dotted). The radial integration of these profiles is shown in Figs. 24 and 26.

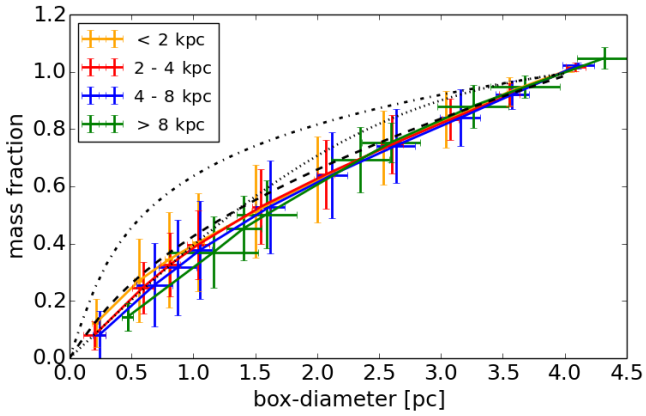

Fig. 26. Average fraction of the filament mass derived from ^{13}CO emission dependent on the box-diameter of the mask. The color indicates the distance of the filament with d_1 orange, d_2 red, d_3 blue, and d_4 green. The errorbars indicate the dispersion of the measured mass fraction and box-diameter. The black lines are same as Fig. 24.

^{13}CO emission, and l is the length along the velocity coherent skeleton. Because of the separation of the velocity components this length does no longer securely describe the linear shape (with small branches) of the original filament candidate sample, especially for the not fully correlated filaments. Therefore, we concentrate this discussion on the fully correlated filaments, but also perform the calculations for the others.

The line-masses we observe with our resolution are significantly above the critical thermal value (see Fig. 27).

This leaves us with two possible conclusions: either the filaments are collapsing radially or they have a supporting mechanism additional to the thermal pressure. Moreover, we find that the linewidth of the molecular gas is significantly larger than the sound speed, $c_s = 0.21$ km s^{-1}. This increased linewidth can support both theories, as it can be interpreted as either structured motions, like collapse, or turbulent motions within the gas.

Assuming that non-thermal motions contribute to the supporting mechanism, equation 11 can be modified to

$$m_{\rm crit,tot} = \frac{2(c_s^2 + \sigma_{\rm nt}^2)}{G} \quad (12)$$

(Fiege & Pudritz 2000), where $\sigma_{\rm nt}$ is the non-thermal velocity dispersion of the filament, and $m_{\rm crit,tot}$ is the critical, total (thermal and non-thermal) line-mass. After determining the velocity dispersion for all filaments, we can calculate the critical non-thermal line-mass and compare it with the observed one (Fig. 27).

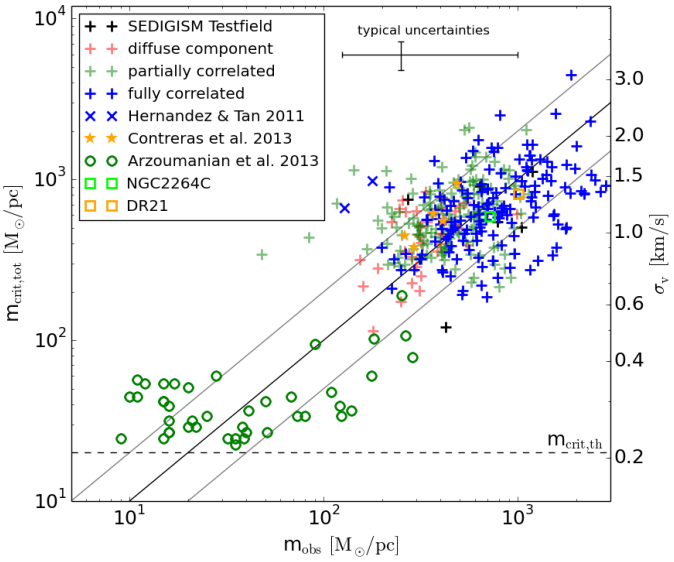

Fig. 27. Critical, non-thermal line-mass derived from the velocity dispersion versus observed line-mass using integrated ^{13}CO. The fully correlated filaments are indicated in blue, and the other filaments of this study in a shaded green and red. The black solid line shows the one-to-one correlation, the grey lines indicate a factor 2 uncertainty, and the dashed line shows the critical thermal line-mass.

The uncertainty of the critical line-mass is given by the observed velocity dispersion and therefore depends on the velocity resolution and the quality of the signal. The main contributions for the uncertainties of the mass estimates are the X-factor (factor of 0.5–2), optically thick ^{13}CO emission (factor of 1–2), and the distance. As the length is also dependent on the distance estimate, the line-mass is only linearly dependent on the distance, which adds another factor of 0.8–1.2 to the uncertainty. Additionally, the length is measured as projection on the sky and therefore, the observed line-mass is an upper limit considering possible inclinations. The typical uncertainty is given by the black cross in Fig. 27. Additionally, it needs to be mentioned that based on the resolution of our data we are only able to derive global parameters. Higher resolution data (spatial and kinematic) could reveal substructures, which might lead to different results.

We find that the critical, non-thermal line-mass is, within the uncertainties, in agreement with the observed line-mass. Therefore, Eq. 12 seems to describe a common relation between the observed linewidth and line-mass in the form $m \propto (c_s^2 + \sigma_{\rm nt}^2)$. The sound speed, c_s, depends only on the temperature of the ISM, which can be assumed to be about constant. Hence, the line-mass is proportional to the non-thermal motion. We also find that partially correlated filaments and diffuse components follow the same relation as the fully correlated filaments, but with a slightly wider spread.

We now want to investigate where this relation comes from. As we discussed before, one explanation might be infall motion. Inutsuka & Miyama (1992) showed that infinitely long, isothermal filaments with a line-mass above the critical value collapse radially. Heitsch et al. (2009) and Heitsch (2013b) determined the accretion velocity profile, $v(R)$, for gas in a steady-state free-fall onto the filament axis as

$$v(R) = 2\left(Gm \ln \frac{R_{\rm ref}}{R}\right)^{1/2}, \quad (13)$$

where G is the gravitational constant, m is the line-mass of the filament, $R_{\rm ref}$ is the limiting, outer radius of the filament, and R is the radial position of the gas.

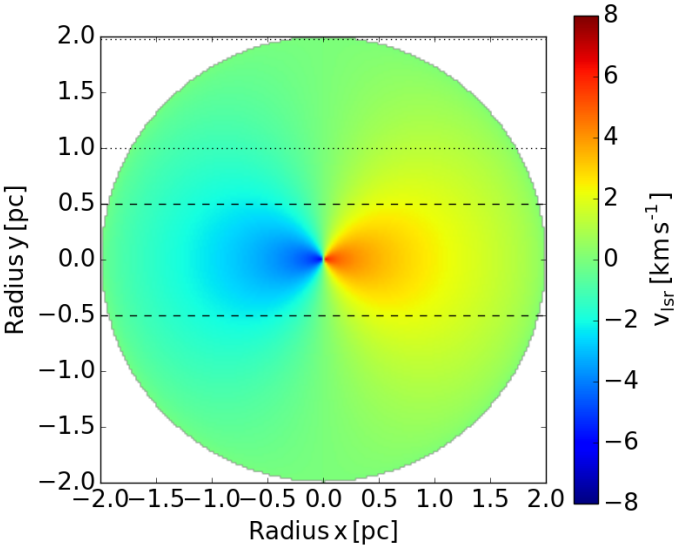

Fig. 28. Line-of-sight velocity distribution across a slice of a filament base on Eq. 13 using a line-mass of $m = 500$ M$_\odot$ pc^{-1} and $R_{\rm ref} = 2.0$ pc. The observer is located on the right side, observing the whole slice, the inner part (dashed lines), and outer part (dotted lines), which where analysed separately.

We use this radial velocity distribution, $v(R)$, to estimate the signal which would be observed from a collapsing filament, similar to Heitsch (2013a). First, we derive the line-of-sight velocities, v_{lsr}, across the filament for an observer looking edge on (see Fig. 28),

$$v_{lsr} = v(R) \cdot \frac{x}{R}, \quad (14)$$

where R is the radial distance to the center, and x is the position in the x-axis direction of the Cartesian coordinate system. Second, we draw for each position in the filament 50 values from a Gaussian distribution centered on the derived velocities with a thermal velocity dispersion of $c_s = 0.21$ km s^{-1}. Third, we plot a weighted histogram of the velocities with bins identical to the SEDIGISM channel width of 0.25 km s^{-1}, where we use the density at the position of the filament as weight. The density is given by a Plummer-like distribution (see Section 5.1). From the weighted histogram we calculate the standard deviation, hence the theoretically observed velocity dispersion.

Within this template we vary the line-mass, m, the exponent of the density profile, p, and the area of the filament we observe (complete, middle, edge) to study their effect on theoretical signal. We choose the outer radius $R_{\rm ref} = 2.0$ pc and the characteristic radius of the density distribution $R_0 = 0.1$ pc, see Section 5.1. The results are shown in Table 4 and Fig. 29.

Table 4. The three input parameters, the resulting velocity dispersion $\sigma_{\rm v}$, derived from the modelled collapse spectra, and the expected total velocity dispersion, following the found relation with m.

Fig. 29	m M$_\odot$ pc^{-1}	p	area	$\sigma_{\rm v}$ km s^{-1}	$\sigma_{\rm crit,nt}$ km s^{-1}
a	100	1.5	all	1.03	0.46
b	500	1.5	all	2.29	1.04
c	1000	1.5	all	3.23	1.47
d	500	2.0	all	2.65	1.04
e	500	3.0	all	3.24	1.04
f	500	1.5	middle	2.86	-
g	500	1.5	edge	0.62	-

We find that the infall motions indeed show the observed relation between line-mass and velocity dispersion, $m \propto \sigma_{\rm v}^2$ (Table 4, models a, b, c). However, the theoretical velocity dispersion is higher by a factor of 2 than the observed values. Additionally, we did not take turbulent motions into account, which would be caused by the infall (Heitsch 2013b), and give a wider theoretical signal. To fit the observations, the collapse needs to be slowed down, which can be caused by the turbulence created by the collapse. Finding a combination of collapse and turbulent motions that would reproduce the observed kinematics is beyond the scope of this study.

Another way to identify ongoing collapse could be an analysis of the shape of the emission lines (Schneider et al. 2010). The theoretical line profiles show double-peaked shapes towards the centre of the filament and for filaments with a steep density profile. However, a comparison of the theoretical line shapes with the observed ones is difficult as several other effects can alter the shape, like spatially unresolved motions of the filament within the beam, or self-absorption, also see Heitsch (2013a) for different inclination angles. In a few filaments we find some evidence for a double-peaked velocity profile (see Section 3.2). But a more detailed analysis of, preferably, geometrically simple filaments with higher spatial and kinematic resolution would be necessary to address the effects of complex kinematics.

Rapid radial collapse would lead to extremely narrow filaments, which rarely have been observed up to now (e.g. Stutz & Gould 2016). However, Heitsch (2013b) shows that the fragmentation timescales are shorter than the collapse timescales, which is supported by the fact that fragmentation is seen in almost all filaments (Jackson et al. 2010; Kainulainen et al. 2013; Takahashi et al. 2013; Wang et al. 2014; Beuther et al. 2015; Teixeira et al. 2016; Kainulainen et al. 2017). Our finding of slowed collapse would increase the difference between the timescales, which is still in agreement with the observations. Also, simulations of filament evolution by Chira et al. (2018) show a start of fragmentation before the filaments reach the critical mass for gravitational collapse.

However, we also cannot rule out the possibility that the observed velocity dispersion is mainly created by turbulent motions. These turbulent motions are discussed to increase the internal pressure and support the filament against gravitational collapse. Therefore, this theory is also in agreement with the observations.

6. Conclusions

In this study we studied spectral line emission from 283 filament candidates detected with ATLASGAL continuum dust emission from the catalogue of Li et al. (2016) in the SEDIGISM ^{13}CO and C^{18}O survey. As these candidates can be the result of line-of-sight projection of multiple structures, we tested the candidates for coherence in velocity space and derived the mass, size, and a collection of kinematic properties. To do so we developed an automated analysis tool that finds the different velocity components of a candidate, if existing, separates them and checks for correlation with the original ATLASGAL emission. We found 422 velocity-coherent filaments that correlate completely or partially with the original candidate. For these filaments we find the following:

- Two-thirds of the filament candidates are single velocity-coherent structures. The other candidates are line-of-sight projections of mainly two and three velocity components, and up to one candidate with seven velocity components. Also, we found a possible indication for a correlation between the maximum intensity within the filament candidate and the number of velocity components for the integrated ^{13}CO and ATLASGAL dust emission, but a flat behaviour is within the uncertainties.
- Comparing the kinematics of the filaments seen in ^{13}CO and C^{18}O , we could show that both isotopologues trace the same gas. Differences found in the comparison could be identified as biases arising from low signal-to-noise C^{18}O data.
- The filament profiles are on average in agreement with a Plummer-like density distribution with an exponent of $p \approx 1.5 \pm 0.5$. The inner radius cannot be constrained exactly because of the limited resolution of the data. This low exponent indicates that filaments are typically located within larger molecular clouds, and therefore, the outer radius of a filament cannot be well defined. For the mass estimates we chose a radius which includes the gas that can take part in star formation within the next 2 Myr.
- The observed line-mass of the filaments is in agreement with the critical non-thermal line-mass and significantly higher than the critical thermal line-mass. However, we do not know the source of the observed velocity dispersion. Comparing the relation we find between velocity

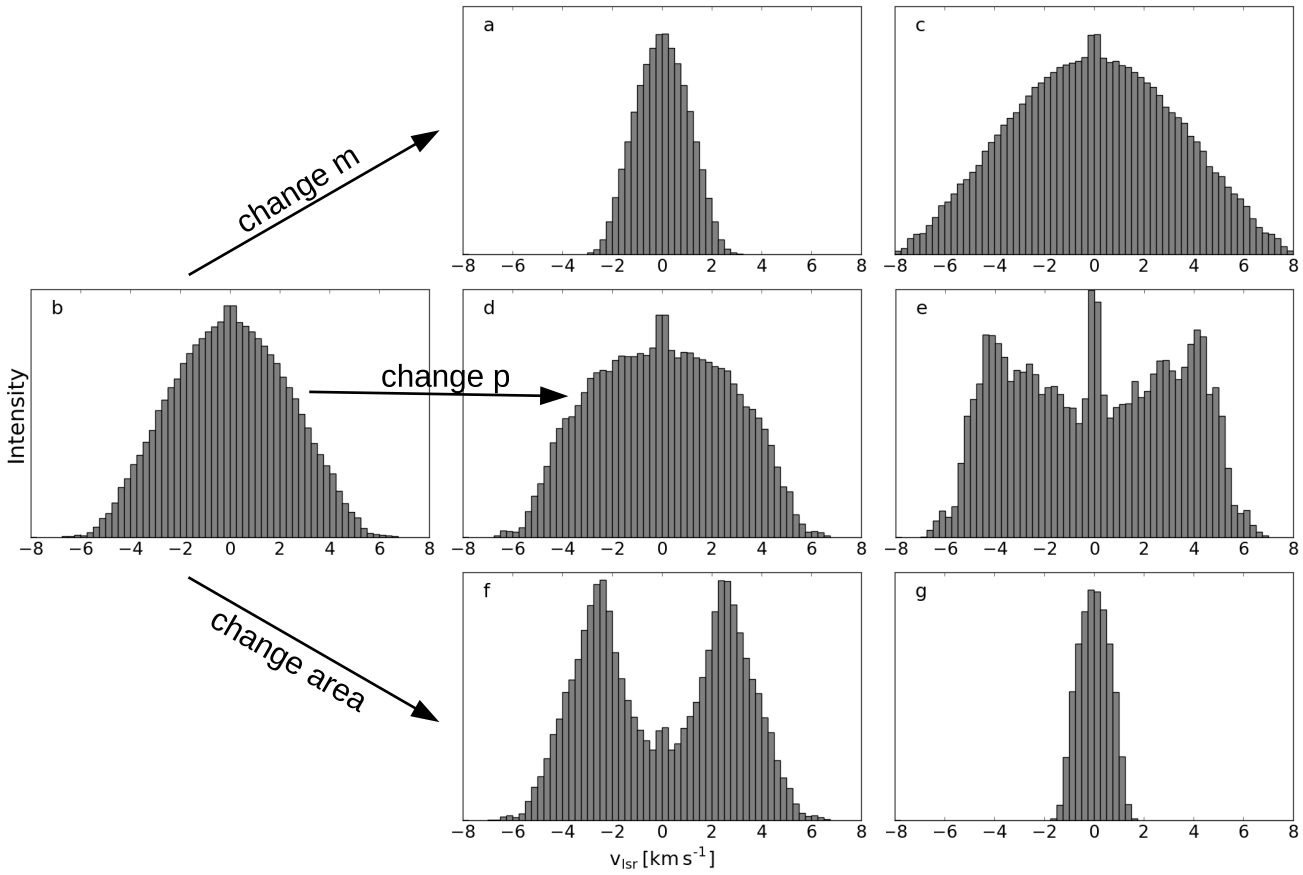

Fig. 29. Theoretical molecular line profiles with varying parameters, see Table 4.

dispersion and line-mass with the theoretical infall velocity profile based on Heitsch (2013b) generally does not reveal evidence for free-fall collapse. However, radial infall of the gas onto the skeleton can possibly explain the relation.

In this study we analysed the kinematics of 283 filament candidates, finding 180 reliable velocity coherent filaments, 151 with distance estimates between 1 kpc and 13 kpc, and 242 other velocity coherent filamentary structures in the line-of-sight of the candidates, leading to the largest statistics of filament parameters so far. However, due to the spatial resolution of 30″ and velocity resolution of 0.25 km s^{-1}, the derived parameters generally only describe global behaviour of the filaments. As the evolution and fragmentation of filaments is a hierarchical process it will be necessary to also study the smaller scales. High resolution observations to recover the small scales (< 0.1 pc) are essential, and this study can be the starting point for the selection of a representative sample for such higher resolution follow-ups.

Acknowledgments

We want to thank the anonymous referee for constructive and very detailed comments. Also, we thank Guang-Xing Li for supporting this study by offering additional data and information on the filament candidates. Also, we thank Prof. Kostas Tassis, Dr. Dario Colombo, Carsten König, and the rest of the SEDIGISM consortium for support and productive discussions.

M.M. is supported for this research through a stipend from the International Max Planck Research School (IMPRS) for Astronomy and Astrophysics at the Universities of Bonn and Cologne. T.Cs. acknowledges support from the *Deutsche Forschungsgemeinschaft, DFG* via the SPP (priority programme) 1573 'Physics of the ISM'. H.B. acknowledges support from the European Research Council under the Horizon 2020 Framework Program via the ERC Consolidator Grant CSF-648505. L.B. acknowledges support by CONICYT project PFB-06. This work of J.K. has received funding from the European Union's Horizon 2020 research and innovation program under grant agreement No 639459 (PROMISE).

References

Abreu-Vicente, J., Ragan, S., Kainulainen, J., et al. 2016, A&A, 590, A131
André, P., Men'shchikov, A., Bontemps, S., et al. 2010, A&A, 518, L102
Arzoumanian, D., André, P., Didelon, P., et al. 2011, A&A, 529, L6
Arzoumanian, D., André, P., Peretto, N., & Könyves, V. 2013, A&A, 553, A119
Bally, J., Stark, A. A., Wilson, R. W., et al. 1987, ApJ, 312, L45
Beuther, H., Ragan, S. E., Johnston, K., et al. 2015, A&A, 584, A67
Beuther, H., Tackenberg, J., Linz, H., et al. 2012, ApJ, 747, 43
Caldu-Primo, A., Schruba, A., Walter, F., et al. 2013, AJ, 146, 150
Chira, R. A., Kainulainen, J., Ibàñez-Mejía, J. C., Henning, T., & Mac Low, M. M. 2018, A&A, 610, A62
Contreras, Y., Rathborne, J., & Garay, G. 2013a, MNRAS, 433, 251
Contreras, Y., Schuller, F., Urquhart, J. S., et al. 2013b, A&A, 549, A45
Csengeri, T., Urquhart, J. S., Schuller, F., et al. 2014, A&A, 565, A75
Csengeri, T., Weiss, A., Wyrowski, F., et al. 2016, A&A, 585, A104

Evans II, N. J., Dunham, M. M., Jørgensen, J. K., et al. 2009, ApJ, 181, 321
Federrath, C. 2016, MNRAS, 457, 375
Fiege, J. D. & Pudritz, R. E. 2000, MNRAS, 311, 85
Fischera, J. & Martin, P. G. 2012, A&A, 542, A77
Gonzalez, R. C. & Woods, R. E. 1992, Reading, MA Addison-Wesley, 1992
Güsten, R., Nyman, L. A., Schilke, P., et al. 2006, A&A, 454, L13
Hacar, A., Kainulainen, J., Tafalla, M., Beuther, H., & Alves, J. 2016, A&A, 587, A97
Hacar, A., Tafalla, M., Forbrich, J., et al. 2018, A&A, 610, A77
Hacar, A., Tafalla, M., Kauffmann, J., & Kovács, A. 2013, A&A, 554, A55
Heitsch, F. 2013a, ApJ, 769, 115
Heitsch, F. 2013b, ApJ, 776, 62
Heitsch, F., Ballesteros-Paredes, J., & Hartmann, L. 2009, ApJ, 704, 1735
Henshaw, J. D., Caselli, P., Fontani, F., Jimenez-Serra, I., & Tan, J. C. 2014, MNRAS, 440, 2860
Hernandez, A. K., Tan, J. C., Kainulainen, J., et al. 2012, ApJ, 756, L13
Hill, T., Motte, F., Didelon, P., et al. 2011, A&A, 533, A94
Inutsuka, S. & Miyama, S. M. 1992, ApJ, 338, 392
Jackson, J., Finn, S., Chambers, E., Rathborne, J., & Simon, R. 2010, ApJ, 719, L185
Johnstone, D., Jason, D. F., Redman, R. O., et al. 2003, ApJ, 588, L37
Juvela, M., Malinen, J., & Lunttila, T. 2012, A&A, 544, 11 pp
Kainulainen, J., Hacar, A., Alves, J., et al. 2015, A&A, 586, A27
Kainulainen, J., Ragan, S. E., Henning, T., & Stutz, A. 2013, A&A, 557, A120
Kainulainen, J., Stutz, A. M., Stanke, T., et al. 2017, A&A, 600, A141
Kainulainen, J., Stutz, A. M., Stanke, T., et al. 2017, A&A, 600, A141
Kauffmann, J., Bertoldi, F., Bourke, T. L., Evans, N. J., & Lee, C. W. 2008, A&A, 487, 993
Kirk, H., Myers, P. C., Bourke, T. L., et al. 2013, ApJ, 766, 115
Koch, E. W. & Rosolowsky, E. W. 2015, MNRAS, 452, 3435
Lamarre, J.-M., Puget, J.-L., Ade, P. A. R., et al. 2010, A&A, 520, A9
Li, G.-X., Urquhart, J. S., Leurini, S., et al. 2016, A&A, 591, A5
Mattern, M., Kainulainen, J., Zhang, M., & Beuther, H. 2018, eprint arXiv:1804.02256 [arXiv:1804.02256]
Miettinen, O. 2012, A&A, 545, A3
Molinari, S., Bally, J., Barlow, M., et al. 2010, PASP, 122, 314
Nutter, D., Kirk, J. M., Stamatellos, D., & Ward-Thompson, D. 2008, MNRAS, 384, 755
Ossenkopf, V. & Henning, T. 1994, A&A, 291, 943
Ostriker, J. 1964, ApJ, 140, 1056
Padoan, P., Juvela, M., Goodman, A., & Nordlund, Å. 2001, ApJ, 553, 227
Palmeirim, P., André, P., Kirk, J., et al. 2013, A&A, 550, A38
Panopoulou, G. V., Tassis, K., Goldsmith, P. F., & Heyer, M. H. 2014, MNRAS, 444, 2507
Peretto, N., Fuller, G. A., André, P., et al. 2014, A&A, 561, A83
Peretto, N., Fuller, G. a., Duarte-Cabral, A., et al. 2013, A&A, 555, A112
Pillai, T., Wyrowski, F., Carey, S. J., & Menten, K. M. 2006a, A&A, 450, 569
Pillai, T., Wyrowski, F., Menten, K. M., & Krügel, E. 2006b, A&A, 447, 929
Planck Collaboration, P., Ade, P. A. R., Aghanim, N., et al. 2014, A&A, 571, A1
Ragan, S. E., Henning, T., Tackenberg, J., et al. 2014, A&A, 568, A73
Recchi, S., Hacar, A., & Palestini, A. 2013, A&A, 558, A27
Reid, M. J., Dame, T. M., Menten, K. M., & Brunthaler, A. 2016, ApJ, 823, 77
Schisano, E., Rygl, K. L. J., Molinari, S., et al. 2014, ApJ, 791, 27
Schneider, N., Csengeri, T., Bontemps, S., et al. 2010, A&A, 520, A49
Schneider, S. & Elmegreen, B. G. 1979, ApJ, 41, 87
Schuller, F., Csengeri, T., Urquhart, J. S., et al. 2017, A&A, 601, A124
Schuller, F., Menten, K. M., Contreras, Y., et al. 2009, A&A, 504, 415
Smith, R. J., Glover, S. C. O., Klessen, R. S., et al. 2015, MNRAS, 455, 3640
Sousbie, T. 2011, MNRAS, 414, 350
Stutz, A. M. & Gould, A. 2016, A&A, 590, A2
Takahashi, S., Ho, P. T. P., Teixeira, P. S., Zapata, L. A., & Su, Y.-N. 2013, ApJ, 763, 57
Teixeira, P. S., Takahashi, S., Zapata, L. A., Ho, P. T. P., & Ho, P. T. P. 2016, A&A, 587, A47
Urquhart, J. S., Csengeri, T., Wyrowski, F., et al. 2014, A&A, 568, A41
Urquhart, J. S., König, C., Giannetti, A., et al. 2018, MNRAS, 473, 1059
Vassilev, V., Meledin, D., Lapkin, I., et al. 2008, A&A, 490, 1157
Wang, K., Testi, L., Burkert, A., et al. 2016, ApJS, 226, 9
Wang, K., Testi, L., Ginsburg, A., et al. 2015, MNRAS, 450, 4043
Wang, K., Zhang, Q., Testi, L., et al. 2014, MNRAS, 439, 3275
Wang, K., Zhang, Q., Wu, Y., Li, H. B., & Zhang, H. 2012, ApJ, 745
Zucker, C., Battersby, C., & Goodman, A. 2015, ApJ, 815, 23
Zucker, C., Battersby, C., & Goodman, A. 2017, ArXiv e-prints [arXiv:1712.09655]

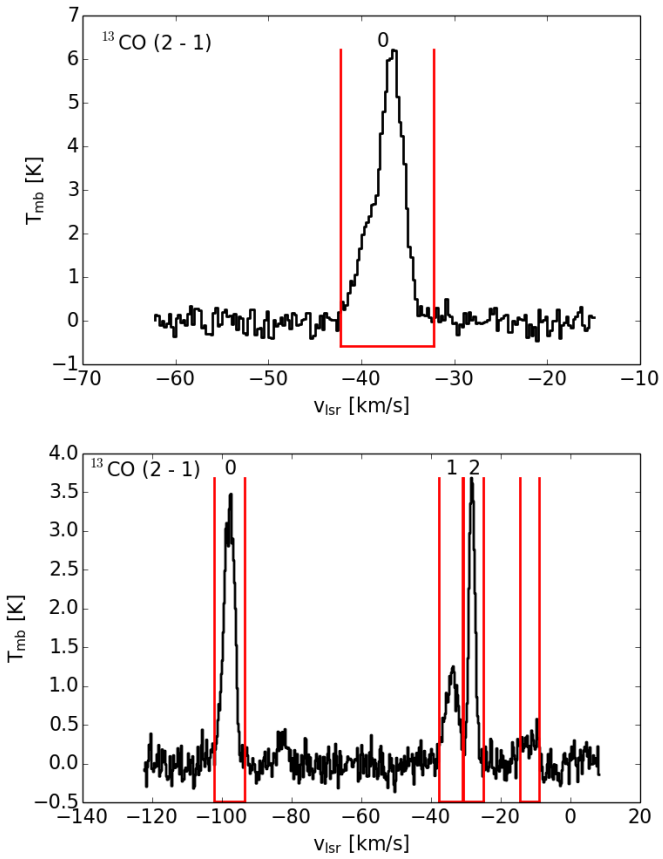

Fig. A.1. Average ^{13}CO spectrum over the skeleton of filament candidate "G339.116-00.405" (top) and "G346.293+00.109" (bottom). The red lines mark the identified emission intervals named by letters.

Appendix A: gas dust correlation examples

In section 3.3 we are describing the method of comparing the ATLASGAL dust intensities with the integrated ^{13}CO intensity maps to identify the spatially correlated velocity components. Based on this correlation we assign one of four categories to the structure, which are: uncorrelated, completely correlated, partially correlated, and diffuse component. To visualize this categorization we show one example in the section 3.3 (Figs. 6, 7). To give a complete picture we present here the correlation plots of the other components of the filament candidate "G333.297+00.073" (Fig. A.2, for intensity maps see Fig. 6), and ^{13}CO spectra (Fig. A.1), integrated intensity maps and the corresponding correlation plots for the filament candidates "G339.116-00.405" (Fig. A.3) and "G346.293+00.109" (Figs. A.4 and A.5).

Appendix B: Filament profiles

In Section 5.1 we showed how the gas mass of correlated filaments is increasing with increasing radius. To be complete, we also show the mass curves of the correlated filaments based on the corrected ATLASGAL+PLANCK data (Fig. B.1), and the mass curves of the partially correlated (blue, Fig. B.2) and diffuse component filaments (red, Fig. B.2) based on the integrated ^{13}CO observations.

The mass curves of of the correlated filaments are in mostly in agreement with ^{13}CO observations. However, for the most nearby filaments (< 2 kpc), and especially in the continuum data, we find profiles indicating a slope of $p < 0$. This can be explained by line-of-sight confusion within the large boxes around the filament skeleton. As the dust continuum data traces all emission along the line-of-site it is possible that strong emission, which is not related to the filament but located nearby, is taken into account for the mass estimate for larger radii. Therefore, the masses will be overestimated. This effect is more likely for nearby filaments, as larger angular sizes are taken into account for the same physical size. The gas mass curves of the partially correlated and diffuse component filaments show on average similar results as the correlated filaments, but with a larger scatter, as the skeleton no longer necessarily represents the shape of the structure.

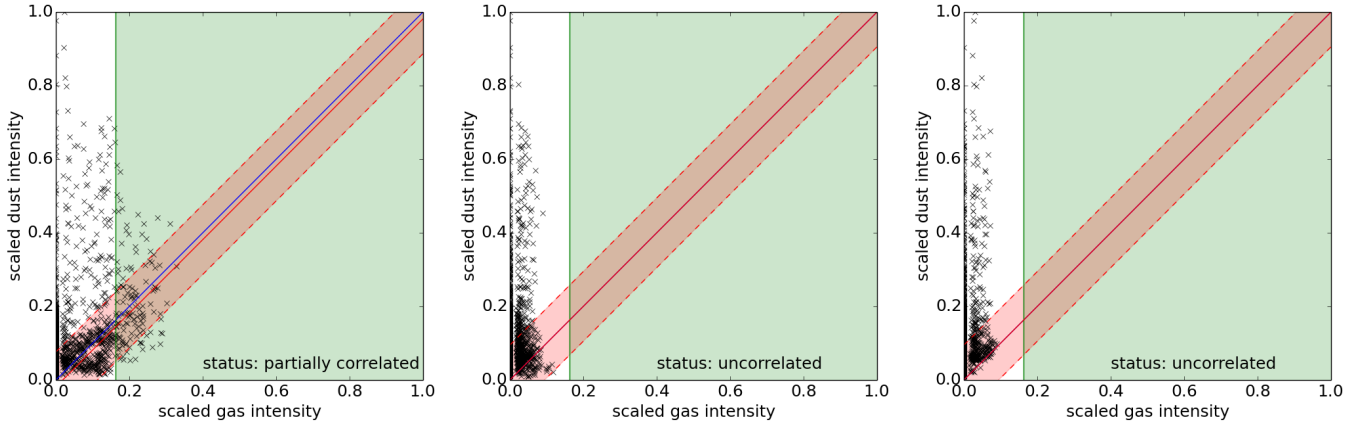

Fig. A.2. Gas-dust correlation plots of the velocity components "b","c", and "d" of the filament candidate G333.297+00.073 (see Figs. 3, 5, and 6). The blue line gives the one-to-one correlation. The green area indicates values above the $\sigma_{\rm gas}$ limit. The red line shows the fitting result, and the area within the dashed red lines marks the $\pm\sigma_{\rm cor}$ surrounding. $p_{\rm cor,\ gas}$ is estimated from the overlap of these areas.

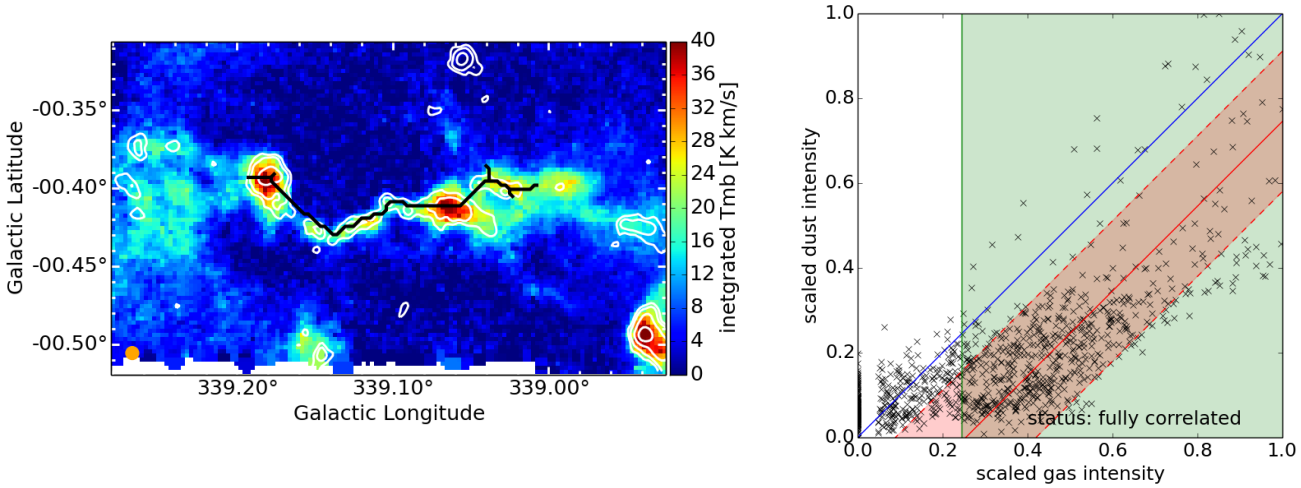

Fig. A.3. Integrated ^{13}CO intensity map (left) and gas-dust correlation plot (right, description as in Fig. A.2) of the single velocity component filament candidate "G339.116-00.405". Because of the good correlation between the only identified velocity component with the ATLASGAL emission, it was categorized as fully correlated filament and can be found as "G339.116-00.405_0" in the final catalogue.

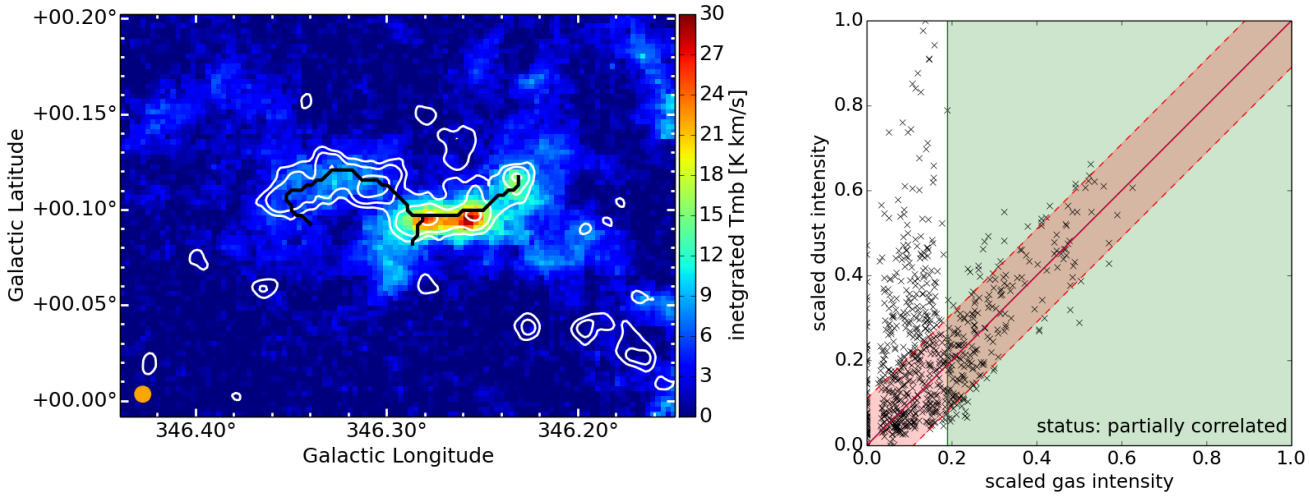

Fig. A.4. Integrated ^{13}CO intensity map left) and gas-dust correlation plot (right, description as in Fig. A.2)) of the first velocity component of the filament candidate "G346.293+00.109". The partially correlated filament is listed as "G346.293+00.109_0". The other three velocity components of the candidate are shown in Fig. A.5.

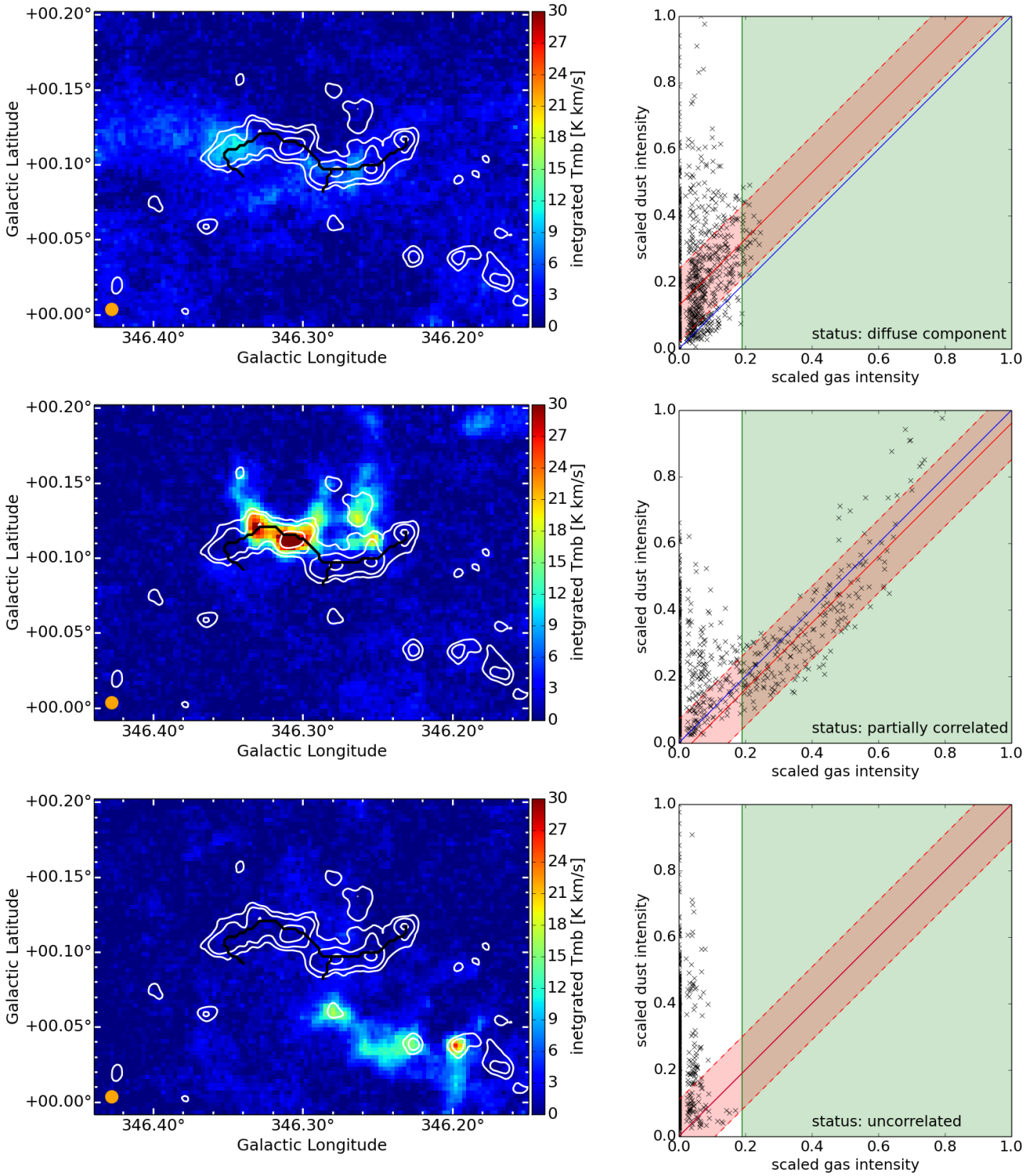

Fig. A.5. Integrated ^{13}CO intensity maps (left) and gas-dust correlation plots (right, description as in Fig. A.2)) of the second (top), third (middle), and fourth (bottom) velocity component of the filament candidate "G346.293+00.109". The second, diffuse component is listed as "G346.293+00.109_1" and the third, partially correlated component is listed as "G346.293+00.109_2". The uncorrelated component is not listed in the catalogue. The first velocity components of the candidate is shown in Fig. A.4.

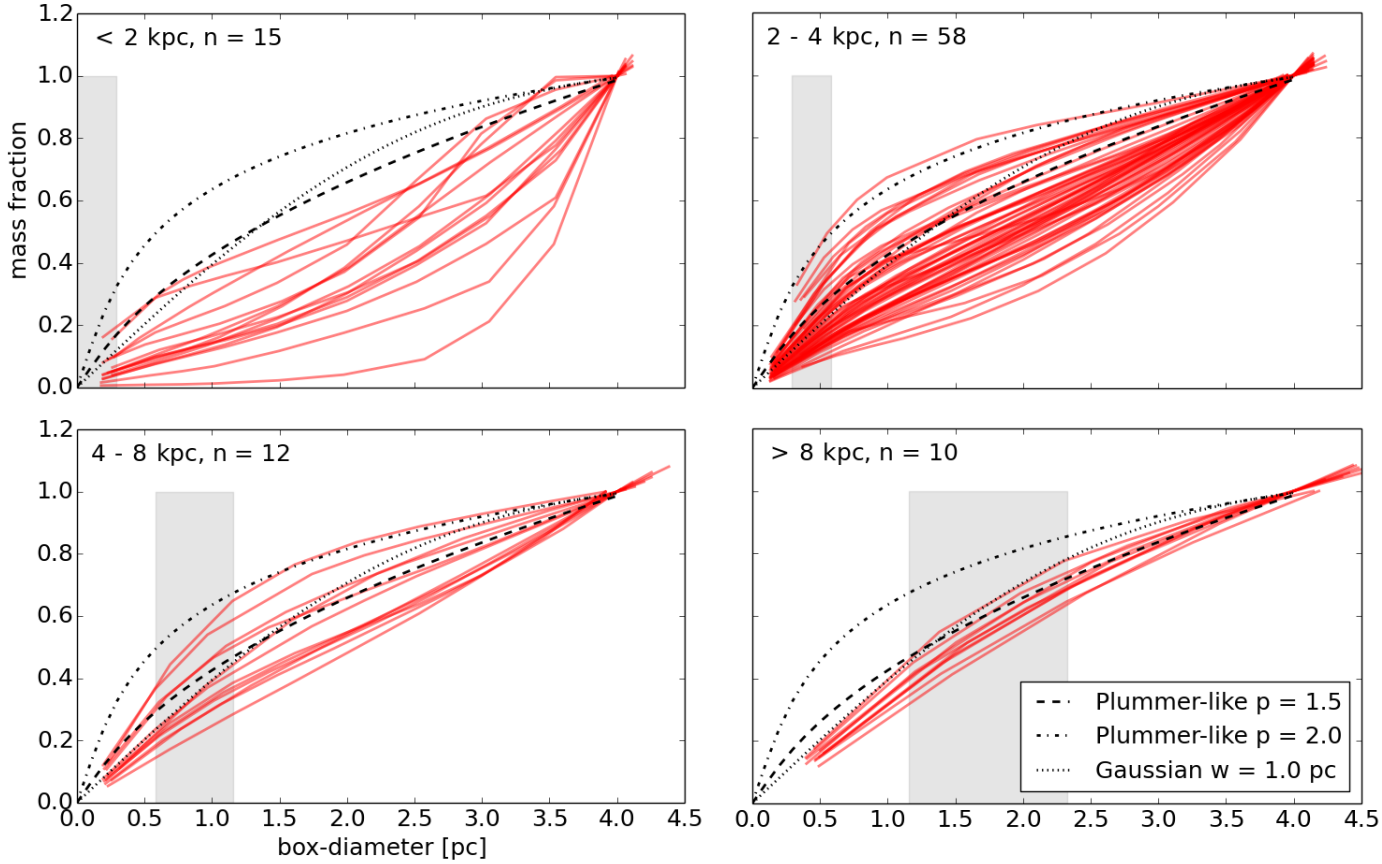

Fig. B.1. Fraction of the filament mass derived from corrected ATLASGAL+PLANCK dust continuum emission dependent on the box-diameter of the mask separated with distances. *Top left:* $d < 2$ kpc, *Top right:* 2 kpc $< d < 4$ kpc, *Bottom left:* 4 kpc $< d < 8$ kpc, *Bottom right:* $d > 8$ kpc. The gray lines indicate the physical beam size at these distances. The black lines show the theoretical profiles, which describe a Plummer-like $p = 1.5$ (dashed) or $p = 2.0$ (dash-dotted), and a Gaussian with $w = 1.0$ (dotted).

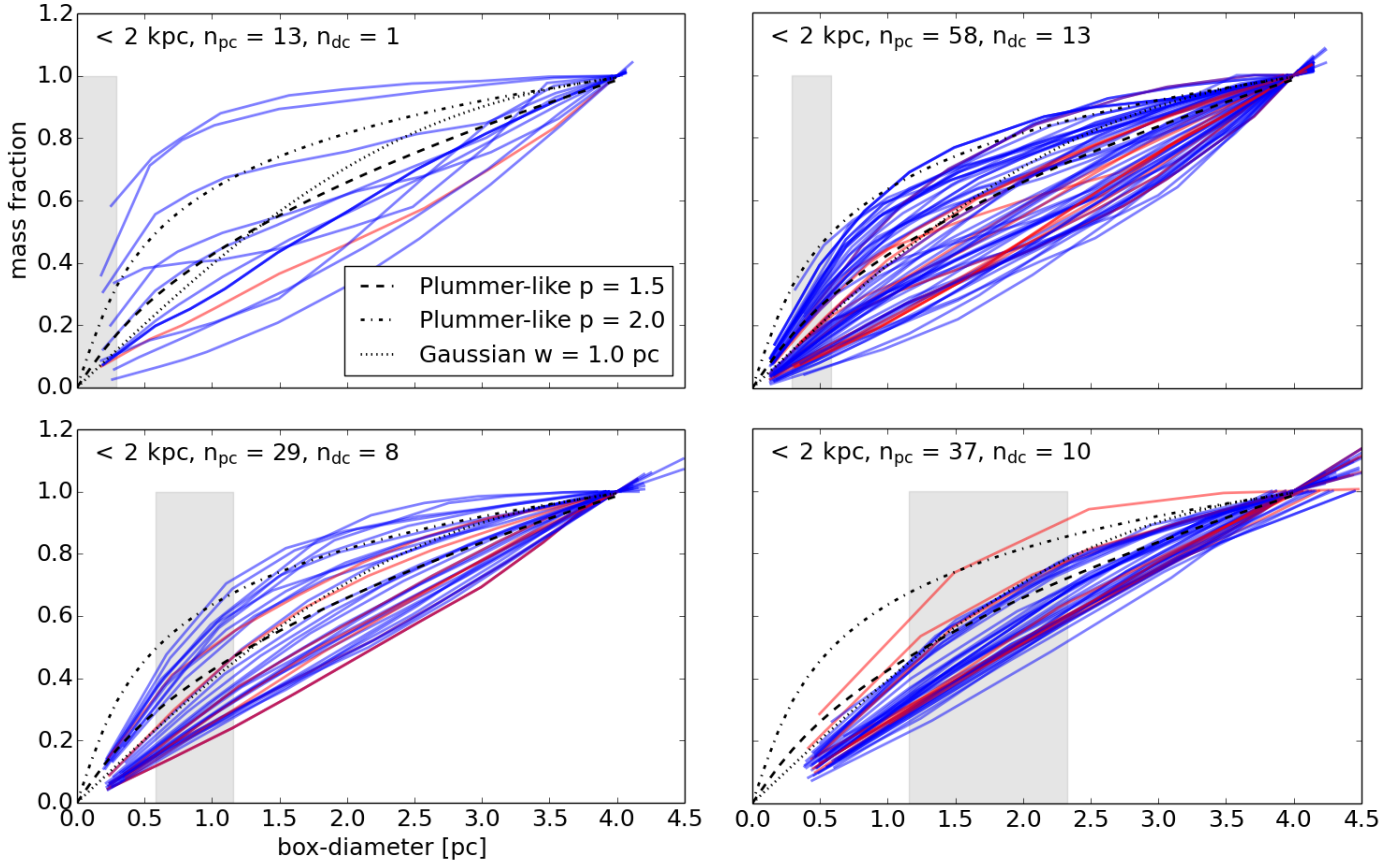

Fig. B.2. Fraction of the filament mass for partially correlated (blue) and diffuse component (red) filaments derived from ^{13}CO emission dependent on the box-diameter of the mask separated with distances. *Top left:* $d < 2$ kpc, *Top right:* 2 kpc $< d < 4$ kpc, *Bottom left:* 4 kpc $< d < 8$ kpc, *Bottom right:* $d > 8$ kpc. The vertical gray lines indicate the physical beam size at these distances. The black lines show the theoretical profiles, which describe a Plummer-like $p = 1.5$ (dashed) or $p = 2.0$ (dash-dotted), and a Gaussian with $w = 1.0$ (dotted).

Table 5. tbd

Filament ID	ℓ °	b °	Status	N_c	$v_{lsr}(^{13}CO)$ km s^{-1}	$v_{lsr}(C^{18}O)$ km s^{-1}	$\sigma(v_{^{13}CO})$ km s^{-1}	$\sigma(v_{C^{18}O})$ km s^{-1}	σ_v km s^{-1}	$\sigma_v(^{13}CO)$ km s^{-1}	$\sigma_v(C^{18}O)$ km s^{-1}	$\sigma_{v,t}(^{13}CO)$ km s^{-1}	$\sigma_{v,t}(C^{18}O)$ km s^{-1}
G000.615-00.448_0	0.61	-0.45	full. cor.	1	15.69	15.75	0.56	7.18	0.84	0.95	0.5	1.19	1.16
G000.675+00.310_0	0.67	0.31	part. cor.	1	136.44	-	1.33	0.0	1.72	1.73	-	3.79	-
G000.914+00.308_0	0.91	0.31	part. cor.	1	174.07	173.73	1.99	0.0	1.94	1.95	-	4.46	4.88
G001.717+00.359_0	1.72	0.36	part. cor.	3	3.07	2.34	0.36	0.53	0.79	0.92	0.46	1.24	0.81
G001.717+00.359_1	1.72	0.36	part. cor.	3	8.93	-	0.44	1.19	0.97	1.07	0.61	1.76	-
G001.717+00.359_2	1.72	0.36	part. cor.	3	-17.3	-	3.17	0.0	1.73	1.74	-	4.65	-
G002.128+00.295_0	2.13	0.3	full. cor.	1	3.86	2.85	0.36	1.66	1.13	1.23	0.71	1.98	-
G002.210-00.049_0	2.21	-0.05	part. cor.	2	11.27	8.39	2.05	0.0	2.77	2.77	-	5.62	5.95
G002.210-00.049_1	2.21	-0.05	part. cor.	2	127.35	126.52	1.42	0.0	1.72	1.73	-	3.03	3.81
G002.370+00.069_0	2.37	0.07	dif. comp.	3	1.21	0.45	0.5	0.0	0.79	0.81	-	1.05	1.03
G002.370+00.069_1	2.37	0.07	full. cor.	3	7.56	7.67	0.89	1.36	1.38	1.41	0.64	2.17	2.18
G002.370+00.069_2	2.37	0.07	part. cor.	3	15.97	15.61	0.24	0.0	0.98	1.0	-	1.53	1.31
G002.420+00.205_0	2.42	0.21	part. cor.	1	6.68	7.05	0.75	2.5	0.91	1.1	0.71	2.14	2.05
G002.476-00.120_0	2.48	-0.12	part. cor.	2	6.99	6.28	1.13	0.0	1.31	1.33	-	2.56	2.75
G002.476-00.120_1	2.48	-0.12	part. cor.	2	14.93	13.99	0.84	0.0	0.94	0.97	-	1.83	-
G002.585-00.000_0	2.59	-0.0	part. cor.	2	-5.58	-5.49	0.76	1.59	1.13	1.17	1.0	1.7	1.62
G002.585-00.000_1	2.59	-0.0	dif. comp.	2	5.5	-	0.58	0.0	1.38	1.4	-	2.31	-
G002.687+00.106_0	2.69	0.11	full. cor.	1	10.68	9.69	1.35	4.43	1.25	2.01	0.64	3.98	-
G003.321-00.097_0	3.32	-0.1	part. cor.	2	3.61	3.69	0.81	0.54	1.27	1.34	0.7	1.91	1.68
G003.321-00.097_1	3.32	-0.1	part. cor.	2	10.24	9.79	1.13	3.48	1.35	1.56	1.15	2.09	1.45
G003.387+00.185_0	3.39	0.18	part. cor.	1	66.94	72.73	1.98	0.0	1.96	1.97	-	5.85	9.2
G003.446-00.223_0	3.45	-0.22	part. cor.	1	-23.25	-22.61	0.93	0.0	0.95	0.97	-	1.6	-
G003.456+00.006_0	3.46	0.01	full. cor.	1	5.11	5.07	0.62	2.17	1.05	1.33	0.61	1.94	-
G004.180-00.010_0	4.18	-0.01	part. cor.	3	6.22	5.23	0.53	1.6	0.69	0.76	0.5	1.46	1.24
G004.180-00.010_1	4.18	-0.01	full. cor.	3	14.61	14.51	1.03	3.66	1.27	1.37	0.57	2.13	2.46
G004.180-00.010_2	4.18	-0.01	part. cor.	3	27.11	26.08	0.78	9.62	0.99	1.21	0.85	1.66	-
G004.583-00.109_0	4.58	-0.11	part. cor.	2	13.79	13.71	0.74	4.35	1.2	1.39	0.59	2.2	1.73
G004.583-00.109_1	4.58	-0.11	part. cor.	2	25.1	23.24	1.55	0.0	1.32	1.33	-	2.33	-
G004.705+00.001_0	4.7	0.0	full. cor.	1	10.32	10.54	0.52	5.03	1.74	2.81	0.58	3.24	2.2
G004.711-00.440_0	4.71	-0.44	full. cor.	1	5.91	5.47	0.24	1.52	0.7	0.76	0.41	0.98	0.99
G004.794-00.284_0	4.79	-0.28	full. cor.	2	6.77	6.67	0.25	0.0	0.74	0.77	-	1.07	0.73
G004.794-00.284_1	4.79	-0.28	part. cor.	2	12.15	11.76	0.37	0.0	1.05	1.07	-	1.4	1.11
G004.950-00.076_0	4.95	-0.08	full. cor.	1	11.01	11.33	0.73	3.3	1.13	1.23	1.02	1.95	1.09
G005.101-00.104_0	5.1	-0.1	full. cor.	1	45.0	44.99	0.81	16.57	1.07	1.21	0.7	1.61	1.66
G005.357+00.101_0	5.36	0.1	full. cor.	1	10.98	11.18	0.82	5.21	0.75	1.13	0.58	2.13	1.17
G005.454+00.167_0	5.45	0.17	full. cor.	1	12.92	13.24	0.32	0.0	1.09	1.11	-	1.6	1.7
G005.704-00.306_0	5.7	-0.31	full. cor.	1	7.54	7.41	0.28	0.0	1.27	1.29	-	1.45	1.15
G005.912+00.283_0	5.91	0.28	part. cor.	1	57.99	-	1.93	0.0	1.52	1.54	-	3.27	-
G005.930-00.095_0	5.93	-0.09	part. cor.	1	15.3	15.78	0.26	3.95	0.7	0.74	0.58	0.92	0.61
G006.589-00.106_0	6.59	-0.11	part. cor.	2	5.05	6.37	0.78	0.42	1.13	1.19	0.78	1.57	1.38
G006.589-00.106_1	6.59	-0.11	part. cor.	2	15.35	15.46	2.55	5.55	1.71	1.96	1.09	3.6	2.99
G006.849+00.151_0	6.85	0.15	part. cor.	2	18.46	18.48	0.76	0.0	1.04	1.06	-	2.07	2.02
G006.849+00.151_1	6.85	0.15	part. cor.	2	-17.1	-16.98	0.86	0.0	1.12	1.14	-	1.75	2.34

Table 5. continued.

Filament ID	ℓ °	b °	Status	N_c	$v_{lsr}(^{13}CO)$ km s^{-1}	$v_{lsr}(C^{18}O)$ km s^{-1}	$\sigma(v_{^{13}CO})$ km s^{-1}	$\sigma(v_{C^{18}O})$ km s^{-1}	σ_v km s^{-1}	$\sigma_v(^{13}CO)$ km s^{-1}	$\sigma_v(C^{18}O)$ km s^{-1}	$\sigma_{v,t}(^{13}CO)$ km s^{-1}	$\sigma_{v,t}(C^{18}O)$ km s^{-1}
G007.250-00.120_0	7.25	-0.12	part. cor.	2	18.21	18.68	0.37	2.5	0.86	0.9	0.68	0.96	0.27
G007.250-00.120_1	7.25	-0.12	part. cor.	2	22.76	22.85	0.63	10.2	1.02	1.28	0.62	1.57	1.34
G008.000-00.272_0	8.0	-0.27	full. cor.	1	40.72	40.56	0.48	15.76	1.01	1.5	0.88	1.71	1.22
G008.255+00.165_0	8.25	0.16	full. cor.	1	18.87	19.03	0.27	0.34	0.79	1.36	0.71	1.41	1.21
G008.800-00.359_0	8.8	-0.36	full. cor.	2	38.18	38.35	0.64	18.79	1.15	1.45	0.66	1.77	0.61
G008.800-00.359_1	8.8	-0.36	part. cor.	2	20.21	20.15	0.36	7.51	0.85	0.94	0.55	1.29	1.47
G008.914-00.318_0	8.91	-0.32	full. cor.	1	38.03	38.1	0.49	19.21	1.06	1.3	0.63	1.56	-
G009.230+00.157_0	9.23	0.16	full. cor.	1	16.97	17.22	0.35	4.59	0.7	1.04	0.61	1.14	0.89
G009.280-00.152_0	9.28	-0.15	full. cor.	1	40.97	41.75	0.28	0.29	0.74	1.36	0.64	1.56	-
G009.970-00.024_0	9.97	-0.02	part. cor.	3	49.46	48.9	0.83	21.86	1.12	1.43	0.83	2.25	1.43
G009.970-00.024_1	9.97	-0.02	part. cor.	3	11.12	10.87	0.44	0.0	1.21	1.23	-	2.03	2.53
G009.970-00.024_2	9.97	-0.02	dif. comp.	3	17.51	15.94	0.36	0.0	0.67	0.7	-	1.13	-
G010.531-00.024_0	10.53	-0.02	part. cor.	1	69.23	69.18	1.51	18.22	1.53	1.63	0.98	2.68	2.75
G010.682-00.161_0	10.68	-0.16	full. cor.	4	29.52	29.75	0.78	14.62	1.73	2.23	0.87	2.83	1.96
G010.682-00.161_1	10.68	-0.16	dif. comp.	4	42.6	-	0.87	0.0	0.95	0.97	-	2.16	-
G010.682-00.161_2	10.68	-0.16	part. cor.	4	51.4	51.9	0.41	17.38	0.97	1.25	0.75	1.31	-
G010.682-00.161_3	10.68	-0.16	dif. comp.	4	-8.08	-	3.32	0.0	0.85	0.88	-	3.88	-
G010.694+00.034_0	10.69	0.03	part. cor.	3	18.92	19.07	0.79	5.3	1.36	1.6	0.6	2.13	2.28
G010.694+00.034_1	10.69	0.03	full. cor.	3	30.81	31.21	2.24	9.87	2.34	2.52	0.81	3.77	3.74
G010.694+00.034_2	10.69	0.03	part. cor.	3	39.19	-	0.43	0.0	0.97	0.99	-	1.15	-
G010.809-00.393_0	10.81	-0.39	part. cor.	2	-0.26	-1.13	0.9	0.54	1.31	1.42	1.01	1.96	1.98
G010.809-00.393_1	10.81	-0.39	part. cor.	2	30.82	29.2	0.47	0.0	0.98	1.0	-	1.78	-
G010.878-00.468_0	10.88	-0.47	part. cor.	2	32.77	33.07	0.63	9.55	1.45	1.65	0.6	2.97	0.86
G010.878-00.468_1	10.88	-0.47	part. cor.	2	-0.63	0.06	1.65	0.17	1.21	1.26	0.61	2.08	1.99
G010.971-00.363_0	10.97	-0.36	full. cor.	2	-1.01	-0.94	0.71	0.29	1.32	1.39	0.67	1.69	1.24
G010.971-00.363_1	10.97	-0.36	part. cor.	2	33.91	34.53	0.6	0.0	1.61	1.63	-	2.42	2.05
G011.046-00.069_0	11.05	-0.07	dif. comp.	3	10.99	8.69	0.63	0.68	1.07	1.09	0.46	1.89	-
G011.046-00.069_1	11.05	-0.07	part. cor.	3	19.72	21.03	1.83	4.65	1.24	1.44	0.76	2.53	2.15
G011.046-00.069_2	11.05	-0.07	full. cor.	3	30.0	30.01	1.06	14.75	1.06	1.35	0.68	1.93	1.71
G011.612-00.383_0	11.61	-0.38	full. cor.	1	30.64	30.43	0.3	0.0	1.83	1.84	-	2.48	2.12
G012.405-00.138_0	12.41	-0.14	full. cor.	2	33.61	33.75	0.39	11.92	1.14	1.25	0.57	1.35	1.22
G012.405-00.138_1	12.41	-0.14	part. cor.	2	120.88	120.44	0.53	0.0	0.81	0.84	-	1.1	1.12
G012.529-00.314_0	12.53	-0.31	full. cor.	3	34.8	34.68	0.5	14.83	1.08	1.2	0.81	1.4	0.59
G012.529-00.314_1	12.53	-0.31	dif. comp.	3	40.27	40.49	0.53	0.0	0.58	0.61	-	0.93	0.93
G012.529-00.314_2	12.53	-0.31	dif. comp.	3	9.82	8.16	0.73	0.0	1.25	1.26	-	2.23	-
G012.543+00.011_0	12.54	0.01	part. cor.	2	45.69	45.49	0.44	8.38	1.27	1.32	0.8	2.06	1.42
G012.543+00.011_1	12.54	0.01	part. cor.	2	34.49	-	0.21	0.0	0.8	0.83	-	1.17	-
G012.543-00.092_0	12.54	-0.09	part. cor.	3	36.46	36.61	0.85	0.0	1.24	1.26	-	1.93	2.59
G012.543-00.092_1	12.54	-0.09	full. cor.	3	50.96	51.02	0.83	5.42	1.27	1.32	0.39	2.42	2.84
G012.543-00.092_2	12.54	-0.09	dif. comp.	3	21.5	21.15	1.1	0.0	1.06	1.08	-	1.77	-
G012.595+00.116_0	12.59	0.12	part. cor.	1	56.98	57.18	0.68	20.0	0.88	0.98	0.75	1.28	0.96
G012.893+00.496_0	12.89	0.5	full. cor.	2	32.72	32.7	0.58	5.12	0.96	1.49	0.96	1.77	1.04
G012.893+00.496_1	12.89	0.5	full. cor.	2	18.39	19.06	0.45	0.0	0.86	0.89	-	1.05	-

Table 5. continued.

Filament ID	ℓ °	b °	Status	N_c	$v_{lsr}(^{13}CO)$ km s^{-1}	$v_{lsr}(C^{18}O)$ km s^{-1}	$\sigma(v_{^{13}CO})$ km s^{-1}	$\sigma(v_{C^{18}O})$ km s^{-1}	σ_v km s^{-1}	$\sigma_v(^{13}CO)$ km s^{-1}	$\sigma_v(C^{18}O)$ km s^{-1}	$\sigma_{v,t}(^{13}CO)$ km s^{-1}	$\sigma_{v,t}(C^{18}O)$ km s^{-1}
G013.220+00.164_0	13.22	0.16	full. cor.	2	53.81	54.21	0.33	0.0	1.21	1.23	-	1.57	1.6
G013.220+00.164_1	13.22	0.16	part. cor.	2	17.92	18.55	0.82	0.0	1.21	1.23	-	2.26	2.53
G013.282-00.316_0	13.28	-0.32	full. cor.	2	39.44	40.1	0.89	19.77	1.87	2.2	0.8	3.14	2.53
G013.282-00.316_1	13.28	-0.32	part. cor.	2	17.53	18.22	1.45	3.91	2.08	2.19	0.5	3.46	2.43
G013.313+00.193_0	13.31	0.19	full. cor.	2	18.16	18.27	0.58	8.22	0.85	0.95	0.61	1.13	0.7
G013.313+00.193_1	13.31	0.19	part. cor.	2	53.13	54.95	0.37	8.89	0.84	0.9	0.66	1.27	-
G013.460+00.171_0	13.46	0.17	full. cor.	1	18.16	18.08	0.29	4.64	1.1	1.15	0.62	1.23	-
G013.700-00.072_0	13.7	-0.07	part. cor.	1	47.89	47.21	0.98	23.35	0.88	1.19	0.74	1.65	1.11
G013.893-00.129_0	13.89	-0.13	full. cor.	2	39.12	38.95	0.49	19.67	1.39	1.7	0.7	1.81	1.33
G013.893-00.129_1	13.89	-0.13	part. cor.	2	17.56	16.99	0.75	8.19	1.32	1.62	0.99	2.09	2.1
G014.005+00.311_0	14.01	0.31	full. cor.	1	46.14	45.3	0.77	12.36	1.16	1.25	0.58	1.86	1.83
G014.117-00.392_0	14.12	-0.39	full. cor.	2	38.38	38.03	0.6	15.46	1.68	1.78	0.68	2.45	1.33
G014.117-00.392_1	14.12	-0.39	full. cor.	2	20.83	-	0.64	0.0	1.67	1.69	-	2.61	-
G014.627-00.123_0	14.63	-0.12	full. cor.	1	40.59	40.46	0.65	19.94	1.55	1.76	0.87	2.28	2.07
G014.789-00.478_0	14.79	-0.48	full. cor.	1	22.0	21.15	0.67	8.88	1.11	1.25	0.4	1.72	1.37
G014.919-00.065_0	14.92	-0.06	full. cor.	1	28.3	28.44	0.75	0.0	1.31	1.33	-	2.52	2.12
G015.611-00.476_0	15.61	-0.48	full. cor.	2	16.21	15.91	1.05	7.41	0.63	0.72	0.63	1.27	1.25
G015.611-00.476_1	15.61	-0.48	part. cor.	2	-4.2	-	0.78	0.0	1.14	1.16	-	1.66	-
G015.653-00.224_0	15.65	-0.22	full. cor.	1	57.4	57.5	0.69	24.27	0.61	0.77	0.59	1.04	0.7
G016.609-00.069_0	16.61	-0.07	part. cor.	2	59.06	59.22	0.94	22.42	0.79	1.0	0.71	1.54	1.25
G016.609-00.069_1	16.61	-0.07	part. cor.	2	41.25	40.82	1.01	14.72	0.96	1.26	0.71	2.72	1.17
G016.661+00.121_0	16.66	0.12	full. cor.	1	15.23	15.21	0.28	5.42	0.64	0.7	0.55	0.8	0.5
G016.700-00.235_0	16.7	-0.24	part. cor.	2	55.93	56.71	0.61	8.44	0.89	0.92	0.69	1.44	-
G016.700-00.235_1	16.7	-0.24	part. cor.	2	28.4	28.12	1.1	0.0	1.17	1.19	-	1.89	1.63
G016.757+00.013_0	16.76	0.01	full. cor.	1	33.99	34.96	0.6	6.31	1.33	1.37	0.84	2.23	-
G016.919+00.275_0	16.92	0.27	full. cor.	1	24.3	24.34	0.3	8.62	1.13	1.39	0.76	1.4	1.14
G016.929-00.082_0	16.93	-0.08	full. cor.	2	40.85	40.86	0.32	14.5	0.72	0.81	0.48	1.02	0.37
G016.929-00.082_1	16.93	-0.08	dif. comp.	2	-4.42	-4.91	0.98	0.0	1.13	1.15	-	1.54	2.03
G016.998+00.280_0	17.0	0.28	full. cor.	1	23.35	23.66	0.67	10.71	1.32	1.67	0.52	1.84	1.68
G301.638-00.239_0	301.64	-0.24	full. cor.	1	-37.2	-37.34	0.5	12.09	0.96	1.34	0.66	1.41	0.6
G305.560-00.003_0	305.56	-0.0	full. cor.	1	-38.53	-38.11	1.26	15.3	1.39	1.66	1.0	2.1	1.76
G309.161-00.358_0	309.16	-0.36	full. cor.	1	-41.7	-41.43	0.3	6.8	1.02	1.65	0.85	2.01	1.67
G313.703-00.181_0	313.7	-0.18	full. cor.	1	-44.49	-44.38	0.9	1.36	1.04	1.75	0.88	2.06	2.14
G313.717+00.103_0	313.72	0.1	part. cor.	3	-55.82	-56.33	0.65	27.19	0.75	0.97	0.63	1.11	0.87
G313.717+00.103_1	313.72	0.1	dif. comp.	3	-50.55	-49.07	0.27	0.0	0.76	0.78	-	0.99	-
G313.717+00.103_2	313.72	0.1	full. cor.	3	-44.87	-44.83	0.19	22.4	0.79	1.1	0.57	1.1	0.76
G314.219+00.266_0	314.22	0.27	full. cor.	1	-60.53	-60.7	1.36	11.61	1.31	1.95	1.04	2.43	2.5
G314.284+00.100_0	314.28	0.1	full. cor.	2	-56.6	-56.2	0.48	25.54	1.17	1.33	0.76	1.47	0.96
G314.284+00.100_1	314.28	0.1	full. cor.	2	-50.3	-50.24	0.85	17.16	1.1	1.86	1.01	2.14	1.62
G317.386+00.113_0	317.39	0.11	full. cor.	1	-43.42	-43.27	1.66	13.37	1.45	1.98	1.0	2.71	2.67
G317.889-00.256_0	317.89	-0.26	full. cor.	1	-36.53	-35.99	0.65	12.09	1.31	1.77	1.04	1.96	1.68
G320.240+00.027_0	320.24	0.03	full. cor.	1	-9.88	-10.4	0.5	4.36	1.37	1.64	0.76	1.75	1.4
G320.243+00.406_0	320.24	0.41	part. cor.	1	-32.72	-32.4	0.37	16.01	0.83	0.98	0.84	1.22	0.93

Table 5. continued.

Filament ID	ℓ °	b °	Status	N_c	$v_{lsr}(^{13}CO)$ km s^{-1}	$v_{lsr}(C^{18}O)$ km s^{-1}	$\sigma(v_{^{13}CO})$ km s^{-1}	$\sigma(v_{C^{18}O})$ km s^{-1}	σ_v km s^{-1}	$\sigma_v(^{13}CO)$ km s^{-1}	$\sigma_v(C^{18}O)$ km s^{-1}	$\sigma_{v,t}(^{13}CO)$ km s^{-1}	$\sigma_{v,t}(C^{18}O)$ km s^{-1}
G320.270-00.299_0	320.27	-0.3	full. cor.	1	-65.81	-65.6	1.01	30.69	1.34	1.7	1.01	2.09	1.46
G320.883-00.392_0	320.88	-0.39	full. cor.	1	-45.1	-45.08	0.46	6.77	0.84	1.33	0.81	1.54	1.2
G323.179+00.149_0	323.18	0.15	full. cor.	1	-65.96	-65.91	0.73	25.98	0.83	1.18	0.81	1.39	1.31
G323.929+00.036_0	323.93	0.04	full. cor.	1	-57.18	-57.23	0.64	24.27	1.69	1.78	0.73	2.23	2.02
G326.552+00.165_0	326.55	0.16	full. cor.	1	-74.69	-74.51	0.74	37.17	1.36	1.6	0.92	1.91	1.28
G326.586+00.050_0	326.59	0.05	full. cor.	1	-75.73	-75.55	0.49	0.0	1.25	1.27	-	1.73	-
G326.722-00.099_0	326.72	-0.1	full. cor.	1	-58.65	-57.08	1.23	13.52	1.73	1.79	0.79	2.74	0.9
G326.790-00.119_0	326.79	-0.12	full. cor.	1	-56.53	-56.27	0.52	25.21	1.29	1.76	0.87	1.97	1.18
G327.036-00.408_0	327.04	-0.41	full. cor.	1	-63.89	-63.57	0.84	26.58	1.09	1.56	0.74	1.97	1.25
G327.042-00.169_0	327.04	-0.17	full. cor.	1	-60.1	-60.55	0.63	26.22	1.47	1.63	0.69	1.94	1.33
G327.157-00.256_0	327.16	-0.26	full. cor.	1	-61.49	-61.52	1.33	24.59	1.59	2.23	0.94	2.85	2.52
G327.258-00.420_0	327.26	-0.42	full. cor.	1	-48.01	-48.14	0.45	23.36	1.18	1.34	0.72	1.43	1.54
G327.396+00.452_0	327.4	0.45	full. cor.	1	-79.89	-79.35	0.48	38.14	1.44	1.75	1.04	2.29	1.85
G327.870+00.157_0	327.87	0.16	part. cor.	2	-92.65	-92.01	1.76	37.96	1.13	1.33	1.04	2.32	1.88
G327.870+00.157_1	327.87	0.16	dif. comp.	2	-50.25	-49.27	0.92	14.87	1.02	1.36	0.59	2.13	2.19
G327.884+00.002_0	327.88	0.0	full. cor.	2	-97.17	-96.4	0.55	18.94	1.17	1.2	0.95	1.5	1.13
G327.884+00.002_1	327.88	0.0	part. cor.	2	-49.48	-48.14	0.51	0.0	0.78	0.81	-	0.86	-
G327.981-00.101_0	327.98	-0.1	full. cor.	1	-48.87	-48.63	0.85	20.19	1.49	1.78	0.86	2.22	2.11
G328.627+00.063_0	328.63	0.06	part. cor.	2	-85.69	-	0.28	0.0	0.81	0.84	-	1.06	-
G328.627+00.063_1	328.63	0.06	part. cor.	2	-56.59	-	0.48	0.0	1.07	1.09	-	1.6	-
G328.773+00.304_0	328.77	0.3	full. cor.	2	-101.44	-101.79	0.57	41.63	1.35	1.54	0.59	1.8	1.3
G328.773+00.304_1	328.77	0.3	dif. comp.	2	-86.01	-	0.2	0.0	0.75	0.78	-	1.31	-
G328.940+00.277_0	328.94	0.28	full. cor.	1	-88.82	-89.06	0.54	0.0	1.4	1.42	-	1.65	0.99
G330.348-00.122_0	330.35	-0.12	part. cor.	1	-95.97	-95.96	0.64	0.0	1.42	1.43	-	1.87	1.88
G330.760-00.306_0	330.76	-0.31	full. cor.	2	-63.07	-63.32	0.67	29.64	1.51	1.78	0.93	1.99	1.29
G330.760-00.306_1	330.76	-0.31	part. cor.	2	-53.2	-54.38	0.64	0.0	0.94	0.96	-	1.96	1.88
G330.973+00.076_0	330.97	0.08	part. cor.	3	-50.47	-50.37	0.59	12.48	1.11	1.23	0.64	1.67	0.94
G330.973+00.076_1	330.97	0.08	part. cor.	3	-61.5	-59.71	0.63	7.58	1.12	1.18	0.52	1.76	-
G330.973+00.076_2	330.97	0.08	part. cor.	3	-32.91	-33.82	0.38	5.56	0.75	0.81	0.65	0.87	-
G330.986+00.337_0	330.99	0.34	full. cor.	1	-55.7	-55.69	0.38	27.43	0.93	1.18	0.77	1.28	0.87
G331.533+00.241_0	331.53	0.24	dif. comp.	3	-62.31	-	0.31	0.0	1.04	1.06	-	1.43	-
G331.533+00.241_1	331.53	0.24	part. cor.	3	-55.63	-55.99	1.2	22.38	1.08	1.32	0.56	1.88	1.58
G331.533+00.241_2	331.53	0.24	part. cor.	3	-92.3	-92.12	0.56	15.41	1.13	1.2	0.53	1.63	1.46
G331.670-00.272_0	331.67	-0.27	full. cor.	3	-48.12	-48.17	0.67	15.48	0.66	0.93	0.64	1.18	1.06
G331.670-00.272_1	331.67	-0.27	dif. comp.	3	-99.78	-97.94	0.71	0.0	0.91	0.93	-	1.39	-
G331.670-00.272_2	331.67	-0.27	part. cor.	3	-94.07	-94.29	0.82	0.0	1.25	1.26	-	1.85	1.77
G331.973-00.378_0	331.97	-0.38	full. cor.	1	-60.3	-60.44	0.81	30.0	1.0	1.25	0.7	1.5	1.41
G332.000+00.011_0	332.0	0.01	full. cor.	2	-55.08	-54.18	1.68	8.97	2.32	2.4	0.52	3.6	2.38
G332.000+00.011_1	332.0	0.01	part. cor.	2	-87.04	-87.77	0.91	0.0	1.59	1.6	-	2.63	2.63
G332.370-00.080_0	332.37	-0.08	dif. comp.	3	-58.92	-58.31	0.63	0.0	0.98	1.0	-	1.31	0.06
G332.370-00.080_1	332.37	-0.08	full. cor.	3	-48.2	-48.12	2.06	23.57	1.18	1.51	0.83	3.15	2.92
G332.370-00.080_2	332.37	-0.08	dif. comp.	3	-87.66	-88.02	1.57	16.15	1.27	1.39	0.76	2.71	2.53
G332.610+00.052_0	332.61	0.05	full. cor.	1	-94.91	-95.27	0.97	29.09	1.24	1.33	0.69	2.27	1.62

Table 5. continued.

Filament ID	ℓ °	b °	Status	N_c	$v_{lsr}(^{13}CO)$ km s^{-1}	$v_{lsr}(C^{18}O)$ km s^{-1}	$\sigma(v_{^{13}CO})$ km s^{-1}	$\sigma(v_{C^{18}O})$ km s^{-1}	σ_v km s^{-1}	$\sigma_v(^{13}CO)$ km s^{-1}	$\sigma_v(C^{18}O)$ km s^{-1}	$\sigma_{v,t}(^{13}CO)$ km s^{-1}	$\sigma_{v,t}(C^{18}O)$ km s^{-1}
G332.852-00.214_0	332.85	-0.21	full. cor.	1	-42.06	-42.19	0.63	16.28	1.36	1.45	0.81	1.89	1.93
G333.007+00.452_0	333.01	0.45	full. cor.	1	-47.14	-	0.86	0.0	1.28	1.3	-	2.28	-
G333.063+00.181_0	333.06	0.18	full. cor.	1	-51.13	-50.78	1.06	21.78	1.94	2.2	0.96	3.23	2.87
G333.202-00.250_0	333.2	-0.25	part. cor.	3	-54.86	-55.42	1.37	0.0	0.97	0.99	-	1.67	1.63
G333.202-00.250_1	333.2	-0.25	part. cor.	3	-48.23	-49.39	2.03	0.0	1.13	1.15	-	2.5	1.48
G333.202-00.250_2	333.2	-0.25	part. cor.	3	-38.5	-	1.22	0.0	0.87	0.89	-	1.87	-
G333.297+00.073_0	333.3	0.07	full. cor.	2	-48.32	-48.42	1.09	23.89	1.59	1.85	1.01	2.38	1.67
G333.297+00.073_1	333.3	0.07	part. cor.	2	-70.21	-70.54	0.72	18.21	1.21	1.34	0.78	1.75	1.0
G333.481+00.165_0	333.48	0.16	full. cor.	1	-103.6	-103.82	0.29	30.98	0.84	0.88	0.79	0.88	0.91
G333.722+00.361_0	333.72	0.36	full. cor.	1	-33.99	-33.96	0.6	7.1	0.81	1.16	0.78	1.39	1.12
G333.868-00.312_0	333.87	-0.31	full. cor.	1	-46.4	-45.11	1.49	20.98	2.49	3.19	0.92	3.91	3.44
G333.899-00.106_0	333.9	-0.11	part. cor.	2	-93.62	-93.46	0.25	19.82	0.8	0.86	0.49	1.16	1.36
G333.899-00.106_1	333.9	-0.11	part. cor.	2	-41.82	-39.96	1.2	9.21	1.56	1.79	1.04	2.96	2.49
G333.985+00.224_0	333.98	0.22	part. cor.	5	-83.25	-82.64	0.38	12.38	0.76	0.8	0.31	1.22	1.1
G333.985+00.224_1	333.98	0.22	part. cor.	5	-48.13	-	1.04	9.73	0.97	1.02	0.44	1.77	-
G333.985+00.224_2	333.98	0.22	dif. comp.	5	-42.14	-	0.45	0.0	0.8	0.82	-	1.33	-
G333.985+00.224_3	333.98	0.22	part. cor.	5	-60.19	-60.08	1.9	16.15	1.02	1.1	0.54	2.09	1.93
G333.985+00.224_4	333.98	0.22	dif. comp.	5	-93.89	-	1.18	0.0	1.06	1.08	-	3.07	-
G333.992+00.058_0	333.99	0.06	full. cor.	3	-86.06	-86.01	0.68	24.2	1.78	1.89	0.7	2.86	2.73
G333.992+00.058_1	333.99	0.06	part. cor.	3	-44.96	-45.34	1.49	11.23	1.34	1.4	0.59	3.15	2.66
G333.992+00.058_2	333.99	0.06	part. cor.	3	-60.56	-60.18	0.8	18.22	0.9	1.03	0.75	1.28	0.99
G334.056+00.489_0	334.06	0.49	full. cor.	1	-59.72	-60.27	0.59	0.0	1.66	1.68	-	2.52	0.84
G334.070-00.257_0	334.07	-0.26	part. cor.	2	-48.76	-48.16	0.31	0.0	0.95	0.98	-	1.39	1.0
G334.070-00.257_1	334.07	-0.26	part. cor.	2	-43.63	-42.7	0.49	0.0	1.17	1.19	-	1.9	2.27
G334.202+00.156_0	334.2	0.16	full. cor.	2	-89.28	-88.54	0.83	29.13	1.83	1.96	0.61	2.86	2.39
G334.202+00.156_1	334.2	0.16	part. cor.	2	-40.47	-39.8	1.08	0.0	1.36	1.37	-	2.47	2.58
G334.267-00.107_0	334.27	-0.11	full. cor.	2	-86.23	-86.01	0.85	9.93	1.21	1.24	0.67	1.75	1.17
G334.267-00.107_1	334.27	-0.11	part. cor.	2	-32.07	-32.8	1.5	3.61	1.29	1.34	0.74	2.58	-
G334.442+00.050_0	334.44	0.05	part. cor.	3	-90.46	-91.13	0.47	36.5	0.84	1.04	0.6	1.8	1.26
G334.442+00.050_1	334.44	0.05	part. cor.	3	-106.95	-108.36	1.36	0.0	1.16	1.18	-	1.97	-
G334.442+00.050_2	334.44	0.05	part. cor.	3	-70.86	-71.56	1.13	0.0	0.94	0.97	-	2.36	2.57
G334.617-00.270_0	334.62	-0.27	full. cor.	1	-46.18	-45.46	0.67	22.15	1.33	1.78	0.71	2.24	0.9
G334.640+00.426_0	334.64	0.43	full. cor.	1	-64.73	-64.55	0.39	31.84	1.02	1.24	0.81	1.52	0.82
G334.684+00.024_0	334.68	0.02	part. cor.	3	-32.05	-31.71	0.83	7.0	0.89	0.95	0.56	1.49	1.37
G334.684+00.024_1	334.68	0.02	dif. comp.	3	-27.49	-	0.11	0.0	0.65	0.68	-	0.67	-
G334.684+00.024_2	334.68	0.02	dif. comp.	3	-85.75	-	0.51	0.0	0.82	0.84	-	1.28	-
G334.840-00.196_0	334.84	-0.2	part. cor.	2	-43.77	-44.07	1.17	17.4	1.09	1.27	0.55	2.19	1.67
G334.840-00.196_1	334.84	-0.2	part. cor.	2	-27.81	-28.41	0.84	0.0	1.18	1.2	-	1.56	1.51
G335.008-00.268_0	335.01	-0.27	part. cor.	2	-27.06	-25.39	1.74	3.02	1.46	1.5	0.36	2.57	1.92
G335.008-00.268_1	335.01	-0.27	part. cor.	2	-18.75	-18.83	1.34	0.0	1.14	1.16	-	1.84	1.76
G335.083+00.065_0	335.08	0.07	part. cor.	1	-73.22	-74.25	0.79	0.0	1.11	1.13	-	1.86	0.57
G335.251-00.033_0	335.25	-0.03	full. cor.	1	-44.47	-44.59	0.43	10.95	1.02	1.07	0.65	1.75	1.72
G335.814+00.061_0	335.81	0.06	part. cor.	1	-89.59	-88.06	0.74	0.0	0.83	0.85	-	1.38	-

Table 5. continued.

Filament ID	ℓ °	b °	Status	N_c	$v_{lsr}(^{13}CO)$ km s^{-1}	$v_{lsr}(C^{18}O)$ km s^{-1}	$\sigma(v_{^{13}CO})$ km s^{-1}	$\sigma(v_{C^{18}O})$ km s^{-1}	σ_v km s^{-1}	$\sigma_v(^{13}CO)$ km s^{-1}	$\sigma_v(C^{18}O)$ km s^{-1}	$\sigma_{v,t}(^{13}CO)$ km s^{-1}	$\sigma_{v,t}(C^{18}O)$ km s^{-1}
G336.060+00.040_0	336.06	0.04	part. cor.	1	-118.02	-118.41	0.52	38.31	0.98	1.1	0.53	1.41	-
G336.062-00.271_0	336.06	-0.27	full. cor.	1	-39.23	-39.52	0.43	12.74	0.8	0.88	0.7	1.11	1.03
G336.194-00.457_0	336.19	-0.46	full. cor.	1	-87.77	-87.82	0.22	26.29	0.88	0.94	0.63	1.2	0.88
G336.248+00.310_0	336.25	0.31	part. cor.	2	-73.37	-72.87	1.5	10.76	1.01	1.07	0.64	1.85	1.94
G336.248+00.310_1	336.25	0.31	part. cor.	2	-44.94	-45.01	0.6	14.29	0.75	1.05	0.52	1.41	0.96
G336.376+00.204_0	336.38	0.2	full. cor.	2	-45.82	-46.26	0.88	7.58	1.07	1.1	0.72	1.8	1.51
G336.376+00.204_1	336.38	0.2	dif. comp.	2	-68.41	-68.73	1.05	12.53	0.97	1.07	0.7	1.78	1.65
G336.391+00.012_0	336.39	0.01	part. cor.	2	-128.65	-128.26	1.21	40.86	1.36	1.48	1.36	2.24	2.0
G336.391+00.012_1	336.39	0.01	dif. comp.	2	-39.03	-	0.39	3.38	0.89	0.98	0.45	2.14	-
G336.846+00.282_0	336.85	0.28	part. cor.	2	-77.16	-78.1	1.43	16.6	1.45	1.5	0.57	2.77	2.48
G336.846+00.282_1	336.85	0.28	part. cor.	2	-66.88	-67.05	0.76	22.57	0.92	1.13	0.72	1.33	1.01
G337.148-00.387_0	337.15	-0.39	full. cor.	2	-20.68	-20.61	0.65	0.0	0.74	0.77	-	1.17	1.29
G337.148-00.387_1	337.15	-0.39	part. cor.	2	-40.45	-41.11	0.52	6.81	0.87	0.94	0.72	1.2	0.86
G337.409-00.400_0	337.41	-0.4	part. cor.	2	-41.24	-41.42	0.48	20.23	1.01	1.26	1.1	1.78	1.37
G337.409-00.400_1	337.41	-0.4	dif. comp.	2	-54.26	-	0.21	10.05	0.7	0.77	0.51	0.78	-
G337.744-00.346_0	337.74	-0.35	full. cor.	1	-41.56	-41.58	0.6	19.85	0.99	1.22	0.72	1.69	1.16
G337.850+00.087_0	337.85	0.09	full. cor.	1	-54.82	-53.84	1.85	14.01	3.09	3.15	0.51	5.7	6.23
G338.181-00.477_0	338.18	-0.48	full. cor.	1	-36.88	-36.5	0.78	13.93	1.41	1.55	0.59	2.28	1.73
G338.279-00.295_0	338.28	-0.29	part. cor.	2	-13.54	-13.91	0.99	4.41	1.43	1.61	0.71	2.78	2.92
G338.279-00.295_1	338.28	-0.29	part. cor.	2	-122.35	-121.63	0.46	0.0	1.13	1.15	-	1.33	1.62
G338.291-00.119_0	338.29	-0.12	part. cor.	2	-91.93	-92.07	0.33	15.36	0.88	0.93	0.54	1.01	0.96
G338.291-00.119_1	338.29	-0.12	part. cor.	2	-116.16	-117.14	1.16	0.0	1.27	1.29	-	2.25	2.27
G338.528+00.214_0	338.53	0.21	part. cor.	1	-36.06	-35.78	0.64	12.04	1.34	1.48	0.86	2.12	2.11
G338.680-00.455_0	338.68	-0.45	full. cor.	2	-38.02	-39.32	0.37	13.01	1.17	1.28	0.62	2.17	-
G338.680-00.455_1	338.68	-0.45	part. cor.	2	-46.93	-	0.49	5.2	1.01	1.06	0.62	1.3	-
G338.708-00.328_0	338.71	-0.33	full. cor.	2	-45.24	-43.78	0.57	12.56	1.04	1.11	0.65	1.89	1.14
G338.708-00.328_1	338.71	-0.33	full. cor.	2	-31.77	-31.63	0.63	12.4	1.27	1.46	0.59	2.05	1.34
G338.749+00.159_0	338.75	0.16	full. cor.	1	-33.31	-34.75	0.74	15.59	1.79	1.99	1.0	2.92	-
G338.773+00.492_0	338.77	0.49	full. cor.	1	-62.87	-63.13	0.85	23.46	1.5	2.14	1.03	2.49	1.99
G338.806+00.111_0	338.81	0.11	full. cor.	1	-33.54	-34.6	0.68	9.56	1.7	1.84	0.67	2.66	-
G338.941-00.058_0	338.94	-0.06	part. cor.	2	-55.67	-56.54	0.84	12.33	0.92	0.96	0.76	1.42	-
G338.941-00.058_1	338.94	-0.06	part. cor.	2	-44.83	-45.54	1.37	22.96	1.23	1.6	1.0	2.6	2.02
G338.953+00.278_0	338.95	0.28	full. cor.	2	-55.15	-55.67	0.59	17.77	0.8	0.88	0.57	1.12	-
G338.953+00.278_1	338.95	0.28	part. cor.	2	-25.92	-25.32	1.14	3.48	1.31	1.32	0.42	2.46	2.23
G338.993+00.110_0	338.99	0.11	part. cor.	1	-28.15	-25.66	1.46	0.0	1.31	1.33	-	2.58	-
G339.077+00.153_0	339.08	0.15	part. cor.	2	-79.91	-79.84	1.27	33.74	1.31	1.5	1.03	2.28	2.49
G339.077+00.153_1	339.08	0.15	dif. comp.	2	-26.26	-22.5	1.55	0.0	1.15	1.17	-	2.7	-
G339.113-00.203_0	339.11	-0.2	full. cor.	3	-117.57	-117.98	1.59	38.08	1.38	1.57	0.73	2.6	2.34
G339.113-00.203_1	339.11	-0.2	part. cor.	3	-30.48	-30.66	0.71	4.0	1.02	1.05	0.69	1.72	1.66
G339.113-00.203_2	339.11	-0.2	part. cor.	3	-42.98	-43.04	0.31	13.21	0.98	1.1	0.69	1.28	1.37
G339.116-00.405_0	339.12	-0.41	full. cor.	1	-37.2	-37.35	0.78	16.3	1.05	1.4	0.7	1.73	1.73
G339.260+00.117_0	339.26	0.12	part. cor.	1	-72.43	-72.56	1.15	35.35	1.12	1.3	0.97	1.93	1.86
G339.385-00.414_0	339.38	-0.41	full. cor.	1	-38.69	-38.86	0.35	17.96	1.0	1.18	0.63	1.28	1.03

Table 5. continued.

Filament ID	ℓ °	b °	Status	N_c	$v_{lsr}(^{13}CO)$ km s^{-1}	$v_{lsr}(C^{18}O)$ km s^{-1}	$\sigma(v_{^{13}CO})$ km s^{-1}	$\sigma(v_{C^{18}O})$ km s^{-1}	σ_v km s^{-1}	$\sigma_v(^{13}CO)$ km s^{-1}	$\sigma_v(C^{18}O)$ km s^{-1}	$\sigma_{v,t}(^{13}CO)$ km s^{-1}	$\sigma_{v,t}(C^{18}O)$ km s^{-1}
G339.586-00.119_0	339.59	-0.12	full. cor.	2	-33.49	-33.94	1.35	13.95	1.3	2.01	0.89	2.78	2.19
G339.586-00.119_1	339.59	-0.12	part. cor.	2	-23.07	-23.82	1.09	2.82	1.11	1.14	0.96	1.93	1.02
G339.692+00.291_0	339.69	0.29	part. cor.	1	-92.69	-92.75	0.51	33.77	1.13	1.22	0.92	1.55	1.53
G339.988-00.165_0	339.99	-0.16	full. cor.	2	-51.65	-51.69	0.8	22.57	1.28	1.68	0.83	2.02	2.0
G339.988-00.165_1	339.99	-0.16	part. cor.	2	-36.58	-36.05	0.45	4.75	0.86	0.88	0.59	1.17	0.79
G340.301-00.387_0	340.3	-0.39	full. cor.	3	-48.24	-48.04	1.77	19.32	1.58	2.65	1.12	3.85	3.4
G340.301-00.387_1	340.3	-0.39	dif. comp.	3	-122.84	-122.58	1.6	0.0	1.13	1.15	-	2.18	2.21
G340.301-00.387_2	340.3	-0.39	dif. comp.	3	-91.41	-91.75	0.65	0.0	1.02	1.04	-	1.44	1.6
G340.316+00.079_0	340.32	0.08	part. cor.	2	-111.48	-111.5	1.44	53.62	0.83	1.01	0.67	1.74	1.9
G340.316+00.079_1	340.32	0.08	dif. comp.	2	-28.75	-28.58	0.36	0.0	1.05	1.08	-	1.62	1.85
G340.482-00.306_0	340.48	-0.31	part. cor.	3	-88.7	-88.84	0.44	40.35	0.83	1.14	0.66	1.28	1.07
G340.482-00.306_1	340.48	-0.31	part. cor.	3	-45.58	-45.78	0.71	0.0	1.78	1.79	-	2.4	1.97
G340.482-00.306_2	340.48	-0.31	part. cor.	3	-39.19	-38.55	0.39	11.57	1.19	1.32	0.62	1.59	1.63
G340.511-00.471_0	340.51	-0.47	full. cor.	1	-43.75	-43.09	1.18	18.62	1.85	2.04	0.86	2.52	1.5
G340.630-00.093_0	340.63	-0.09	part. cor.	3	-101.52	-	0.73	0.0	0.87	0.89	-	1.23	-
G340.630-00.093_1	340.63	-0.09	part. cor.	3	-48.1	-	1.34	0.0	1.71	1.73	-	2.41	-
G340.630-00.093_2	340.63	-0.09	part. cor.	3	-38.23	-	0.68	0.0	1.66	1.67	-	2.88	-
G340.981-00.013_0	340.98	-0.01	full. cor.	4	-47.06	-46.86	0.4	0.0	1.08	1.1	-	1.23	1.09
G340.981-00.013_1	340.98	-0.01	part. cor.	4	-40.29	-39.66	0.61	12.38	0.77	0.84	0.52	1.21	-
G340.981-00.013_2	340.98	-0.01	part. cor.	4	-32.25	-31.44	0.61	3.88	0.93	0.98	0.57	1.3	-
G340.981-00.013_3	340.98	-0.01	part. cor.	4	-27.51	-28.6	0.65	0.0	1.07	1.1	-	1.69	0.68
G341.244-00.265_0	341.24	-0.27	full. cor.	1	-43.55	-43.41	0.77	13.58	1.37	2.35	1.02	2.84	2.4
G341.415+00.244_0	341.42	0.24	full. cor.	3	-37.04	-37.51	0.23	13.61	1.01	1.1	0.6	1.3	-
G341.415+00.244_1	341.42	0.24	full. cor.	3	-24.03	-25.5	1.2	0.0	1.87	1.89	-	2.83	-
G341.415+00.244_2	341.42	0.24	part. cor.	3	-76.96	-78.13	0.41	15.5	0.81	0.86	0.5	1.09	-
G341.674+00.184_0	341.67	0.18	part. cor.	2	-15.77	-16.91	1.65	5.92	1.19	1.3	0.77	2.21	1.12
G341.674+00.184_1	341.67	0.18	part. cor.	2	-74.79	-	0.35	0.0	1.05	1.07	-	1.42	-
G341.938+00.054_0	341.94	0.05	full. cor.	2	-121.32	-121.24	0.65	31.92	0.83	0.88	0.6	1.11	-
G341.938+00.054_1	341.94	0.05	part. cor.	2	-22.61	-21.44	0.26	0.0	0.83	0.85	-	1.46	-
G342.100+00.399_0	342.1	0.4	part. cor.	7	-119.73	-119.75	0.56	50.34	0.88	1.16	0.73	1.37	1.19
G342.100+00.399_1	342.1	0.4	dif. comp.	7	-84.23	-83.93	0.56	0.0	0.63	0.66	-	0.98	0.78
G342.100+00.399_2	342.1	0.4	dif. comp.	7	-77.6	-77.38	0.62	14.7	1.15	1.21	0.71	1.61	1.61
G342.100+00.399_3	342.1	0.4	part. cor.	7	-71.36	-71.13	0.93	32.7	1.31	1.7	1.06	2.16	1.99
G342.100+00.399_4	342.1	0.4	dif. comp.	7	-25.5	-25.49	0.51	4.1	1.03	1.11	0.55	1.51	0.4
G342.100+00.399_5	342.1	0.4	dif. comp.	7	-40.7	-	0.26	0.0	0.9	0.93	-	1.08	-
G342.100+00.399_6	342.1	0.4	dif. comp.	7	-19.4	-	0.36	0.0	0.45	0.5	-	0.62	-
G342.345-00.005_0	342.34	-0.01	part. cor.	1	-6.41	-6.25	0.6	2.11	1.22	1.31	0.82	1.6	1.63
G342.357+00.113_0	342.36	0.11	part. cor.	5	-93.48	-93.72	0.65	45.65	0.77	0.93	0.72	1.3	1.05
G342.357+00.113_1	342.36	0.11	dif. comp.	5	-128.8	-128.03	1.44	0.0	1.32	1.34	-	2.27	2.31
G342.357+00.113_2	342.36	0.11	part. cor.	5	-7.08	-7.76	1.51	2.3	1.14	1.4	1.24	2.01	1.65
G342.357+00.113_3	342.36	0.11	dif. comp.	5	-68.57	-69.02	1.78	0.0	1.09	1.11	-	2.38	1.97
G342.357+00.113_4	342.36	0.11	dif. comp.	5	-28.97	-	1.6	4.26	1.22	1.26	0.5	2.71	-
G342.478-00.167_0	342.48	-0.17	full. cor.	2	-24.64	-24.84	0.49	11.23	1.08	1.26	0.65	1.43	1.29

Table 5. continued.

Filament ID	ℓ °	b °	Status	N_c	$v_{lsr}(^{13}CO)$ km s^{-1}	$v_{lsr}(C^{18}O)$ km s^{-1}	$\sigma(v_{^{13}CO})$ km s^{-1}	$\sigma(v_{C^{18}O})$ km s^{-1}	σ_v km s^{-1}	$\sigma_v(^{13}CO)$ km s^{-1}	$\sigma_v(C^{18}O)$ km s^{-1}	$\sigma_{v,t}(^{13}CO)$ km s^{-1}	$\sigma_{v,t}(C^{18}O)$ km s^{-1}
G342.478-00.167_1	342.48	-0.17	full. cor.	2	-19.66	-	0.56	0.0	0.8	0.83	-	1.03	-
G342.823+00.129_0	342.82	0.13	full. cor.	1	-24.46	-26.87	0.86	0.0	0.92	0.94	-	1.97	-
G343.579-00.170_0	343.58	-0.17	full. cor.	1	-27.53	-26.86	0.38	11.41	0.95	1.04	0.52	1.64	0.96
G343.776-00.149_0	343.78	-0.15	full. cor.	1	-26.74	-26.29	2.26	13.13	1.12	1.62	0.79	3.32	3.12
G343.908+00.113_0	343.91	0.11	part. cor.	1	9.4	9.23	1.1	1.24	1.28	1.32	0.6	1.77	1.73
G343.998-00.143_0	344.0	-0.14	part. cor.	1	-21.73	-22.73	0.28	0.0	0.96	0.99	-	1.69	1.1
G344.043-00.373_0	344.04	-0.37	full. cor.	1	-87.92	-87.77	0.6	43.91	0.93	1.13	0.63	1.34	0.97
G344.340-00.227_0	344.34	-0.23	full. cor.	1	-85.75	-85.8	1.07	42.56	0.89	1.05	0.53	1.54	1.12
G344.447-00.186_0	344.45	-0.19	part. cor.	2	-86.35	-86.15	0.26	40.63	0.67	0.85	0.54	0.94	0.85
G344.447-00.186_1	344.45	-0.19	part. cor.	2	-46.42	-	0.59	0.0	0.75	0.78	-	1.87	-
G344.592-00.026_0	344.59	-0.03	part. cor.	1	-1.71	-1.87	0.39	0.3	1.55	1.63	1.18	2.03	1.73
G345.345-00.060_0	345.34	-0.06	full. cor.	2	-18.04	-18.51	0.37	0.0	0.89	0.91	-	1.48	1.95
G345.345-00.060_1	345.34	-0.06	part. cor.	2	-1.14	-0.0	0.32	0.0	0.83	0.86	-	1.31	-
G345.433-00.143_0	345.43	-0.14	full. cor.	1	-16.2	-16.37	0.96	7.58	1.13	1.37	0.76	1.71	1.55
G345.493+00.337_0	345.49	0.34	full. cor.	1	-16.89	-16.69	0.74	5.03	1.3	1.9	1.14	2.32	1.71
G345.635+00.358_0	345.64	0.36	full. cor.	1	-16.3	-16.6	0.77	8.13	1.65	2.09	0.83	2.49	2.33
G345.873+00.292_0	345.87	0.29	full. cor.	1	-15.2	-14.97	0.76	3.32	1.35	1.45	0.4	1.95	1.34
G345.879+00.021_0	345.88	0.02	part. cor.	3	-114.93	-115.01	0.62	53.56	0.7	0.93	0.59	1.12	1.11
G345.879+00.021_1	345.88	0.02	part. cor.	3	-80.76	-80.65	1.17	29.49	1.18	1.38	0.73	2.11	1.39
G345.879+00.021_2	345.88	0.02	part. cor.	3	-4.57	-4.35	0.82	1.05	1.46	1.53	1.0	2.86	2.79
G346.177+00.029_0	346.18	0.03	part. cor.	4	-77.21	-77.42	0.47	13.18	1.09	1.14	0.66	1.34	1.47
G346.177+00.029_1	346.18	0.03	part. cor.	4	-89.45	-	0.66	0.0	1.37	1.38	-	1.8	-
G346.177+00.029_2	346.18	0.03	part. cor.	4	-12.45	-	1.15	1.77	1.15	1.16	0.84	1.97	-
G346.177+00.029_3	346.18	0.03	dif. comp.	4	-99.71	-98.15	0.62	0.0	1.17	1.19	-	2.24	0.55
G346.293+00.109_0	346.29	0.11	part. cor.	3	-97.88	-97.6	0.33	48.32	1.09	1.32	0.87	1.47	1.22
G346.293+00.109_1	346.29	0.11	dif. comp.	3	-34.04	-34.29	0.83	6.41	1.14	1.22	0.51	1.57	1.64
G346.293+00.109_2	346.29	0.11	part. cor.	3	-28.13	-28.12	0.34	11.88	0.65	0.78	0.59	0.91	0.89
G346.483+00.144_0	346.48	0.14	part. cor.	1	-8.89	-8.45	0.62	3.97	1.55	1.73	1.1	1.93	1.47
G346.951-00.155_0	346.95	-0.16	part. cor.	3	-82.94	-82.55	0.61	13.7	1.01	1.07	0.51	1.31	1.45
G346.951-00.155_1	346.95	-0.16	part. cor.	3	-76.65	-77.93	1.34	0.0	1.37	1.39	-	2.06	1.77
G346.951-00.155_2	346.95	-0.16	part. cor.	3	-70.55	-70.32	0.62	0.0	1.03	1.05	-	1.46	1.19
G347.216+00.026_0	347.22	0.03	full. cor.	1	-70.43	-70.53	1.22	35.11	2.22	2.57	1.05	3.41	2.7
G347.390+00.266_0	347.39	0.27	part. cor.	3	-91.67	-92.15	1.94	0.0	1.56	1.57	-	2.76	2.65
G347.390+00.266_1	347.39	0.27	part. cor.	3	-81.8	-82.03	1.33	17.71	1.39	1.44	0.79	2.23	2.23
G347.390+00.266_2	347.39	0.27	dif. comp.	3	-64.12	-	0.22	0.0	0.85	0.88	-	1.27	-
G347.870-00.318_0	347.87	-0.32	full. cor.	1	-94.39	-93.95	0.97	43.66	1.11	1.62	0.83	2.06	1.2
G347.894+00.035_0	347.89	0.03	part. cor.	2	-28.62	-	1.53	9.86	1.39	1.52	1.29	2.71	-
G347.894+00.035_1	347.89	0.03	dif. comp.	2	-77.96	-76.9	3.62	0.0	1.2	1.21	-	3.8	4.88
G348.034+00.439_0	348.03	0.44	full. cor.	1	-8.4	-7.35	0.4	1.32	1.22	1.26	0.49	1.47	1.08
G348.232+00.462_0	348.23	0.46	full. cor.	1	-7.4	-7.23	0.44	2.49	1.14	1.62	0.75	1.77	1.14
G348.492+00.346_0	348.49	0.35	part. cor.	2	-62.67	-62.06	0.94	25.79	1.44	1.69	0.78	2.16	-
G348.492+00.346_1	348.49	0.35	full. cor.	2	-8.3	-7.51	0.37	0.0	1.06	1.08	-	1.27	-
G349.876+00.099_0	349.88	0.1	part. cor.	3	-61.44	-61.14	1.05	12.67	1.56	1.65	0.66	2.48	2.09

Table 5. continued.

Filament ID	ℓ °	b °	Status	N_c	$v_{lsr}(^{13}CO)$ km s^{-1}	$v_{lsr}(C^{18}O)$ km s^{-1}	$\sigma(v_{^{13}CO})$ km s^{-1}	$\sigma(v_{C^{18}O})$ km s^{-1}	σ_v km s^{-1}	$\sigma_v(^{13}CO)$ km s^{-1}	$\sigma_v(C^{18}O)$ km s^{-1}	$\sigma_{v,t}(^{13}CO)$ km s^{-1}	$\sigma_{v,t}(C^{18}O)$ km s^{-1}
G349.876+00.099_1	349.88	0.1	part. cor.	3	-108.2	-109.39	1.22	36.54	1.46	1.6	0.89	2.57	-
G349.876+00.099_2	349.88	0.1	dif. comp.	3	16.35	-	3.35	0.0	1.18	1.2	-	3.89	-
G350.299+00.237_0	350.3	0.24	part. cor.	1	-40.01	-41.35	2.23	0.0	2.11	2.12	-	5.18	5.79
G350.522-00.255_0	350.52	-0.25	full. cor.	1	-21.65	-21.81	0.59	10.75	1.56	1.84	0.79	2.1	0.99
G350.781+00.492_0	350.78	0.49	full. cor.	1	-1.63	-1.16	0.41	0.78	0.7	0.9	0.56	1.01	-
G351.022-00.343_0	351.02	-0.34	full. cor.	1	-17.49	-17.08	0.46	7.33	0.97	1.52	0.83	1.9	1.34
G351.498+00.254_0	351.5	0.25	full. cor.	1	-44.11	-43.79	1.39	0.0	1.43	1.44	-	2.29	2.14
G351.731+00.446_0	351.73	0.45	part. cor.	1	-3.26	-	0.37	0.0	0.9	0.93	-	1.01	-
G351.928-00.245_0	351.93	-0.25	part. cor.	2	-22.41	-23.15	0.61	3.8	1.22	1.26	0.7	1.91	1.71
G351.928-00.245_1	351.93	-0.25	full. cor.	2	-11.97	-12.35	0.6	5.15	1.52	1.67	0.69	2.3	2.0
G352.030+00.069_0	352.03	0.07	full. cor.	1	-4.55	-5.09	0.48	2.3	0.74	1.15	0.44	1.54	1.07
G352.062-00.257_0	352.06	-0.26	full. cor.	1	-11.32	-11.05	0.57	5.58	1.2	1.46	0.94	1.93	1.13
G352.107+00.184_0	352.11	0.18	full. cor.	3	-55.9	-56.53	1.54	25.79	1.57	1.83	1.27	3.09	2.5
G352.107+00.184_1	352.11	0.18	dif. comp.	3	-43.83	-41.95	0.86	0.0	1.63	1.64	-	2.44	1.64
G352.107+00.184_2	352.11	0.18	dif. comp.	3	-37.3	-	0.18	0.0	0.8	0.82	-	1.05	-
G352.208+00.354_0	352.21	0.35	full. cor.	1	-1.16	-1.14	0.23	0.44	0.6	0.78	0.56	0.8	0.54
G352.308-00.447_0	352.31	-0.45	full. cor.	1	-12.21	-11.86	1.3	5.94	1.19	1.67	0.98	2.4	2.1
G352.781-00.050_0	352.78	-0.05	part. cor.	1	-44.87	-44.61	0.79	0.0	1.02	1.04	-	1.74	1.34
G352.883+00.464_0	352.88	0.46	full. cor.	1	-4.11	-4.36	0.62	1.66	1.62	1.72	0.8	1.98	1.68
G353.201-00.242_0	353.2	-0.24	full. cor.	1	-17.4	-17.35	0.37	7.3	0.76	1.25	0.61	1.49	0.94
G353.294+00.312_0	353.29	0.31	part. cor.	3	-1.09	-1.12	0.35	0.06	0.77	0.83	0.35	0.89	0.34
G353.294+00.312_1	353.29	0.31	part. cor.	3	-21.94	-22.1	0.35	0.0	0.95	0.97	-	1.11	1.32
G353.294+00.312_2	353.29	0.31	part. cor.	3	-17.05	-16.38	0.48	0.0	1.03	1.06	-	1.35	1.25
G353.389-00.340_0	353.39	-0.34	full. cor.	1	-16.95	-17.21	0.79	8.51	1.44	1.79	1.24	2.31	1.93
G353.418-00.208_0	353.42	-0.21	full. cor.	1	-82.43	-82.46	0.76	35.73	1.2	1.33	0.75	1.77	1.61
G353.477-00.160_0	353.48	-0.16	full. cor.	1	-16.29	-16.46	0.18	5.59	0.97	1.02	0.66	1.02	-
G353.564-00.464_0	353.56	-0.46	full. cor.	1	-17.01	-16.5	0.44	3.14	0.88	1.59	0.71	1.86	0.55
G353.949+00.252_0	353.95	0.25	full. cor.	1	2.78	3.21	0.33	1.46	1.01	1.25	0.61	1.51	1.05
G353.992+00.321_0	353.99	0.32	full. cor.	1	2.63	3.17	0.6	1.18	0.93	0.95	0.54	1.62	1.22
G354.991+00.421_0	354.99	0.42	part. cor.	1	96.9	95.75	2.87	0.0	2.09	2.1	-	6.2	4.75
G355.211-00.496_0	355.21	-0.5	full. cor.	1	-4.15	-4.86	0.5	2.56	1.24	1.53	0.64	1.91	1.04
G355.257-00.260_0	355.26	-0.26	full. cor.	1	-2.23	-2.09	0.46	0.67	1.15	1.65	0.93	2.02	1.43
G355.265+00.339_0	355.26	0.34	part. cor.	3	55.68	53.86	3.52	0.0	2.15	2.16	-	4.42	3.03
G355.265+00.339_1	355.26	0.34	dif. comp.	3	103.08	103.15	1.3	0.0	0.94	0.96	-	2.47	2.71
G355.265+00.339_2	355.26	0.34	dif. comp.	3	71.21	-	1.64	7.5	1.35	1.41	0.52	2.22	-
G355.564+00.279_0	355.56	0.28	full. cor.	2	-80.75	-80.53	1.06	18.57	0.84	0.9	0.48	2.23	2.69
G355.564+00.279_1	355.56	0.28	part. cor.	2	111.01	-	0.9	0.0	1.16	1.18	-	1.55	-
G355.619-00.049_0	355.62	-0.05	full. cor.	1	-19.78	-19.76	0.72	6.01	1.48	1.54	0.97	2.18	2.09
G355.635+00.302_0	355.64	0.3	part. cor.	2	111.26	111.0	0.38	17.32	0.95	0.97	0.51	1.22	1.12
G355.635+00.302_1	355.64	0.3	part. cor.	2	-71.54	-70.29	0.47	11.17	1.02	1.09	0.54	1.78	-
G355.673+00.089_0	355.67	0.09	full. cor.	2	4.15	4.17	0.42	0.91	0.83	0.86	0.71	1.23	0.95
G355.673+00.089_1	355.67	0.09	part. cor.	2	-72.38	-71.63	0.71	0.0	1.41	1.43	-	2.54	1.61
G355.742-00.252_0	355.74	-0.25	full. cor.	2	-24.6	-24.33	1.11	11.95	1.15	1.4	0.96	2.26	2.33

Table 5. continued.

Filament ID	ℓ °	b °	Status	N_c	$v_{lsr}(^{13}CO)$ km s^{-1}	$v_{lsr}(C^{18}O)$ km s^{-1}	$\sigma(v_{^{13}CO})$ km s^{-1}	$\sigma(v_{C^{18}O})$ km s^{-1}	σ_v km s^{-1}	$\sigma_v(^{13}CO)$ km s^{-1}	$\sigma_v(C^{18}O)$ km s^{-1}	$\sigma_{v,t}(^{13}CO)$ km s^{-1}	$\sigma_{v,t}(C^{18}O)$ km s^{-1}
G355.742-00.252_1	355.74	-0.25	part. cor.	2	4.16	3.92	0.28	0.0	0.77	0.8	-	0.93	1.03
G355.743+00.135_0	355.74	0.13	part. cor.	1	17.33	16.61	0.86	2.36	1.38	1.4	0.4	2.38	-
G355.836+00.317_0	355.84	0.32	part. cor.	1	-3.19	-3.05	0.47	0.35	0.85	0.93	0.44	1.59	1.39
G355.991-00.414_0	355.99	-0.41	full. cor.	1	-0.87	-1.12	0.39	0.37	0.75	1.05	0.72	1.15	0.73
G356.416+00.088_0	356.42	0.09	full. cor.	1	-5.4	-5.38	1.03	2.93	0.97	1.22	0.64	1.91	1.78
G356.495+00.198_0	356.5	0.2	full. cor.	1	-4.83	-4.34	0.53	1.48	0.91	1.04	0.59	1.24	0.54
G356.874-00.021_0	356.87	-0.02	full. cor.	1	-9.04	-8.92	0.92	4.22	1.14	1.31	0.61	1.87	1.8
G357.033+00.193_0	357.03	0.19	full. cor.	1	-7.97	-7.8	0.42	1.36	0.95	0.98	0.77	1.24	0.96
G357.420+00.356_0	357.42	0.36	full. cor.	1	-13.92	-13.68	0.41	0.0	0.9	0.92	-	1.07	0.69
G357.637-00.325_0	357.64	-0.33	part. cor.	3	-11.44	-10.94	1.29	0.87	1.13	1.16	0.62	2.29	2.1
G357.637-00.325_1	357.64	-0.33	dif. comp.	3	-2.97	-	0.72	0.39	0.96	1.05	0.8	1.64	-
G357.637-00.325_2	357.64	-0.33	full. cor.	3	4.38	5.09	0.7	2.27	1.38	1.73	0.9	1.81	-
G357.956-00.160_0	357.96	-0.16	part. cor.	2	-6.28	-6.29	1.22	2.14	1.83	2.12	1.21	2.81	1.65
G357.956-00.160_1	357.96	-0.16	part. cor.	2	8.12	10.18	0.63	2.95	1.09	1.37	0.56	2.12	-
G358.017-00.041_0	358.02	-0.04	full. cor.	2	9.06	8.9	1.41	3.34	1.31	1.55	0.67	2.64	2.63
G358.017-00.041_1	358.02	-0.04	part. cor.	2	-136.3	-	0.59	0.0	1.25	1.27	-	1.69	-
G358.101-00.128_0	358.1	-0.13	dif. comp.	2	-3.7	-4.18	1.09	0.83	0.94	1.03	0.71	2.18	1.47
G358.101-00.128_1	358.1	-0.13	full. cor.	2	8.11	8.4	0.73	3.4	1.42	2.09	0.92	2.31	1.91
G358.243-00.425_0	358.24	-0.43	full. cor.	2	4.25	4.43	0.93	1.49	0.91	1.41	0.86	1.77	1.32
G358.243-00.425_1	358.24	-0.43	part. cor.	2	-6.65	-6.15	0.41	0.0	1.15	1.17	-	1.69	1.83
G358.245+00.010_0	358.24	0.01	part. cor.	1	-34.78	-34.26	2.96	0.0	1.88	1.89	-	4.04	4.1
G358.377-00.211_0	358.38	-0.21	full. cor.	2	-0.57	-	1.52	0.54	1.41	1.43	0.31	2.68	-
G358.377-00.211_1	358.38	-0.21	part. cor.	2	-48.28	-50.27	2.56	10.28	2.97	3.13	0.77	5.03	5.14
G358.451-00.422_0	358.45	-0.42	full. cor.	3	-4.24	-4.34	0.63	2.04	1.19	1.57	1.14	1.95	1.67
G358.451-00.422_1	358.45	-0.42	part. cor.	3	6.17	6.23	0.46	2.93	0.8	1.14	0.77	1.52	1.54
G358.451-00.422_2	358.45	-0.42	dif. comp.	3	16.18	16.27	0.74	3.54	0.89	0.99	0.62	1.29	1.56
G359.232+00.329_0	359.23	0.33	part. cor.	1	0.68	0.17	0.34	0.0	0.84	0.87	-	1.03	-
G359.372-00.437_0	359.37	-0.44	full. cor.	1	14.28	14.26	0.26	4.9	0.6	0.98	0.48	1.07	0.43
G359.404+00.308_0	359.4	0.31	full. cor.	2	6.66	6.95	1.22	2.41	1.03	1.17	0.56	2.23	1.7
G359.404+00.308_1	359.4	0.31	dif. comp.	2	16.61	16.69	0.67	0.0	0.82	0.84	-	1.24	1.95
G359.564-00.451_0	359.56	-0.45	full. cor.	1	13.33	13.28	0.41	6.12	0.96	1.14	0.68	1.44	0.53
G359.863-00.248_0	359.86	-0.25	dif. comp.	3	-2.43	-	2.2	0.0	1.86	1.87	-	3.36	-
G359.863-00.248_1	359.86	-0.25	part. cor.	3	17.28	16.35	2.47	7.53	1.38	1.55	0.62	3.34	-
G359.863-00.248_2	359.86	-0.25	dif. comp.	3	-127.04	-130.57	2.86	0.0	2.16	2.17	-	6.06	6.46
G359.896-00.316_0	359.9	-0.32	full. cor.	1	16.16	16.32	0.6	7.12	1.04	1.4	0.79	1.78	1.53

Table 6. tbd

Filament ID	d kpc	l °	$l(d)$ pc	M(ATG) $M_\odot$	M(ATG + P) $M_\odot$	M(dust) $M_\odot$	M(gas) $M_\odot$	$m_{\rm crit,nt}$ $M_\odot\,pc^{-1}$	$m_{\rm obs}$ $M_\odot\,pc^{-1}$	det. ^{13}CO	det. C^{18}O	edge flag	d flag
G000.615-00.448_0	-	-	0.11	-	-	-	-	-	351	1.0	0.28	0	0
G000.675+00.310_0	-	-	0.03	-	-	-	-	-	1397	0.18	0.0	0	0
G000.914+00.308_0	-	-	0.04	-	-	-	-	-	1769	0.25	0.0	0	0
G001.717+00.359_0	-	-	0.03	-	-	-	-	-	312	0.12	0.03	0	0
G001.717+00.359_1	-	-	0.06	-	-	-	-	-	459	0.18	0.02	0	0
G001.717+00.359_2	-	-	0.06	-	-	-	-	-	1410	0.22	0.0	0	0
G002.128+00.295_0	-	-	0.06	-	-	-	-	-	613	1.0	0.19	0	0
G002.210-00.049_0	-	-	0.04	-	-	-	-	-	3576	0.5	0.0	0	0
G002.210-00.049_1	-	-	0.04	-	-	-	-	-	1397	0.46	0.0	0	0
G002.370+00.069_0	-	-	0.02	-	-	-	-	-	307	0.19	0.0	0	0
G002.370+00.069_1	-	-	0.12	-	-	-	-	-	900	0.88	0.02	0	0
G002.370+00.069_2	-	-	0.05	-	-	-	-	-	466	0.4	0.0	0	0
G002.420+00.205_0	-	-	0.04	-	-	-	-	-	405	0.5	0.14	0	0
G002.476-00.120_0	-	-	0.06	-	-	-	-	-	824	0.45	0.0	0	0
G002.476-00.120_1	-	-	0.03	-	-	-	-	-	435	0.22	0.0	0	0
G002.585-00.000_0	-	-	0.06	-	-	-	-	-	613	0.56	0.08	0	0
G002.585-00.000_1	-	-	0.03	-	-	-	-	-	912	0.31	0.0	0	0
G002.687+00.106_0	-	-	0.14	-	-	-	-	-	752	0.98	0.68	0	0
G003.321-00.097_0	-	-	0.07	-	-	-	-	-	768	0.31	0.02	0	0
G003.321-00.097_1	-	-	0.1	-	-	-	-	-	863	0.36	0.12	0	0
G003.387+00.185_0	-	-	0.08	-	-	-	-	-	1811	0.22	0.0	0	0
G003.446-00.223_0	-	-	0.03	-	-	-	-	-	439	0.25	0.0	0	0
G003.456+00.006_0	-	-	0.12	-	-	-	-	-	535	0.62	0.18	0	0
G004.180-00.010_0	-	-	0.08	-	-	-	-	-	244	0.32	0.06	0	0
G004.180-00.010_1	-	-	0.16	-	-	-	-	-	767	0.7	0.05	0	0
G004.180-00.010_2	-	-	0.09	-	-	-	-	-	474	0.4	0.13	0	0
G004.583-00.109_0	-	-	0.11	-	-	-	-	-	695	0.69	0.09	0	0
G004.583-00.109_1	-	-	0.13	-	-	-	-	-	825	0.79	0.0	0	0
G004.705+00.001_0	-	-	0.08	-	-	-	-	-	1423	1.0	0.5	0	0
G004.711-00.440_0	-	-	0.09	-	-	-	-	-	252	0.86	0.08	0	0
G004.794-00.284_0	2.9	3.07	0.06	299	5649	1065	894	291	274	0.49	0.0	0	2
G004.794-00.284_1	2.9	3.05	0.06	334	8754	1505	834	274	533	0.47	0.0	0	2
G004.950-00.076_0	2.9	2.57	0.05	280	6760	914	1774	689	619	0.83	0.08	0	2
G005.101-00.104_0	10.8	40.51	0.21	18402	76880	24043	25629	633	551	0.71	0.14	0	1
G005.357+00.101_0	2.9	5.28	0.1	720	7662	1461	4799	908	283	1.0	0.58	0	1
G005.454+00.167_0	2.9	2.77	0.05	214	3816	564	1082	391	572	1.0	0.0	0	2
G005.704-00.306_0	3.0	3.47	0.07	254	5603	954	2577	742	771	1.0	0.0	0	2
G005.912+00.283_0	-	-	0.04	-	-	-	-	-	1102	0.27	0.0	0	0
G005.930-00.095_0	3.0	1.72	0.03	348	4573	955	1018	592	246	0.43	0.07	0	2
G006.589-00.106_0	3.0	2.38	0.05	6187	27235	9665	1322	556	610	0.14	0.01	0	1
G006.589-00.106_1	3.0	10.98	0.21	6619	43684	12875	7499	683	1377	0.64	0.12	0	1
G006.849+00.151_0	3.0	1.93	0.04	536	6399	1717	891	462	521	0.42	0.0	0	2
G006.849+00.151_1	-	-	0.02	-	-	-	-	-	608	0.33	0.0	0	0

Table 6. continued.

Filament ID	d kpc	l °	$l(d)$ pc	M(ATG) $M_\odot$	M(ATG + P) $M_\odot$	M(dust) $M_\odot$	M(gas) $M_\odot$	$m_{\rm crit,nt}$ $M_\odot\,pc^{-1}$	$m_{\rm obs}$ $M_\odot\,pc^{-1}$	det. ^{13}CO	det. C^{18}O	edge flag	d flag
G007.250-00.120_0	3.0	2.8	0.05	2220	10619	3372	1176	420	366	0.32	0.02	0	1
G007.250-00.120_1	3.0	5.73	0.11	2455	15984	4343	3392	591	508	0.68	0.25	0	1
G008.000-00.272_0	10.9	17.26	0.09	15870	33100	16262	30342	1758	493	1.0	0.73	0	1
G008.255+00.165_0	3.0	7.05	0.13	1535	11756	4903	8897	1262	314	1.0	0.88	0	1
G008.800-00.359_0	4.4	17.07	0.22	2380	27776	9217	14098	826	640	1.0	0.39	0	1
G008.800-00.359_1	3.1	7.3	0.14	1197	14241	4700	2971	407	356	0.63	0.16	0	1
G008.914-00.318_0	4.4	13.36	0.17	2049	18719	4839	12420	929	539	1.0	0.39	0	1
G009.230+00.157_0	3.1	5.05	0.09	567	5528	1336	3958	784	246	1.0	0.77	0	1
G009.280-00.152_0	4.7	5.28	0.06	1579	9755	3464	6130	1161	274	1.0	0.8	0	1
G009.970-00.024_0	3.5	6.88	0.11	1593	16507	2535	2512	365	603	0.78	0.24	0	1
G009.970-00.024_1	3.5	4.09	0.07	1572	15282	2418	1327	325	698	0.42	0.0	0	2
G009.970-00.024_2	3.5	1.87	0.03	1446	8604	1822	530	283	228	0.22	0.0	0	2
G010.531-00.024_0	8.5	17.54	0.12	4360	48903	9008	14489	826	1103	0.98	0.07	0	1
G010.682-00.161_0	2.9	14.04	0.28	3783	49461	13992	16062	1144	1418	1.0	0.34	0	1
G010.682-00.161_1	5.0	2.87	0.03	6010	45787	15349	896	312	442	0.11	0.0	0	1
G010.682-00.161_2	5.0	6.38	0.07	6275	51055	16800	2768	434	462	0.28	0.12	0	1
G010.682-00.161_3	5.0	4.28	0.05	5752	40890	13982	1653	386	360	0.18	0.0	0	2
G010.694+00.034_0	2.9	4.17	0.08	2733	31686	11257	2765	663	885	0.38	0.07	0	1
G010.694+00.034_1	2.9	10.06	0.2	3143	52917	18674	15780	1569	2573	0.97	0.09	0	1
G010.694+00.034_2	2.9	1.96	0.04	2087	19936	7256	594	304	458	0.19	0.0	0	1
G010.809-00.393_0	5.0	6.41	0.07	1465	14267	2872	4020	627	816	0.81	0.09	0	1
G010.809-00.393_1	2.9	3.2	0.06	537	6408	1199	1139	356	468	0.66	0.0	0	2
G010.878-00.468_0	2.9	5.68	0.11	965	16112	1932	3742	659	999	0.66	0.08	0	2
G010.878-00.468_1	5.0	7.26	0.08	2188	22926	3565	3806	525	701	0.41	0.06	0	2
G010.971-00.363_0	5.0	12.07	0.14	4626	25295	6767	9341	774	833	0.92	0.06	0	1
G010.971-00.363_1	2.9	6.99	0.14	1727	17290	3306	4049	579	1230	0.92	0.0	0	2
G011.046-00.069_0	2.9	1.81	0.04	8349	49178	15981	774	427	557	0.05	0.0	0	1
G011.046-00.069_1	2.9	8.73	0.17	8704	61658	18562	4090	468	740	0.24	0.05	0	1
G011.046-00.069_2	2.9	27.35	0.54	8411	51454	16451	12878	471	543	0.76	0.28	0	1
G011.612-00.383_0	3.0	3.81	0.07	401	10230	1759	2999	788	1579	1.0	0.0	0	2
G012.405-00.138_0	2.6	9.43	0.21	807	18099	3927	7804	827	622	0.97	0.12	0	1
G012.405-00.138_1	8.7	4.82	0.03	4563	38064	10563	1727	358	329	0.15	0.0	0	2
G012.529-00.314_0	2.6	8.14	0.18	1177	13178	3543	5601	688	561	0.88	0.2	0	1
G012.529-00.314_1	2.6	3.0	0.07	964	7160	2163	754	251	174	0.33	0.0	0	1
G012.529-00.314_2	1.3	1.88	0.08	404	7353	1799	479	254	741	0.39	0.0	0	2
G012.543+00.011_0	12.0	17.74	0.08	6570	46716	9427	7198	406	776	0.84	0.03	0	1
G012.543+00.011_1	12.0	6.6	0.03	5071	28427	6550	2752	417	316	0.34	0.0	0	1
G012.543-00.092_0	2.6	3.25	0.07	832	19478	4223	2541	782	734	0.36	0.0	0	2
G012.543-00.092_1	4.8	14.84	0.18	2500	38102	8831	8142	548	767	0.81	0.01	0	2
G012.543-00.092_2	2.6	2.62	0.06	791	16469	3602	585	223	543	0.28	0.0	0	1
G012.595+00.116_0	4.8	4.59	0.05	1104	12478	2920	1830	398	382	0.49	0.13	0	2
G012.893+00.496_0	2.5	5.3	0.12	3616	8374	4483	5040	951	446	1.0	0.93	1	1
G012.893+00.496_1	1.8	3.82	0.12	1882	4842	2428	2129	558	367	1.0	0.0	1	1

Table 6. continued.

Filament ID	d kpc	l °	$l(d)$ pc	M(ATG) $M_\odot$	M(ATG + P) $M_\odot$	M(dust) $M_\odot$	M(gas) $M_\odot$	$m_{\rm crit,nt}$ $M_\odot\,pc^{-1}$	$m_{\rm obs}$ $M_\odot\,pc^{-1}$	det. ^{13}CO	det. C^{18}O	edge flag	d flag
G013.220+00.164_0	2.6	3.56	0.08	305	8704	2115	2463	692	701	1.0	0.0	0	1
G013.220+00.164_1	1.9	1.61	0.05	232	7220	1815	1193	742	702	0.62	0.0	0	2
G013.282-00.316_0	2.6	25.67	0.57	3464	70003	18554	30486	1188	1653	0.99	0.28	0	1
G013.282-00.316_1	1.8	7.51	0.24	2559	51664	14625	8304	1106	2032	0.41	0.04	0	2
G013.313+00.193_0	1.9	10.64	0.32	837	12003	4864	4697	441	355	0.98	0.21	0	1
G013.313+00.193_1	2.6	1.79	0.04	1470	16418	6757	1698	949	346	0.14	0.03	0	2
G013.460+00.171_0	1.9	1.95	0.06	159	4496	1013	1540	789	581	1.0	0.05	0	2
G013.700-00.072_0	4.5	10.55	0.13	3280	22978	5657	8288	786	385	0.76	0.39	0	1
G013.893-00.129_0	3.1	4.22	0.08	1065	20126	3925	12025	2850	918	1.0	0.42	0	2
G013.893-00.129_1	1.8	1.89	0.06	564	11761	2190	854	452	825	0.77	0.27	0	1
G014.005+00.311_0	3.9	6.66	0.1	986	10736	3271	2866	430	647	0.8	0.08	0	1
G014.117-00.392_0	3.1	4.72	0.09	823	13483	1232	4793	1015	1332	0.97	0.16	0	2
G014.117-00.392_1	1.5	2.32	0.09	306	8194	838	2727	1176	1321	1.0	0.0	0	2
G014.627-00.123_0	3.1	7.21	0.13	1268	20376	1537	8135	1128	1136	1.0	0.31	0	1
G014.789-00.478_0	2.0	3.89	0.11	517	8317	2296	2225	572	590	0.93	0.14	1	1
G014.919-00.065_0	2.6	5.81	0.13	1136	15895	4127	3189	549	822	0.71	0.0	0	1
G015.611-00.476_0	1.8	4.27	0.14	1419	5858	2288	2213	519	203	0.83	0.28	1	1
G015.611-00.476_1	16.9	15.26	0.05	41765	89265	50118	9715	637	622	0.32	0.0	1	1
G015.653-00.224_0	11.6	21.58	0.11	4745	17675	6356	11165	517	193	1.0	0.61	0	1
G016.609-00.069_0	4.7	13.28	0.16	8860	39024	13367	9764	735	314	0.39	0.17	0	1
G016.609-00.069_1	3.6	8.78	0.14	5908	39790	11396	2725	310	453	0.38	0.14	0	1
G016.661+00.121_0	1.9	1.75	0.05	149	1804	233	392	224	211	0.65	0.12	0	1
G016.700-00.235_0	4.7	3.39	0.04	1375	15250	2568	1483	437	392	0.33	0.02	0	2
G016.700-00.235_1	3.6	5.38	0.09	973	15778	2275	2089	388	659	0.67	0.0	0	2
G016.757+00.013_0	3.6	5.93	0.09	1327	13873	3523	3840	647	844	0.82	0.03	0	1
G016.919+00.275_0	1.9	8.06	0.24	1576	11469	3421	12341	1532	610	1.0	0.71	0	1
G016.929-00.082_0	3.6	12.03	0.19	2001	15687	3393	4923	409	265	0.82	0.11	0	1
G016.929-00.082_1	15.9	8.63	0.03	23180	102276	29452	8535	990	609	0.14	0.0	0	1
G016.998+00.280_0	1.9	3.88	0.12	1251	9789	3034	10342	2663	836	1.0	0.43	0	2
G301.638-00.239_0	4.8	7.6	0.09	2491	8737	3874	5637	742	450	1.0	0.69	0	1
G305.560-00.003_0	3.8	19.5	0.29	12255	39279	17799	23893	1225	919	0.97	0.65	0	1
G309.161-00.358_0	3.5	6.7	0.11	2896	13887	4116	11882	1774	505	1.0	0.92	0	1
G313.703-00.181_0	3.0	3.61	0.07	1308	9620	2195	5821	1612	526	1.0	0.87	0	1
G313.717+00.103_0	7.5	4.69	0.04	3144	12401	4505	3990	851	281	0.5	0.38	0	1
G313.717+00.103_1	3.0	1.68	0.03	644	3954	1143	506	301	286	0.46	0.0	0	1
G313.717+00.103_2	3.0	2.59	0.05	696	5560	1410	1926	742	314	0.71	0.46	0	1
G314.219+00.266_0	4.2	14.77	0.2	10074	38592	15690	32319	2188	820	1.0	0.75	0	1
G314.284+00.100_0	4.2	9.73	0.13	8443	23633	11840	8855	910	661	1.0	0.24	0	1
G314.284+00.100_1	4.2	9.73	0.13	8611	25278	12335	11649	1198	582	1.0	0.84	0	1
G317.386+00.113_0	2.8	5.21	0.11	3399	18166	7068	13011	2498	995	1.0	0.69	0	1
G317.889-00.256_0	2.3	7.23	0.18	2572	16165	5089	13494	1866	822	1.0	0.69	0	1
G320.240+00.027_0	0.6	0.75	0.07	82	1239	489	163	217	896	1.0	0.54	0	1
G320.243+00.406_0	2.1	6.36	0.17	2297	5753	2966	4051	637	340	0.98	0.41	0	1

Table 6. continued.

Filament ID	d kpc	l °	$l(d)$ pc	M(ATG) $M_\odot$	M(ATG + P) $M_\odot$	M(dust) $M_\odot$	M(gas) $M_\odot$	$m_{\rm crit,nt}$ $M_\odot\,pc^{-1}$	$m_{\rm obs}$ $M_\odot\,pc^{-1}$	det. ^{13}CO	det. C^{18}O	edge flag	d flag
G320.270-00.299_0	8.6	26.37	0.18	37328	74991	44456	55758	2114	854	0.95	0.66	0	1
G320.883-00.392_0	2.8	6.95	0.14	3019	10049	4020	6689	963	348	1.0	0.88	0	1
G323.179+00.149_0	4.0	5.05	0.07	2362	7883	3657	7578	1502	339	1.0	0.74	0	1
G323.929+00.036_0	10.0	29.45	0.17	18472	54410	21140	38513	1308	1344	1.0	0.2	0	1
G326.552+00.165_0	4.4	9.85	0.13	3117	17795	5341	8525	865	885	1.0	0.36	0	1
G326.586+00.050_0	4.6	5.16	0.06	608	9069	1481	2146	416	749	0.95	0.0	0	2
G326.722-00.099_0	3.5	4.39	0.07	991	15912	3946	5068	1155	1419	0.96	0.04	0	1
G326.790-00.119_0	3.5	7.23	0.12	3143	17259	6190	10318	1427	799	1.0	0.6	0	1
G327.036-00.408_0	3.5	4.97	0.08	858	7042	1599	3995	803	578	0.97	0.57	0	1
G327.042-00.169_0	3.5	7.07	0.12	811	17955	3924	9478	1340	1019	1.0	0.19	0	1
G327.157-00.256_0	3.5	36.25	0.59	8940	73455	23085	54139	1494	1200	1.0	0.59	0	1
G327.258-00.420_0	3.0	7.6	0.15	957	15264	3195	9413	1238	671	1.0	0.43	0	2
G327.396+00.452_0	5.0	13.85	0.16	12620	33115	13902	14448	1043	985	0.94	0.3	0	1
G327.870+00.157_0	5.7	12.24	0.12	8511	48707	17401	12673	1035	614	0.61	0.2	0	1
G327.870+00.157_1	3.1	3.38	0.06	2945	22080	7109	1049	311	508	0.31	0.1	0	2
G327.884+00.002_0	7.1	9.24	0.07	1792	19563	4110	6464	700	660	1.0	0.03	0	2
G327.884+00.002_1	3.1	1.71	0.03	384	5793	1097	395	230	304	0.47	0.0	0	2
G327.981-00.101_0	3.1	9.07	0.17	2824	26926	6362	8813	972	1053	1.0	0.59	0	1
G328.627+00.063_0	9.0	6.54	0.04	2574	15397	5281	1576	241	327	0.54	0.0	0	1
G328.627+00.063_1	3.4	2.06	0.03	562	8458	2188	966	469	548	0.54	0.0	0	2
G328.773+00.304_0	6.8	13.27	0.11	3453	27220	4990	9253	697	871	1.0	0.17	0	1
G328.773+00.304_1	9.0	5.04	0.03	3635	18056	4410	959	190	282	0.29	0.0	0	2
G328.940+00.277_0	5.0	4.46	0.05	694	12265	2390	2896	649	937	0.9	0.0	0	2
G330.348-00.122_0	5.8	10.0	0.1	1903	25812	4436	4653	466	956	0.69	0.0	0	1
G330.760-00.306_0	4.0	11.6	0.17	2233	32090	8461	16253	1402	1074	1.0	0.41	0	1
G330.760-00.306_1	4.0	3.95	0.06	1794	18910	5325	1577	399	430	0.37	0.0	0	1
G330.973+00.076_0	2.9	4.45	0.09	901	15132	2872	1021	230	591	0.43	0.06	0	2
G330.973+00.076_1	3.9	5.21	0.08	1561	22150	4404	3221	618	605	0.37	0.01	0	2
G330.973+00.076_2	-	-	0.06	-	-	-	-	-	283	0.27	0.03	0	0
G330.986+00.337_0	3.4	8.25	0.14	1814	10419	2829	3502	425	426	0.98	0.45	0	1
G331.533+00.241_0	3.5	1.96	0.03	1202	15198	4298	933	476	520	0.16	0.0	0	1
G331.533+00.241_1	3.5	6.97	0.11	1228	17574	4824	2887	414	561	0.59	0.19	0	1
G331.533+00.241_2	5.3	6.6	0.07	2635	25796	7781	2702	409	611	0.33	0.03	0	1
G331.670-00.272_0	3.1	8.33	0.15	1469	9835	2860	5407	649	220	0.96	0.85	0	1
G331.670-00.272_1	5.3	3.21	0.03	3743	18969	6237	1018	317	406	0.23	0.0	0	2
G331.670-00.272_2	5.3	9.0	0.1	4154	25715	7726	3600	400	743	0.6	0.0	0	2
G331.973-00.378_0	3.6	11.29	0.18	1370	12687	2512	5068	449	482	0.94	0.42	0	1
G332.000+00.011_0	3.1	8.94	0.17	1691	37862	5996	7211	807	2530	0.94	0.03	0	2
G332.000+00.011_1	5.3	12.02	0.13	1423	35153	4338	4906	408	1194	0.75	0.0	0	2
G332.370-00.080_0	3.1	7.63	0.14	25736	132180	48379	3077	403	464	0.07	0.0	0	1
G332.370-00.080_1	3.1	97.78	1.81	27338	174920	59182	80571	824	665	0.97	0.51	0	1
G332.370-00.080_2	5.2	33.02	0.36	69299	313946	120785	13501	409	772	0.2	0.03	0	1
G332.610+00.052_0	5.6	16.04	0.16	2259	34359	7143	7452	465	735	0.94	0.1	0	1

Table 6. continued.

Filament ID	d kpc	l °	$l(d)$ pc	M(ATG) $M_\odot$	M(ATG + P) $M_\odot$	M(dust) $M_\odot$	M(gas) $M_\odot$	$m_{\rm crit,nt}$ $M_\odot\,pc^{-1}$	$m_{\rm obs}$ $M_\odot\,pc^{-1}$	det. ^{13}CO	det. C^{18}O	edge flag	d flag
G332.852-00.214_0	3.6	6.38	0.1	600	15318	1958	4459	698	879	0.97	0.15	0	2
G333.007+00.452_0	3.6	3.62	0.06	506	9781	1554	1432	396	788	0.49	0.0	0	2
G333.063+00.181_0	3.6	8.59	0.14	1296	28891	4984	5392	628	1762	0.89	0.2	0	1
G333.202-00.250_0	3.6	1.89	0.03	641	12909	881	942	498	455	0.24	0.0	0	2
G333.202-00.250_1	3.6	2.0	0.03	658	14319	937	447	224	618	0.24	0.0	0	2
G333.202-00.250_2	3.6	3.46	0.06	632	12204	853	577	167	371	0.35	0.0	0	2
G333.297+00.073_0	3.6	29.71	0.47	11172	73991	22262	32686	1100	1193	0.99	0.37	0	1
G333.297+00.073_1	10.7	28.87	0.15	63610	196640	82882	20024	694	700	0.33	0.07	0	1
G333.481+00.165_0	8.7	10.61	0.07	4629	15205	5694	2802	264	345	0.86	0.07	0	1
G333.722+00.361_0	2.3	9.56	0.24	3667	11091	4360	5969	624	326	1.0	0.79	0	1
G333.868-00.312_0	3.6	9.64	0.15	1648	43775	13246	34310	3561	2893	1.0	0.35	0	1
G333.899-00.106_0	9.6	19.81	0.12	6419	36293	6610	5634	284	320	0.58	0.04	0	2
G333.899-00.106_1	3.6	3.06	0.05	1770	28740	2546	2772	904	1151	0.23	0.06	0	1
G333.985+00.224_0	5.2	8.64	0.1	3615	23103	8974	2126	246	289	0.34	0.02	0	2
G333.985+00.224_1	3.1	8.3	0.15	1728	17026	6124	2540	306	455	0.53	0.04	0	1
G333.985+00.224_2	3.1	1.93	0.04	1620	13698	5034	296	153	316	0.14	0.0	0	1
G333.985+00.224_3	3.7	10.05	0.16	2370	21204	7728	4137	412	502	0.56	0.06	0	1
G333.985+00.224_4	5.2	4.0	0.04	4153	30656	11549	1364	341	543	0.14	0.0	0	1
G333.992+00.058_0	5.2	23.2	0.26	3852	57212	14491	17355	748	1500	0.96	0.07	0	1
G333.992+00.058_1	3.6	13.97	0.22	1919	30542	7612	5497	394	856	0.82	0.05	0	2
G333.992+00.058_2	4.0	6.13	0.09	2127	25333	6777	2088	341	398	0.33	0.09	0	1
G334.056+00.489_0	3.7	3.85	0.06	362	6554	914	1425	370	1308	0.85	0.0	0	2
G334.070-00.257_0	3.6	4.93	0.08	639	12927	2487	1849	375	444	0.57	0.0	0	2
G334.070-00.257_1	3.1	5.01	0.09	546	14131	2591	1794	358	657	0.65	0.0	0	2
G334.202+00.156_0	9.6	21.65	0.13	7931	61758	19401	15805	730	1572	1.0	0.11	0	1
G334.202+00.156_1	2.8	2.39	0.05	1396	14335	4148	2286	956	877	0.4	0.0	0	2
G334.267-00.107_0	5.2	11.62	0.13	3242	36560	9429	6894	593	698	0.54	0.01	0	1
G334.267-00.107_1	12.8	15.02	0.07	14140	104867	30747	8024	534	795	0.32	0.01	0	1
G334.442+00.050_0	9.7	20.82	0.12	7852	51946	14536	8654	416	349	0.53	0.17	0	1
G334.442+00.050_1	8.7	8.53	0.06	8018	57847	15705	2985	350	644	0.25	0.0	0	2
G334.442+00.050_2	10.8	9.46	0.05	9332	61013	17142	4223	446	434	0.21	0.0	0	2
G334.617-00.270_0	3.1	6.46	0.12	1949	16660	4036	7906	1225	843	1.0	0.52	0	1
G334.640+00.426_0	4.0	20.51	0.29	6301	20543	7171	13038	636	503	0.91	0.32	0	1
G334.684+00.024_0	2.3	6.36	0.16	1450	14495	3268	2063	324	391	0.49	0.05	0	1
G334.684+00.024_1	2.3	1.15	0.03	1334	10857	2641	184	160	217	0.1	0.0	0	1
G334.684+00.024_2	5.1	3.71	0.04	5663	34208	9420	1050	283	330	0.14	0.0	0	1
G334.840-00.196_0	3.1	8.78	0.16	1019	17938	2058	3969	452	570	0.72	0.18	0	1
G334.840-00.196_1	2.3	4.08	0.1	622	13939	1653	861	211	671	0.47	0.0	0	2
G335.008-00.268_0	13.8	30.74	0.13	19077	141611	45245	18720	609	1008	0.47	0.01	0	1
G335.008-00.268_1	13.8	18.95	0.08	16000	114062	36884	13217	697	629	0.29	0.0	0	1
G335.083+00.065_0	-	-	0.05	-	-	-	-	-	589	0.85	0.0	0	0
G335.251-00.033_0	2.9	4.9	0.1	496	7192	1294	2336	476	507	0.97	0.06	0	1
G335.814+00.061_0	9.7	13.02	0.08	3578	34398	6766	5313	408	338	0.36	0.0	0	2

Table 6. continued.

Filament ID	d kpc	l °	$l(d)$ pc	M(ATG) $M_\odot$	M(ATG + P) $M_\odot$	M(dust) $M_\odot$	M(gas) $M_\odot$	$m_{\rm crit,nt}$ $M_\odot\,pc^{-1}$	$m_{\rm obs}$ $M_\odot\,pc^{-1}$	det. ^{13}CO	det. C^{18}O	edge flag	d flag
G336.060+00.040_0	7.6	14.05	0.11	5373	29222	9503	6845	487	470	0.59	0.1	0	1
G336.062-00.271_0	2.9	3.8	0.08	329	5598	1004	1198	316	319	0.69	0.1	0	2
G336.194-00.457_0	5.0	4.97	0.06	306	4538	585	983	198	378	0.95	0.1	0	2
G336.248+00.310_0	10.8	25.59	0.14	16099	84815	28092	14781	578	496	0.3	0.02	0	2
G336.248+00.310_1	3.2	4.98	0.09	2056	20226	5286	2358	473	279	0.21	0.1	0	1
G336.376+00.204_0	12.1	23.97	0.11	10792	59185	16817	12126	506	556	0.42	0.02	0	1
G336.376+00.204_1	10.8	6.03	0.03	9257	52280	14643	2472	410	456	0.14	0.03	0	1
G336.391+00.012_0	6.7	37.36	0.32	25696	97969	35723	27166	727	886	0.7	0.1	0	1
G336.391+00.012_1	2.9	2.06	0.04	5270	26094	8211	1133	551	390	0.08	0.01	0	1
G336.846+00.282_0	4.6	9.79	0.12	3272	21084	6044	4825	493	1002	0.95	0.05	0	1
G336.846+00.282_1	4.3	3.41	0.05	2547	13091	4178	1998	586	413	0.35	0.12	0	1
G337.148-00.387_0	1.6	6.6	0.24	1609	10541	3155	1648	250	276	0.53	0.0	0	1
G337.148-00.387_1	2.8	6.01	0.12	4566	22947	7622	2622	436	374	0.27	0.03	0	1
G337.409-00.400_0	3.0	14.23	0.27	8944	29287	12783	13517	950	499	0.8	0.33	0	1
G337.409-00.400_1	3.7	4.78	0.07	12449	26816	14574	1522	318	251	0.22	0.03	0	1
G337.744-00.346_0	3.0	14.7	0.28	3671	22759	7633	9541	649	476	0.96	0.44	0	1
G337.850+00.087_0	3.5	12.96	0.21	4124	81314	21544	24395	1882	4461	1.0	0.06	0	1
G338.181-00.477_0	2.9	4.41	0.09	715	10061	2684	1710	388	945	0.86	0.11	0	1
G338.279-00.295_0	1.1	1.13	0.06	418	8969	3431	642	566	968	0.59	0.12	0	1
G338.279-00.295_1	7.0	7.25	0.06	2964	23829	4778	3211	443	610	0.59	0.0	0	2
G338.291-00.119_0	5.7	4.12	0.04	1148	17246	2379	1766	429	377	0.36	0.03	0	2
G338.291-00.119_1	7.1	6.15	0.05	1878	31224	4121	3313	539	775	0.44	0.0	0	2
G338.528+00.214_0	2.7	6.39	0.14	1760	15105	4387	2238	351	853	0.65	0.11	0	1
G338.680-00.455_0	2.9	12.3	0.24	1124	14025	2508	4588	373	652	0.95	0.1	0	1
G338.680-00.455_1	2.9	2.73	0.05	1078	11938	2227	540	198	499	0.22	0.01	0	1
G338.708-00.328_0	3.2	7.91	0.14	668	10417	2000	3155	399	525	0.88	0.07	0	2
G338.708-00.328_1	2.9	5.22	0.1	653	11615	2077	1709	328	776	0.66	0.12	0	2
G338.749+00.159_0	2.7	4.15	0.09	830	14933	3270	2425	584	1512	1.0	0.24	0	1
G338.773+00.492_0	4.2	7.52	0.1	3755	19029	7955	17964	2387	1070	1.0	0.7	1	1
G338.806+00.111_0	2.6	6.21	0.14	939	18538	3126	3362	542	1367	0.71	0.07	0	1
G338.941-00.058_0	11.6	15.54	0.08	22161	72798	31414	8379	539	411	0.3	0.05	0	1
G338.941-00.058_1	3.2	10.73	0.19	3170	25865	7320	6992	652	723	0.8	0.4	0	1
G338.953+00.278_0	4.2	6.41	0.09	857	11740	2982	3094	483	320	0.56	0.11	0	2
G338.953+00.278_1	2.2	2.91	0.08	575	10247	2261	1032	355	814	0.46	0.02	0	2
G338.993+00.110_0	2.4	1.99	0.05	214	6310	918	573	288	820	0.79	0.0	0	2
G339.077+00.153_0	4.8	15.19	0.18	4665	34627	10216	8996	592	822	0.67	0.21	0	1
G339.077+00.153_1	2.2	3.37	0.09	1098	12318	3199	1007	299	634	0.33	0.0	0	2
G339.113-00.203_0	7.1	12.56	0.1	4853	55503	19462	13591	1082	906	0.56	0.1	0	2
G339.113-00.203_1	2.9	6.68	0.13	1061	15224	4979	1581	237	507	0.73	0.02	0	2
G339.113-00.203_2	3.1	5.86	0.11	1140	15870	5257	1968	336	469	0.58	0.1	0	1
G339.116-00.405_0	2.9	12.51	0.25	1918	18365	3450	8029	642	529	1.0	0.57	0	1
G339.260+00.117_0	4.8	13.2	0.16	3533	23282	6960	7818	592	599	0.95	0.32	0	1
G339.385-00.414_0	2.9	8.48	0.17	1385	11559	3740	4603	543	486	0.97	0.23	0	1

Table 6. continued.

Filament ID	d kpc	l °	$l(d)$ pc	M(ATG) $M_\odot$	M(ATG + P) $M_\odot$	M(dust) $M_\odot$	M(gas) $M_\odot$	$m_{\rm crit,nt}$ $M_\odot\,pc^{-1}$	$m_{\rm obs}$ $M_\odot\,pc^{-1}$	det. ^{13}CO	det. $C^{18}O$	edge flag	d flag
G339.586-00.119_0	2.6	9.61	0.21	4320	27985	11442	9357	974	809	0.99	0.62	0	1
G339.586-00.119_1	13.2	15.72	0.07	56501	127084	77114	7884	502	591	0.32	0.01	0	1
G339.692+00.291_0	10.0	8.15	0.05	2794	21031	6418	6317	775	612	0.57	0.13	0	1
G339.988-00.165_0	3.6	10.84	0.17	2007	26026	7685	12737	1175	778	1.0	0.6	0	1
G339.988-00.165_1	2.8	3.34	0.07	1101	11687	3624	828	248	363	0.38	0.02	0	1
G340.301-00.387_0	3.6	31.82	0.51	20468	85311	34770	62867	1976	1176	0.95	0.69	0	1
G340.301-00.387_1	7.9	27.05	0.2	68757	153410	84425	9723	359	618	0.37	0.0	0	2
G340.301-00.387_2	10.1	20.49	0.12	89615	185554	106355	10079	492	501	0.21	0.0	0	2
G340.316+00.079_0	7.9	10.8	0.08	2040	23973	3674	6145	569	342	0.69	0.33	0	2
G340.316+00.079_1	-	-	0.05	-	-	-	-	-	537	0.38	0.0	0	0
G340.482-00.306_0	10.2	8.94	0.05	4905	23156	4087	7625	853	344	0.46	0.29	0	2
G340.482-00.306_1	3.6	6.05	0.1	1032	15540	890	3636	601	1485	0.89	0.0	0	1
G340.482-00.306_2	3.6	4.89	0.08	933	10792	755	1967	403	682	0.71	0.09	0	1
G340.511-00.471_0	3.6	5.09	0.08	1003	17777	3530	10213	2005	1612	1.0	0.18	1	1
G340.630-00.093_0	9.6	10.38	0.06	1482	12983	2507	3011	290	370	1.0	0.0	0	2
G340.630-00.093_1	3.6	3.65	0.06	472	12461	1591	2201	604	1388	0.91	0.0	0	2
G340.630-00.093_2	3.6	3.13	0.05	468	12173	1564	2370	758	1297	0.82	0.0	0	2
G340.981-00.013_0	3.3	9.21	0.16	812	16660	3492	3122	339	564	0.82	0.0	0	1
G340.981-00.013_1	3.3	6.32	0.11	757	12716	2815	1352	214	298	0.57	0.1	0	1
G340.981-00.013_2	3.3	3.15	0.05	786	14595	3144	1031	327	420	0.28	0.01	0	1
G340.981-00.013_3	2.2	2.38	0.06	416	11523	2231	450	189	558	0.29	0.0	0	2
G341.244-00.265_0	3.3	28.23	0.49	14242	74596	28981	49166	1741	895	1.0	0.79	0	1
G341.415+00.244_0	2.2	2.77	0.07	239	4833	736	1281	463	490	1.0	0.11	0	2
G341.415+00.244_1	2.2	2.72	0.07	420	10471	1730	3015	1110	1654	0.96	0.0	0	2
G341.415+00.244_2	10.8	8.04	0.04	2518	14184	3705	2526	314	327	0.56	0.04	0	2
G341.674+00.184_0	14.0	14.77	0.06	5453	48378	14825	10009	678	674	0.5	0.13	0	2
G341.674+00.184_1	5.0	6.78	0.08	894	15058	4072	2067	305	528	0.61	0.0	0	1
G341.938+00.054_0	8.0	17.36	0.12	4054	29276	7358	5535	319	342	0.69	0.06	0	1
G341.938+00.054_1	2.0	1.67	0.05	398	7344	1308	561	337	340	0.28	0.0	0	2
G342.100+00.399_0	7.7	33.61	0.25	47791	143249	60722	25252	751	380	0.39	0.22	0	1
G342.100+00.399_1	10.9	10.6	0.06	52561	134087	62627	3308	312	203	0.08	0.0	0	1
G342.100+00.399_2	10.9	49.87	0.26	80893	223829	99440	23705	475	634	0.4	0.04	0	1
G342.100+00.399_3	10.9	70.18	0.37	94022	278989	118953	79406	1131	813	0.55	0.28	0	1
G342.100+00.399_4	2.3	12.25	0.31	5780	30924	9648	3876	316	518	0.46	0.03	0	1
G342.100+00.399_5	12.5	14.95	0.07	77227	198714	92312	5964	399	398	0.09	0.0	0	2
G342.100+00.399_6	2.3	1.72	0.04	4886	16464	6539	309	179	115	0.06	0.0	0	1
G342.345-00.005_0	1.2	2.02	0.1	390	8213	2068	237	117	712	0.6	0.11	0	1
G342.357+00.113_0	9.9	36.18	0.21	19188	88037	27960	27428	758	297	0.63	0.36	0	1
G342.357+00.113_1	7.9	18.69	0.14	17042	99136	28094	6284	336	836	0.4	0.0	0	2
G342.357+00.113_2	1.2	1.6	0.08	836	13048	2269	394	246	628	0.22	0.11	0	1
G342.357+00.113_3	-	-	0.16	-	-	-	-	-	575	0.45	0.0	0	0
G342.357+00.113_4	2.4	2.74	0.07	2114	26129	5174	1480	541	718	0.17	0.02	0	2
G342.478-00.167_0	2.3	4.7	0.12	396	7231	1644	1603	341	564	1.0	0.2	0	1

Table 6. continued.

Filament ID	d kpc	l °	$l(d)$ pc	M(ATG) $M_\odot$	M(ATG + P) $M_\odot$	M(dust) $M_\odot$	M(gas) $M_\odot$	$m_{\rm crit,nt}$ $M_\odot\,pc^{-1}$	$m_{\rm obs}$ $M_\odot\,pc^{-1}$	det. ^{13}CO	det. C^{18}O	edge flag	d flag
G342.478-00.167_1	2.3	3.57	0.09	360	4840	1166	820	230	319	0.77	0.0	0	1
G342.823+00.129_0	2.7	1.54	0.03	157	4420	365	575	374	413	0.55	0.0	0	2
G343.579-00.170_0	2.6	5.01	0.11	680	8019	1677	2184	436	443	0.95	0.16	0	1
G343.776-00.149_0	2.6	28.73	0.63	9132	50422	14012	25245	879	606	0.99	0.48	0	1
G343.908+00.113_0	17.1	31.93	0.11	32107	128729	47790	32660	1023	777	0.47	0.01	0	1
G343.998-00.143_0	2.6	1.66	0.04	270	4731	985	420	253	452	0.48	0.0	0	1
G344.043-00.373_0	10.1	25.8	0.15	4717	32520	8963	13408	520	419	0.93	0.37	0	1
G344.340-00.227_0	10.2	25.78	0.14	4285	27090	6865	21249	824	392	1.0	0.36	0	1
G344.447-00.186_0	10.2	15.92	0.09	4180	20945	5622	9179	577	231	0.62	0.27	0	2
G344.447-00.186_1	-	-	0.03	-	-	-	-	-	280	0.25	0.0	0	0
G344.592-00.026_0	1.1	1.02	0.05	217	4705	1349	145	143	1142	1.0	0.05	0	1
G345.345-00.060_0	1.4	1.11	0.05	89	2641	184	504	454	388	0.67	0.0	0	2
G345.345-00.060_1	1.4	1.0	0.04	86	2471	176	48	48	342	0.62	0.0	0	2
G345.433-00.143_0	1.4	3.62	0.15	708	7953	2638	2292	633	611	1.0	0.62	0	1
G345.493+00.337_0	2.4	12.18	0.29	15468	34737	17632	26787	2199	810	1.0	0.76	0	1
G345.635+00.358_0	2.4	12.87	0.31	2358	28203	9874	18175	1412	1292	1.0	0.41	0	1
G345.873+00.292_0	2.4	4.59	0.11	411	9666	2399	2371	516	862	0.9	0.05	0	2
G345.879+00.021_0	7.5	24.88	0.19	19133	77043	31344	22821	917	245	0.44	0.3	0	1
G345.879+00.021_1	5.9	24.82	0.24	15692	78027	29208	12464	502	669	0.58	0.15	0	1
G345.879+00.021_2	1.4	4.48	0.18	1389	17994	5452	1259	281	1013	0.45	0.04	0	1
G346.177+00.029_0	5.6	7.81	0.08	1707	17128	3944	2259	289	576	0.72	0.03	0	2
G346.177+00.029_1	10.2	10.03	0.06	4965	41025	10177	6775	676	888	0.44	0.0	0	2
G346.177+00.029_2	14.8	8.54	0.03	7359	47552	13062	5198	608	630	0.36	0.03	0	1
G346.177+00.029_3	9.5	5.88	0.04	4076	31259	7985	1450	246	657	0.33	0.0	0	2
G346.293+00.109_0	9.5	29.15	0.18	22134	57231	22207	17934	615	569	0.92	0.32	0	1
G346.293+00.109_1	3.5	5.77	0.09	4011	17588	4531	1525	265	628	0.51	0.03	0	1
G346.293+00.109_2	13.3	15.65	0.07	23110	51740	22558	12584	804	216	0.32	0.23	0	1
G346.483+00.144_0	1.3	2.09	0.09	875	7475	2435	436	209	1131	0.97	0.26	0	1
G346.951-00.155_0	10.4	9.25	0.05	5225	19096	8013	3480	376	492	0.43	0.03	0	1
G346.951-00.155_1	10.4	8.56	0.05	6204	24235	9881	4275	500	893	0.49	0.0	0	1
G346.951-00.155_2	10.4	6.06	0.03	5145	18742	7876	2069	341	516	0.3	0.0	0	1
G347.216+00.026_0	10.7	44.39	0.24	46471	139034	60578	105279	2371	2303	1.0	0.35	0	1
G347.390+00.266_0	9.8	23.75	0.14	7917	51391	21931	13574	571	1153	0.73	0.0	0	2
G347.390+00.266_1	10.2	21.48	0.12	8059	49703	21490	12688	591	924	0.62	0.05	0	1
G347.390+00.266_2	10.7	5.93	0.03	6292	32706	14771	1555	262	360	0.17	0.0	0	2
G347.870-00.318_0	6.9	26.21	0.22	17433	43034	23512	39838	1520	597	0.95	0.59	0	1
G347.894+00.035_0	12.9	68.93	0.31	56255	171650	79834	66881	970	918	0.69	0.1	0	1
G347.894+00.035_1	9.8	13.61	0.08	35425	112024	51227	6757	497	686	0.2	0.0	0	2
G348.034+00.439_0	1.3	2.08	0.09	85	3305	163	1473	707	710	1.0	0.03	0	2
G348.232+00.462_0	1.3	15.94	0.7	3323	15729	4972	12082	758	627	1.0	0.7	1	1
G348.492+00.346_0	5.7	8.47	0.09	2025	17797	5214	4962	586	986	0.78	0.19	0	2
G348.492+00.346_1	1.3	2.17	0.1	151	3334	814	987	455	545	0.86	0.0	0	2
G349.876+00.099_0	10.7	48.39	0.26	38002	142702	53273	41081	849	1155	0.72	0.04	0	1

Table 6. continued.

Filament ID	d kpc	l °	$l(d)$ pc	M(ATG) $M_\odot$	M(ATG + P) $M_\odot$	M(dust) $M_\odot$	M(gas) $M_\odot$	$m_{\rm crit,nt}$ $M_\odot\,pc^{-1}$	$m_{\rm obs}$ $M_\odot\,pc^{-1}$	det. ^{13}CO	det. C^{18}O	edge flag	d flag
G349.876+00.099_1	8.3	27.39	0.19	25488	102875	36938	24430	892	1012	0.55	0.11	0	1
G349.876+00.099_2	22.1	15.3	0.04	70826	224169	91886	6137	401	667	0.11	0.0	0	2
G350.299+00.237_0	11.9	7.37	0.04	5673	39212	9603	4123	559	2098	0.4	0.0	0	2
G350.522-00.255_0	3.3	6.92	0.12	629	12239	2356	7750	1119	1152	1.0	0.29	0	1
G350.781+00.492_0	1.3	2.62	0.12	555	3521	787	1173	448	251	0.77	0.35	1	2
G351.022-00.343_0	3.3	10.54	0.18	2734	15104	4905	6417	609	461	1.0	0.64	0	1
G351.498+00.254_0	11.5	31.37	0.16	12708	59454	18081	15852	505	968	0.89	0.0	0	1
G351.731+00.446_0	1.3	1.26	0.06	77	2441	226	265	211	401	0.73	0.0	0	2
G351.928-00.245_0	3.5	8.54	0.14	2082	23029	5317	2989	350	717	0.65	0.03	0	1
G351.928-00.245_1	1.4	4.92	0.2	769	14656	3282	3996	812	1094	0.92	0.17	0	1
G352.030+00.069_0	1.4	2.29	0.09	199	6592	1282	933	408	275	0.57	0.24	0	2
G352.062-00.257_0	1.4	3.84	0.16	504	8351	1871	1730	450	689	0.91	0.32	0	1
G352.107+00.184_0	10.4	40.6	0.22	30749	132607	54065	28866	711	1160	0.84	0.24	0	1
G352.107+00.184_1	-	-	0.05	-	-	-	-	-	1256	0.19	0.0	0	0
G352.107+00.184_2	-	-	0.05	-	-	-	-	-	316	0.19	0.0	0	0
G352.208+00.354_0	1.3	1.64	0.07	181	2619	553	1137	693	186	1.0	0.87	0	1
G352.308-00.447_0	1.4	5.09	0.21	833	7057	1404	3182	625	684	0.99	0.59	0	1
G352.781-00.050_0	10.9	8.63	0.05	6024	39824	11177	2681	311	504	0.28	0.0	0	1
G352.883+00.464_0	1.4	3.77	0.15	534	9267	1930	6707	1779	1239	1.0	0.12	1	1
G353.201-00.242_0	3.1	6.81	0.13	1177	9209	3303	4458	654	286	0.92	0.62	0	1
G353.294+00.312_0	1.4	1.75	0.07	222	5616	1165	458	261	296	0.27	0.01	0	2
G353.294+00.312_1	1.4	0.93	0.04	247	6863	1463	77	84	436	0.17	0.0	0	2
G353.294+00.312_2	1.4	1.15	0.05	261	7439	1609	348	304	518	0.23	0.0	0	2
G353.389-00.340_0	3.1	39.48	0.73	31847	87054	46500	58559	1483	983	0.99	0.43	0	1
G353.418-00.208_0	8.8	18.23	0.12	4620	27338	7485	15398	845	692	1.0	0.16	0	1
G353.477-00.160_0	3.1	4.13	0.08	493	6119	788	2179	528	461	0.93	0.11	0	1
G353.564-00.464_0	3.1	5.24	0.1	1270	7954	2341	8275	1578	377	1.0	0.82	0	1
G353.949+00.252_0	1.0	3.07	0.18	371	4353	1068	1253	408	495	0.97	0.32	0	1
G353.992+00.321_0	1.0	0.72	0.04	198	2609	533	438	613	419	0.29	0.06	0	1
G354.991+00.421_0	8.4	13.21	0.09	4056	51840	11728	7021	532	2043	0.55	0.0	0	2
G355.211-00.496_0	1.4	1.57	0.06	633	2985	848	1828	1166	738	1.0	0.27	1	2
G355.257-00.260_0	-	-	0.11	-	-	-	-	-	637	1.0	0.67	0	0
G355.265+00.339_0	-	-	0.13	-	-	-	-	-	2160	0.51	0.0	0	0
G355.265+00.339_1	-	-	0.04	-	-	-	-	-	432	0.14	0.0	0	0
G355.265+00.339_2	-	-	0.03	-	-	-	-	-	864	0.15	0.01	0	0
G355.564+00.279_0	-	-	0.07	-	-	-	-	-	351	0.46	0.04	0	0
G355.564+00.279_1	-	-	0.04	-	-	-	-	-	643	0.3	0.0	0	0
G355.619-00.049_0	-	-	0.1	-	-	-	-	-	1037	0.94	0.09	0	0
G355.635+00.302_0	-	-	0.05	-	-	-	-	-	441	0.41	0.02	0	0
G355.635+00.302_1	-	-	0.05	-	-	-	-	-	508	0.41	0.02	0	0
G355.673+00.089_0	-	-	0.11	-	-	-	-	-	342	0.45	0.05	0	0
G355.673+00.089_1	-	-	0.07	-	-	-	-	-	944	0.29	0.0	0	0
G355.742-00.252_0	-	-	0.12	-	-	-	-	-	640	0.87	0.26	0	0

Table 6. continued.

Filament ID	d kpc	l °	$l(d)$ pc	M(ATG) $M_\odot$	M(ATG + P) $M_\odot$	M(dust) $M_\odot$	M(gas) $M_\odot$	$m_{\rm crit,nt}$ $M_\odot\,pc^{-1}$	$m_{\rm obs}$ $M_\odot\,pc^{-1}$	det. ^{13}CO	det. C^{18}O	edge flag	d flag
G355.742-00.252_1	-	-	0.03	-	-	-	-	-	299	0.26	0.0	0	0
G355.743+00.135_0	-	-	0.05	-	-	-	-	-	907	0.45	0.02	0	0
G355.836+00.317_0	-	-	0.06	-	-	-	-	-	357	0.17	0.02	0	0
G355.991-00.414_0	-	-	0.09	-	-	-	-	-	285	1.0	0.94	0	0
G356.416+00.088_0	-	-	0.13	-	-	-	-	-	455	0.88	0.3	0	0
G356.495+00.198_0	-	-	0.13	-	-	-	-	-	402	0.76	0.12	0	0
G356.874-00.021_0	-	-	0.1	-	-	-	-	-	621	0.97	0.24	0	0
G357.033+00.193_0	-	-	0.13	-	-	-	-	-	439	0.64	0.03	0	0
G357.420+00.356_0	-	-	0.05	-	-	-	-	-	393	0.85	0.0	0	0
G357.637-00.325_0	-	-	0.32	-	-	-	-	-	614	0.45	0.0	0	0
G357.637-00.325_1	-	-	0.07	-	-	-	-	-	445	0.12	0.03	0	0
G357.637-00.325_2	-	-	0.7	-	-	-	-	-	901	1.0	0.48	0	0
G357.956-00.160_0	-	-	0.21	-	-	-	-	-	1570	0.82	0.23	0	0
G357.956-00.160_1	-	-	0.12	-	-	-	-	-	568	0.4	0.13	0	0
G358.017-00.041_0	-	-	0.11	-	-	-	-	-	820	0.77	0.19	0	0
G358.017-00.041_1	-	-	0.09	-	-	-	-	-	749	0.6	0.0	0	0
G358.101-00.128_0	-	-	0.1	-	-	-	-	-	435	0.42	0.04	0	0
G358.101-00.128_1	-	-	0.23	-	-	-	-	-	954	1.0	0.63	0	0
G358.243-00.425_0	-	-	0.32	-	-	-	-	-	406	1.0	0.79	0	0
G358.243-00.425_1	-	-	0.15	-	-	-	-	-	632	0.46	0.0	0	0
G358.245+00.010_0	-	-	0.21	-	-	-	-	-	1660	0.56	0.0	0	0
G358.377-00.211_0	-	-	0.05	-	-	-	-	-	950	0.57	0.03	0	0
G358.377-00.211_1	-	-	0.06	-	-	-	-	-	4124	0.63	0.03	0	0
G358.451-00.422_0	-	-	0.54	-	-	-	-	-	675	0.88	0.63	1	0
G358.451-00.422_1	-	-	0.22	-	-	-	-	-	317	0.37	0.29	1	0
G358.451-00.422_2	-	-	0.13	-	-	-	-	-	389	0.22	0.05	1	0
G359.232+00.329_0	-	-	0.04	-	-	-	-	-	348	0.4	0.0	0	0
G359.372-00.437_0	-	-	0.16	-	-	-	-	-	186	1.0	0.73	0	0
G359.404+00.308_0	-	-	0.31	-	-	-	-	-	510	0.91	0.18	0	0
G359.404+00.308_1	-	-	0.04	-	-	-	-	-	330	0.11	0.0	0	0
G359.564-00.451_0	-	-	0.13	-	-	-	-	-	446	0.61	0.26	0	0
G359.863-00.248_0	-	-	0.05	-	-	-	-	-	1622	0.29	0.0	0	0
G359.863-00.248_1	-	-	0.11	-	-	-	-	-	909	0.75	0.27	0	0
G359.863-00.248_2	-	-	0.04	-	-	-	-	-	2180	0.29	0.0	0	0
G359.896-00.316_0	-	-	0.17	-	-	-	-	-	526	0.97	0.59	0	0